# Transition-Edge Superconducting Antenna-Coupled Bolometer

Thesis by

Cynthia L. Hunt

In Partial Fulfillment of the Requirements

for the Degree of

Doctor of Philosophy

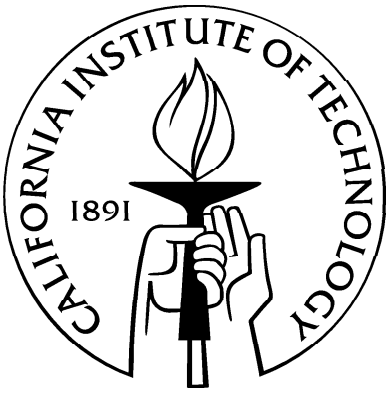


California Institute of Technology

Pasadena, California

2004

(Submitted August 25, 2003)

# Abstract

The temperature anisotropy of the cosmic microwave background (CMB) is now being probed with unprecedented accuracy and sky coverage by the Wilkinson Microwave Anisotropy Probe (WMAP), and will be definitively mapped by the Planck Surveyor after its launch in 2007. However, the polarization of the CMB will not be mapped with sufficient accuracy. In particular, the measurement of the curl-polarization, which may be used to probe the energy scale of the inflationary epoch, requires a large advance in the format of millimeter-wave bolometer arrays. SAMBA (Superconducting Antenna-coupled Multi-frequency Bolometric Array) is being developed to address these needs for the next generation of submillimeter astronomical detectors. SAMBA consists of a focal plane populated with microstrip-coupled slot antennas, whose signals are coherently added and sent to transition-edge superconducting (TES) bolometers via microstrip lines. SAMBA eliminates the need for the feedhorns and optical filters currently used on CMB observational instruments, such as Planck and Boomerang. The SAMBA architecture allows for a high density of pixels in the focal plane with minimal sub-Kelvin mass. As a precursor to a full monolithic high-density antenna array, we are developing a single-band antenna-coupled bolometric detector.

In this thesis, I report test results for a single-pixel antenna-coupled bolometric detector. Our device consists of a dual slot microstrip-coupled slot antenna coupled to an Al/Ti/Au voltage-biased TES. The coupling architecture involves propagating the signal along superconducting microstrip lines and terminating the lines at a normal metal resistor collocated with a TES on a thermally isolated island. The device, which is inherently polarization sensitive, is optimized for 140 GHz measurements. In the thermal bandwidth of the TES, we measure a noise equivalent power (NEP) of $2.0 \times 10^{-17}$ W/$\sqrt{\text{Hz}}$ in dark tests which agrees with the calculated NEP including only contributions from phonon, Johnson and amplifier noise. We do not measure any excess noise above this expectation at frequencies between 1 and 200 Hz. We measure a thermal conductance $G = 55$ pW/K. We measure a thermal time constant as low as 437 $\mu$s at 3 $\mu$V bias when stimulating the TES directly using a light emitting diode.

# Acknowledgements

I would like to thank the many people who have supported me throughout graduate school. First, I'd like to thank the Materials Science department at Caltech for allowing me to take on an unusual project in another department. I thoroughly enjoyed my coursework, and appreciated the welcoming approach the department takes toward its students. My candidacy committee and thesis committee deserve a special thanks for taking time out of their schedules to learn about my work and for guiding me on my way.

Andrew Lange was my advisor for the last five years, and I appreciate now more than ever the things he has taught me and the support that he's given me. His advice is invaluable.

To all those at JPL, a big thank you. First, I would like to thank my JPL supervisor, Jamie Bock for providing the overall support for this project. Thanks to Anthony Turner who taught me how to fabricate spiderweb bolometers. Thanks to Peter Day for teaching me the experimental techniques necessary in testing the devices. There are many other people who have given me support at JPL, both scientific and personal: Rick Le Duc, Bruce Bumble, Rick Vasquez, Paul Maker, Rich Muller, Steve Jurewicz, James Wishard, Hugo Velasquez, Keith Fields, Judi Podosek, Debra Cuda, Darren Dowell, Howard Rockstad, Amy Green, Steve Vargo, Peter Deelman, Thomas George, Barbara Jeffries Nakamura, and Suzi Martin. A special thank-you to Joanne Wellman.

Thank you to the entire SAMBA team for their regular support in my project: Andrew Lange, Jonas Zmuidzinas, , Rick Le Duc, Jamie Bock, Peter Day, Alexey Goldin, Anastasios Vayonakis, and Minhee Yun.

Thanks to the whole Lange group for befriending a Materials Girl, and teaching her a whole lot of cosmology on the way. Postdocs Jason Glenn, Sunil Golwala, Bryan Keating, Ravinder Bahtia, Eric Hivon, Faiz Rahman. My great office mates: Bill Jones, Christian Reichart, Ki Won Yoon and Sam Edgington, and the other grad students: Byron Philhour, Cynthia Chiang, Jack Sayers, and Brendan Crill are all good friends. Victor Hristov and Peter Mason for their support. Marcus Runyan has helped me in particular in two ways: by donating salt and by reading my thesis.

Kathy Deniston deserves a special thank-you for being the glue that holds the Lange group together. She has not only taken care of most of the logistics associated with my research, but she has also been a good friend and supporter.

Rebecca Chacon and I met at JPL in the Microdevices Lab, and we became quick and close friends. I can't say enough about how much I appreciate her on-going support, and ability to make me laugh. She is a wiz in the cleanroom, and maybe someday we will form CSP, as planned.

I don't know how to thank Andrew Benson enough. He is my best friend, my stalwart, and my partner in crime. He has the amazing ability to teach me, "There must be a pony in there somewhere!"

This work was supported under NASA/Goddard grant NAG5-10317. I am grateful to the Intel Foundation for providing a fellowship for my first two years in graduate school.

# Contents

# List of Figures

# Chapter 1

# Introduction

## 1.1 History of the early Universe

Cosmology is the study of the large-scale properties of the Universe as a whole. Cosmologists try to understand the origin, evolution, and fate of the Universe.

A fossil record of the Universe exists just after the Big Bang, long before the formation of the first galaxy or star. Shortly after the Big Bang, the Universe was a hot, dense, opaque soup of subatomic particles and light. About 300,000 years after the Big Bang, the Universe had expanded and cooled enough that this thick, opaque plasma became a transparent gas made up of mostly hydrogen and helium, and the photons were allowed to travel unhindered towards us. This primordial radiation is imprinted on the sky as the cosmic microwave background, or CMB. The CMB is the oldest electromagnetic radiation we can observe, and it has been travelling for about 15 billion years from this "surface of last scattering" to us today. To understand the early Universe, we need to make precise measurements of the CMB.

### 1.1.1 Understanding the origins of the CMB

To understand how the features of the CMB originate, we need to examine the physical processes that occur in the Universe during the epoch between the Big Bang through the surface of last scattering. The Big Bang model describes our Universe as a dynamic and evolving entity which started from an extremely hot and dense state at a finite time in the past, then expanded and cooled to what we now observe [73]. We know that the Universe is expanding [35], which implies that at an earlier time the Universe was much hotter, denser and smaller than it is now. If we extrapolate the expansion back far enough, the radius of the Universe goes to zero and the density approaches infinity.

The early Universe was hot and ionized, made up of subatomic particles (protons, free electrons, etc.), photons, and dark matter[1] [73]. Photons were easily scattered by the free electrons, so they had a very short mean free path: the Universe was opaque. This strong coupling between photons and electrons results in the photons and baryons acting as a coupled fluid. For example, the motion of baryonic material is strongly affected by radiation pressure.

The photons were repeatedly absorbed and scattered, coming into thermal equilibrium with their surroundings, and so obtaining a blackbody spectrum. As the Universe expanded and cooled to a temperature of approximately 3000 K about 300,000 years after the Big Bang, the electrons were able to combine with protons to form neutral hydrogen; this was the era of recombination [63]. The photons no longer scattered, and the Universe became transparent to the microwave background. These photons propagated from this "surface of last scattering" virtually unhindered until they reached us today. As the Universe expanded, the wavelengths of the photons increased (redshifted) from the near-infrared at approximately 3000 K to the millimeter-wave at 3 K. The cosmic microwave background we observe today consists of photons that originate from this opaque surface.

The CMB is not completely isotropic. This anisotropy comes from several sources. First, there is a very large scale temperature fluctuation in the CMB due to the motion of the observer relative to the CMB rest frame. This motion causes a Doppler effect where the radiation is blueshifted in the direction of motion of the observer and redshifted in the opposite direction, and smoothly varying in between. (See Figure 1.1 for a map of this effect.) We observe a temperature difference of 0.008 K between the hot and cold spots in this dipole. From these measurements, we can ascertain that the relative motion of the Earth compared to CMB rest frame is about 370 km/s [43].

There are also temperature anisotropies in the microwave background due to density perturbations of matter in the primordial Universe [72, 67]. Any small density perturbation in the Universe will tend to collapse under its own gravitational pull, thereby becoming ever denser. For baryonic material, however, when its density becomes sufficiently high, radiation pressure, which is the dominant pressure, will resist further gravitational collapse.

[1]Dark matter is matter that only interacts gravitationally and does not absorb or emit photons. This exotic stuff has never been directly detected, nor do we know exactly of what it is made. By measuring the masses of galaxies and clusters of galaxies, astronomers infer that there is approximately 10 times as much mass as can be accounted for from luminous matter alone, and so they postulate the existence of dark matter.

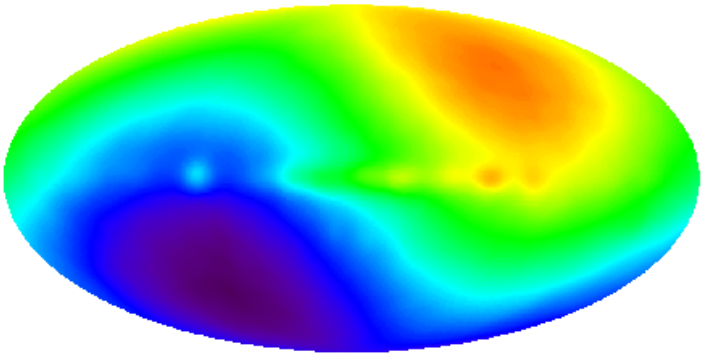

Figure 1.1: COBE-DMR temperature fluctuation map of the CMB, with the mean value, 2.728 K, subtracted, leaving the dominant dipole feature. Blue corresponds to 2.724 Kelvin, the value of the CMB blueshifted in the direction of the motion of the earth. Red is 2.732 Kelvin, the value of the CMB redshifted opposite the direction of the relative motion of the earth. The whole temperature range mapped here is 0.008 K from blue to red [1].

This pressure will cause the dense region to expand again. Eventually the pressure becomes so low due to this expansion that gravity dominates once more, and the cycle starts all over again, causing oscillations[2] [33]. When the baryonic material is at high density and high pressure, it is also at a high temperature. The photons that are frequently scattered come into thermal equilibrium with the local region of baryonic material, resulting in small scale temperature variations. The CMB has preserved a snapshot of these oscillations as they were at the surface of last scattering. (See Figure 1.6 for a full sky snapshot of these perturbations.) A perturbation which has reached the densest part of its cycle at the surface of last scattering will impart a particularly strong signal in the CMB; rarefactions will impart a signal of similar strength. The characteristic length scale of these fluctuations is $1^\circ$ on the sky, twice the size of the full moon. Quantitative calculations of the distribution of anisotropies have been made, and take into account other effects such as gravitational redshifts and the Doppler effect due to motions of baryons at the last scattering surface [40, 9]. The density perturbations in the early Universe ultimately lead to the large scale structures we observe today, such as galaxies and galaxy clusters.

[2]Unlike baryonic matter, dark matter does not exhibit density oscillations because it has no pressure. Dark matter has no pressure because it has no electromagnetic interactions like baryons; i.e., it does not interact with the photons.

### 1.1.2 Anisotropies in the cosmic microwave background: a wealth of information

What can the temperature fluctuations tell us? Cosmologists measure the anisotropy of the CMB to understand, among other things, the isotropy, geometry, and the partition of matter and energy of the Universe.

The temperature of the CMB is almost the same in every direction, which means that the Universe is nearly homogeneous and isotropic. Measurements of the temperature anisotropies tell us that it is isotropic to one part in 100,000 [19]. This extreme isotropy has a couple of important implications. First, this isotropy leads to the horizon problem [70]. The horizon defines the extent of the observable Universe. Since light has a finite speed, $c$, and since the Universe has a finite age, $t_{age}$, we can only observe regions of the Universe within a distance of order $c \cdot t_{age}$. More importantly, only regions within each other's horizons have had time to interact and thereby come into (thermal) equilibrium. For example, take two CMB photons coming from opposite directions on the sky. On Earth we can observe these photons, i.e., they are in our horizon. However, they are not within each other's horizons. So, the problem is, how can the CMB be the same temperature in all directions if the entirety of it has not had chance to interact? This problem remained unsolved until the theory of inflation was developed [25], which will be discussed in section 1.1.3. The second implication of measurements of the extreme isotropy of the Universe is that the simple models, which assume an isotropic and homogeneous Universe, and which have been used to describe the expanding Universe for decades are reasonable approximations [20, 21, 50].

From a map of the temperature anisotropy, we can measure the characteristic angular length scale of the fluctuations. This acts as a 'ruler' that we are observing from a great distance. Since the physical size of this ruler can be calculated, the observed angular size has implications for the geometry of the Universe. Two parallel lines on surfaces of different geometry will either converge, diverge or remain parallel. See Figure 1.2 for a graphic representation of this concept. Measurements of this ruler show that its size is exactly that which we would expect if the path the light took since this 'surface of last scattering' was that expected in a flat geometry. In this way, several experiments have confirmed that the Universe is flat [13, 27, 2].

The temperature anisotropies in the CMB preserve the conditions of the Universe at

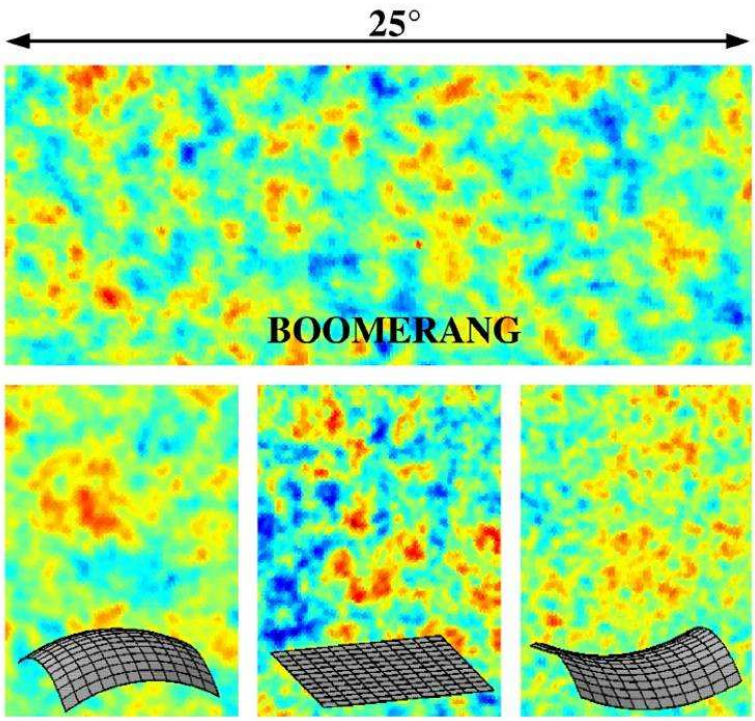


Figure 1.2: Measuring the geometry of the Universe. The top image is a 25° wide piece of the Boomerang field observed in December 1998 from Antarctica [71]. The hot spots in red give a characteristic length scale that we can measure. In the bottom panels, representations of three different geometries of the Universe are given—spherical, flat and hyperbolic, respectively. In addition, a simulated CMB temperature anisotropy map is given for each geometry. For a spherical Universe (left bottom panel), the hot spots appear much larger than those measured by Boomerang. In the hyperbolic Universe (right bottom panel) the hot spots appear smaller than those measured. The 1° hot spots measured by Boomerang indicate that the Universe has a nearly flat geometry. This has been confirmed by the first all-sky survey of WMAP [2].

the surface of last scattering. Different initial conditions, such as the amount of baryonic matter, amount of dark matter, and their interactions, would lead to different patterns left in the CMB. Understanding the details of the power levels at different angular scales can tell us about the relative amounts of different types of matter in the Universe [40, 9]. The temperature angular power spectrum can be seen as the black line in Figure 1.3.

### 1.1.3 Polarization

Besides the temperature anisotropies in the CMB, the radiation is also polarized. This polarization can yield its own wealth of information about the early Universe. Measurements of the polarization can verify our understanding of the primordial fluctuations in the Universe. The polarization is a powerful tool for studying the early Universe because it directly probes the epoch of last scattering. Whereas the temperature fluctuations can evolve over time since the surface of last scattering, the polarization experiences little to no evolution over time[3]. In this way, we can more accurately reconstruct the sources of the anisotropy. The polarization of the CMB gives some complementary information to the temperature power spectrum that can be used to break degeneracies and constrain cosmological parameters.

Thompson scattering of the photons off electrons transforms the temperature anisotropy into a local polarization field. In this way, the polarization in the CMB radiation arises from fluctuations in the early Universe. There are three geometrically distinct types of fluctuations in the early Universe that give rise to different polarization signals in the CMB: scalar, vector and tensor. Scalar perturbations are compressional fluctuations and are the most commonly considered fluctuations. These arise from density fluctuations at the surface of last scattering. Vector perturbations come from a shear force to the radiation field and give rise to a vortical component to the polarization signal, much like eddies in water. There is no associated density fluctuation with the vector perturbation. The tensor perturbations arise from gravitational waves interacting with the photons. The net polarization signal of the CMB is a superposition of these three perturbations.

There are four observable modes of anisotropies in the CMB: the temperature anisotropy, E-mode or grad mode polarization, B-mode or curl mode polarization, and a cross-correlation

[3]The temperature anisotropies change due to the integrated Sachs-Wolfe effect, gravitational lensing, the Rees-Sciama effect, scattering from free electrons after reionization, and the Sunyaev-Zeldovich effect to name a few. For a more detailed discussion of all these effects, the reader is referred to reference [32].

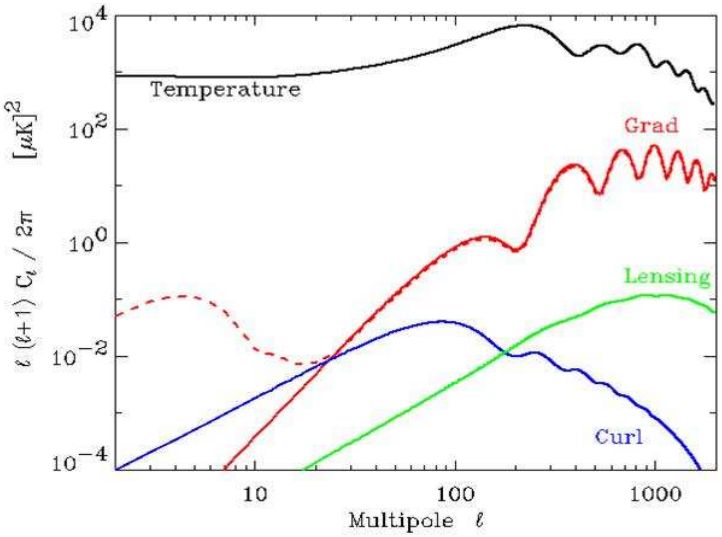


Figure 1.3: Angular power spectra of various features the CMB. The curves are plotted in terms of power ($\mu K^2$) versus angular scale. The top black curve is a model which reproduces experimentally measured temperature anisotropy. The next lowest power curve is the gradient polarization shown in red. The curl polarization curve is estimated and shown in blue. Note how at small angular scales gravitational lensing overcomes the curl signal.

between the temperature and polarization. The CMB has sufficient information to distinguish between the modes which arise from the three types of fluctuations [34].

See Figure 1.3 for an estimate of the power of the gradient and curl angular power spectra. The black line at the top is the best fit temperature anisotropy power spectrum to the WMAP data [2]. The peak of the E-mode, or grad signal is expected to be almost 2 orders of magnitude below the temperature power spectrum. The curl signal is thought to be about 4 orders of magnitude below that. While gravitational waves should be detectable in the cosmic microwave background embedded in the curl polarization mode, their characteristic signal is much weaker than the temperature fluctuations and so is difficult to distinguish. To add to the confusion, there is also power from a polarization signal from gravitational lensing that begins to overtake the curl signal at small angular scales.

The 'holy grail' of polarization measurements is to show direct evidence of the inflationary epoch. At a time of about $10^{-32}$ seconds after the Big Bang, the Universe is thought to have undergone a very short period of extremely rapid acceleration, called inflation. The radius of the Universe jumped about 60 orders of magnitude in $10^{-38}$s. Inflation predicts

that the Universe is flat due to this enormous expansion of space. Inflation also resolves the horizon problem, and predicts that the Universe is isotropic and homogeneous on large scales. Current observations of the temperature anisotropy are consistent with the theory of inflation, however we need a more direct measurement of the consequences of inflation.

The rapid acceleration of the Universe produces gravitational waves, or ripples in the gravitational field of the Universe [33]. The gravitational waves impart a curl component to the polarization of the CMB due to the quadrupole stretching of space. The strength of this signal, however, is unknown. It depends on the details of this inflationary epoch, for example when it occurred. (See Figure 1.3 for an estimate of the curl polarization power spectrum.) Theory predicts that the strongest gravitational wave signal should be at the longest wavelengths, especially those approaching the size of the Universe [34]. Thus, the CMB and the Universe may provide the best gravitational wave detector known. If we can observe evidence of these gravitational waves, this would be the first direct evidence of inflation in the early Universe.

Just as with the temperature anisotropy, if we are clever enough, we should be able to make maps of the polarization of the CMB across the sky. Figure 1.4 shows a model of what this polarization signal might look like superimposed on the temperature anisotropy map. The next big challenge for observational cosmology is to precisely measure the polarization of the CMB, which can provide direct proof of the inflationary epoch and perhaps detect signatures of gravitational waves.

## 1.2 History of CMB Science

The existence of the CMB was first posited by George Gamow in 1948 [22] and by Ralph Alpher and Robert Herman in 1950 [6]. It was another 15 years before Arno Penzias and Robert Wilson at the Bell Laboratories found a constant noisy background in their microwave radiometer in New Jersey [64]. Unaware of the cosmic microwave radiation posited by theorists, they investigated various explanations of their "antenna temperature problem" [82]. They thought through the possibilities of atmospheric microwave absorption, man-made sources, galactic sources, extraterrestrial sources, and inherent antenna problems. One by one they ruled these out, even going so far as to clean pigeon poop off parts of the horn antenna! It was not until Penzias mentioned their spurious antenna noise when

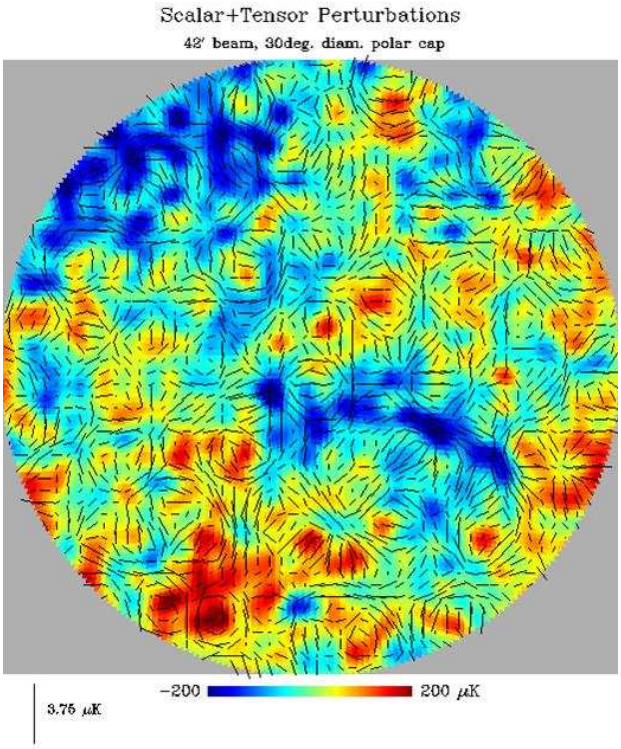


Figure 1.4: Simulated map of the polarization of the CMB superimposed on a temperature fluctuation map. Regions with a curl component are remnants of gravitational waves produced by inflation.

he was working with some collaborators at MIT that they found an explanation. They had remembered some theoretical work done at Princeton about a relic blackbody radiation filling the Universe. Wilson said in 1978 in his speech to the Nobel Prize committee, "We were pleased that the mysterious noise appearing in our antenna had an explanation of any kind, especially one with such significant cosmological implications. Our mood, however, remained one of cautious optimism for some time" [82]. Within the year they received independent confirmation of the measurement from Roll and Wilkinson at Princeton [15]; CMB experimental science was born.

In 1967, Rees and Sciama suggested that large scale temperature fluctuations in the CMB "should be looked for" [67]. At that time, observations and theoretical calculations suggested that these fluctuations should be on the order of a few percent, or tens of millikelvin [72, 61]. Kip Thorne even said, "...we may soon be able to determine with some confidence the large-scale geometry and dynamics of the Universe. In order to prepare for the time—only a few years hence—when greatly improved observations will be available, it would be useful to examine in detail the microwave predictions..." [77]. Unfortunately this was an extremely optimistic estimate of the time needed to make those definitive observations of the small scale anisotropies that would shed light on the beginnings of the Universe and its cosmological consequences. More than 25 years passed after Penzias and Wilson's initial discovery before detector technology was mature enough to detect the small scale CMB temperature fluctuations.

The CMB field slowly progressed during this quarter century. The greatest achievements were in measuring the spectrum of the CMB. Observations were made at over 30 different wavelengths measuring the absolute temperature of the CMB. These observations provided unambiguous evidence that the CMB fit a Planck blackbody spectrum (as in Figure 1.5), just as theorists predicted. The compilation of data yielded strong, direct evidence in support of the Big Bang theory.

It was not until the late 1970's that the dipole of the CMB due to the Earth's motion was measured. This anisotropy was first posited in 1968 by Peebles and Wilkinson [62], and was sought after by observationalists using ground-based techniques. These measurements were plagued by large systematic errors, Galactic emission problems, and atmospheric fluctuations. The dipole was unambiguously observed by two groups who took great pains to carefully design their instrument to reduce the systematic errors. In addition, they

made their measurements from the upper atmosphere to avoid the atmospheric problems of ground-based instruments. The Berkeley group achieved this by flying their instrument in a NASA U-2 aircraft at 20 km [74], while the Princeton/MIT group flew their instrument in balloon flights, covering half the sky [12]. Neither group was able to measure an appreciable quadrupole or smaller angular scale component to the radiation.

During those 25 years, groups continued to make tighter restrictions on the upper limit of the temperature fluctuations of the background radiation. Unfortunately, no one was totally sure how large the temperature fluctuations were. In the early 1980's, the Soviet Union launched the RELIKT instrument aboard the Prognoz 9 satellite to make a detection of the temperature anisotropy of the CMB. Unfortunately, their radiometer was just not sensitive enough; it could only measure temperature variations of 100 $\mu$K with a beam size of 5.5° [76].

NASA's Cosmic Background Explorer (COBE) satellite was proposed in 1974, but not launched until late 1989 [1]. A spaceborn mission has several major advantages over high-altitude experiments (balloon or U-2 aircraft) — atmospheric emission is reduced to a minimum, the instrument can map the entire sky, and observations can be made over an extended period of time. COBE contained three instruments: FIRAS to measure the spectrum of the CMB, DMR to measure the temperature anisotropies across the entire sky, and DIRBE to look at shorter wavelengths. FIRAS made a high precision measurement of the blackbody spectrum of the CMB (Figure 1.5). DMR was the first instrument to make a positive measurement of the small scale anisotropies of the CMB at several wavelengths, and they were found to be $36 \pm 5$ $\mu$ K at the 7° scale. Since the beam was 7°, it could not resolve details on the characteristic 1° scale, however.

It was another 10 years before the instruments were sensitive enough to make the first maps of the small scale anisotropies, and extract a viable extended power spectrum around the first peaks. These results were first released in 2000 by Boomerang [13] and in 2001 by DASI [27], from Caltech and University of Chicago consortia, respectively. These instruments, remarkably, were very different. Boomerang was a balloon-born telescope making direct maps of the temperature fluctuations at several wavelengths using bolometers. DASI was a ground-based telescope in Antarctica using interferometry to measure the power spectrum with HEMT receivers[4]. Both experiments found the first peak of the power spectrum,

[4]Detector technology will be discussed in greater detail in Chapters 2 and 4.

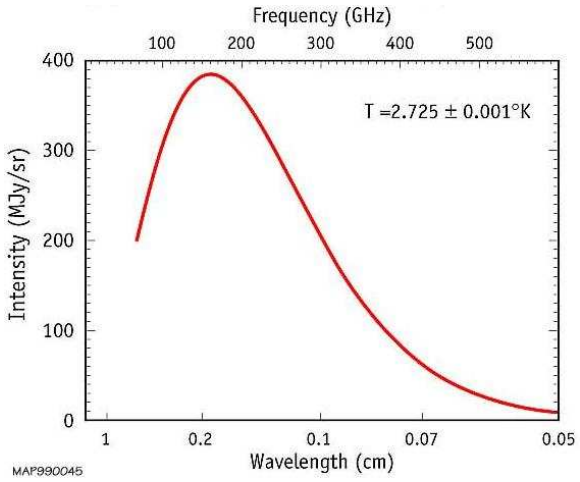


Figure 1.5: The temperature spectrum of the CMB compared to a thermal blackbody emission curve at 2.725K. The error bars are so small that they cannot be seen under the thickness of the red spectrum curve [19].

or the characteristic angular length scale of the fluctuations, to be $\sim 1^\circ$ to within 10% of each other [18, 56].

The Wilkinson Microwave Anisotropy Probe, or WMAP, is a NASA space probe launched in 2001 that has made some of the most sensitive, full-sky measurements of the CMB [2]. Like COBE, it employs interferometry to measure the power spectrum and extract maps of the temperature fluctuations of the CMB. Whereas Boomerang and DASI could only observe a relatively small patch of sky, WMAP has been able to observe the entire sky. It will observe for four years, remapping the entire sky 8 times to increase sensitivity. WMAP has confirmed the previous results from Boomerang and DASI. It has also detected the correlation between the temperature and the polarization anisotropy of the CMB. While WMAP's success is unquestioned, it was not designed to make measurements at fine angular scales, nor was it designed to precisely map the polarization of the CMB.

A future spaceborn instrument that will be able to address these issues is the Planck Surveyor scheduled to be launched in 2007 by the European Space Agency (ESA). [3] It will employ both HEMT receivers and bolometer arrays in 9 frequency bands. Planck has a wide spectral coverage, and will measure the temperature power spectrum from a few degrees down to $5'$. In addition, it has polarization sensitive bolometers that could measure the E-mode power spectrum to a tenth of a degree. Planck is at the leading edge of what we can do with the state-of-the-art technology—its focal plane is packed densely with feedhorns,

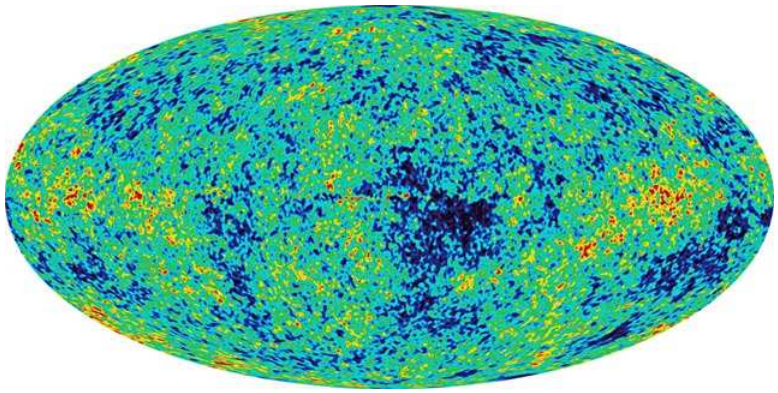

Figure 1.6: Full-sky map of the temperature anisotropies of the CMB as measured by WMAP.

and the bolometers are background limited. Unfortunately Planck will not have the same sensitivity in the curl component of the polarization signal.

In the far future, NASA is proposing an "Inflation Probe" as a part of the Beyond Einstein road map of future missions to understand our Universe in more detail [4]. The goal of the Inflation Probe is to map the polarization of the CMB, both the gradient and curl components, to determine the sources of the polarization and to look for the direct evidence of gravitational waves from the Big Bang. The plan calls for large arrays of polarization sensitive detectors operating with a large bandwidth. To achieve these science goals, the instrument will have to increase its sensitivity by about 100 times over the projected sensitivity for the Planck surveyor. Since Planck is already at the limit of the state-of-the-art technology, radically new advances will have to be made in the detectors and the overall architecture in order to fulfill the science goals laid out by NASA.

The state of the field today is that we are making very precise measurements of the temperature fluctuations over the whole sky. Future experiments will definitively map the whole sky even to small angular scales, and will attempt to measure the polarization. In addition, several experiments (DASI, Maxipol, Boomerang 2K2) have begun to make polarization sensitive maps of patches of the sky [49, 44]. Future spaceborne experiments will map the polarization with high precision and accuracy, provided the technology has advanced enough to meet these goals.

# Chapter 2

# Bolometers: History and Current Technology

## 2.1 What is a bolometer?

A bolometer is a thermal radiation detector whose output is an electrical signal[1]. Bolometers are very broad band detectors and are used from X-ray through millimeter-wave regimes [29, 10, 65]. Bolometers are the most sensitive direct detectors between wavelengths of 200$\mu$m and 5mm, a range that includes most of the CMB. In this regime there are no photoconductive detectors that can efficiently couple to the radiation. The work in this thesis is concerned with bolometers in this range for submillimeter and millimeter-wave cosmology.

A simple model of a bolometer is shown in Figure 2.1. It consists of an absorbing element of heat capacity $C$, which is connected to a thermal bath by a weak thermal link of conductance $G$. When illuminated with radiation, a power $P$ is absorbed in $C$, and the detector temperature $T$ rises above the bath temperature, $T_0$. The heat then dissipates through the weak thermal link, and the absorbing element equilibrates back to its quiescent temperature. This temperature change is measured with a sensitive thermistor. The temperature rise is related to the power deposited in the absorber, which makes the bolometer a thermal radiation detector.

This chapter first describes a brief history of bolometer technology, then discusses current technology. The shortcomings of the currently implemented bolometer technology are highlighted with reference to future CMB missions.

[1] "Thermal radiation detector" is a confusing phrase often used in the bolometer community. We mean that the bolometer detects radiation thermally, not that the bolometer exclusively detects thermal radiation.

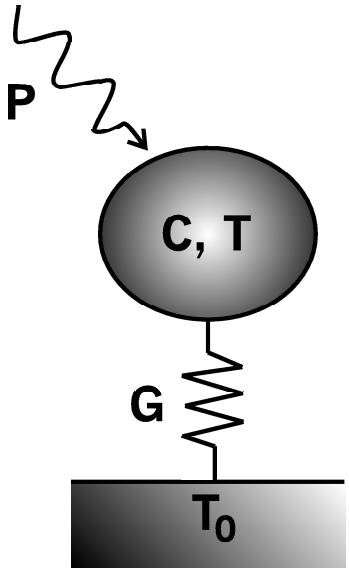


Figure 2.1: A schematic of a simple bolometer. The bolometer consists of an absorbing element of heat capacity $C$ which is weakly coupled to a thermal bath at temperature $T_0$ through a weak thermal conductance $G$. When a power $P$ is absorbed in $C$, the temperature of the absorbing element increases, and equilibrates in a characteristic time scale of $\tau_{therm} = C/G$. This temperature rise is related to the power deposited in the absorber, which makes the bolometer a thermal radiation detector.

## 2.2 Previous bolometer technology

Herschel developed one of the first thermal detectors: a mercury-glass thermometer to detect radiation that was not visible to the eye but just beyond the red light dispersed by a prism [28].

The word bolometer comes from the Greek, "*bole*", which means "ray of light". The term was first coined in 1881 by Samuel P. Langley [47]. Langley used a bolometer to make infrared measurements of astronomical objects, most notably the infrared portion of the Solar spectrum. Langley's bolometer used a pair of matched platinum strips, which were the arms in a Wheatstone bridge. When one strip was exposed to radiation while the other remained dark, the change in temperature of the exposed strip changed its resistance and unbalanced the bridge. He successfully measured temperature differences of $10\mu$K in the Solar spectrum.

P. Richards reviews in reference [68] a detailed history of bolometers for the wavelengths discussed in this thesis, that is infrared to millimeter wavelengths. We will pick up the story in 1983, just before the modern history of bolometers begins. At that time, 'com-

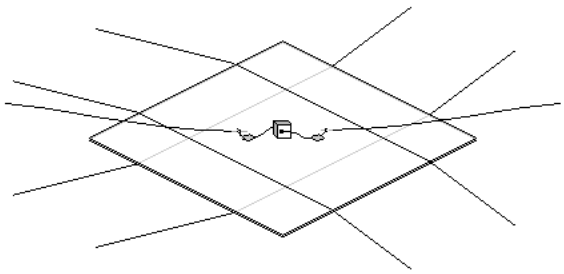

Figure 2.2: A drawing of the old composite bolometers. This type of bolometer had to be assembled by hand, had high heat capacities and high thermal conductance. They were also susceptible to cosmic rays, which would saturate the detector.

posite bolometers' were the state-of-the-art. The individual elements of these composite bolometers (Figure 2.2) had to be assembled by hand one at a time; the leads were soldered to the thermistor, the thermistor was soldered to the absorber, and it was all suspended by delicate kevlar threads [46].

In 1984 P. M. Downey et al. developed monolithic silicon bolometers [17]. These were different from the old 'composite bolometers' because they could be mass produced using silicon microfabrication techniques. The monolithic bolometers had integrated components on one chip; the wires, absorber, and thermally isolated island are patterned using photolithography. This allowed the features to be much smaller than before, reducing the heat capacity, lowering the thermal conductance, and reducing the noise levels. The bolometer technology in use today is a variation of the original monolithic bolometers.

## 2.3 Current bolometer technology

The state of the art in millimeter-wave direct detection are spiderweb bolometers (Figure 2.3). The absorbing area is a free-standing mesh of silicon nitride, which provides support, covered by a thin film of metal to aid in the absorption. The thermal supports are bare legs of silicon nitride typically 1 mm long by 5 $\mu$m wide by 1 $\mu$m thick. The open areas in the web are much smaller than the wavelength being detected, so the web acts as a solid absorber to incoming radiation. One large advantage in this design is the greatly reduced total heat capacity of the bolometer. In a spiderweb bolometer the heat capacity of the absorber is

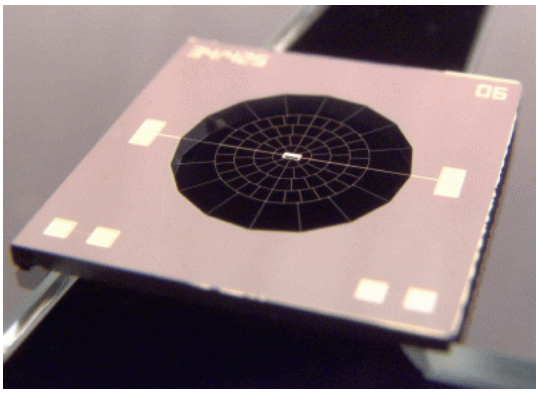

Figure 2.3: Spiderweb bolometer. The absorber is a micromesh of silicon nitride substrate with metal film absorber. There are 12 supporting legs, each 1mm long, with two leg supporting the readout leads from the NTD-Ge chip. The mesh and legs give the bolometer the look of a 'spiderweb.' The thermistor is a doped semiconductor chip made of neutron transmutation doped Ge (NTD-Ge), and is bonded in the center of the web. The whole structure is supported by a silicon frame. The bolometer pictured here is a typical example of the spiderweb bolometers used in many CMB temperature anisotropy missions, including Archeops, Boomerang, and the Planck Surveyor.

minimized. The total heat capacity of the bolometer is dominated by the thermistor and the In-bump bonds connecting the thermistor to the absorber. The reduced heat capacity decreases the thermalization time of the absorber. This, coupled with the reduced thermal conductance, increases its sensitivity. Another advantage to the spiderweb design is the considerable reduction in microphonic noise due to the greatly reduced suspended mass. In addition, this device provides a 95% reduction in cosmic ray cross section due to the small geometric cross section [8, 59].

Spiderweb bolometers are not inherently polarization sensitive, polarization being a key feature necessary for detectors on future CMB missions. There has been some work using polarized grids, which act as a beam splitter to orthogonal polarizations which are fed to a separate set of filters then to spiderweb bolometers. However, this work was plagued with errors from the differences in filtering between the polarizations and uncertainty arising from mixing of the polarizations before hitting the beam splitters [7]. Recent work by Maxipol uses a waveplate to extract one polarization utilizing a spiderweb bolometer as the detector [5]. A modified spiderweb bolometer is showing great promise for polarization CMB work. Dubbed 'PSB' for polarization sensitive bolometer, the 'web' absorbing structure is replaced with parallel metallized slats (Figure 2.4). In this way the bolometer itself is sensitive to only

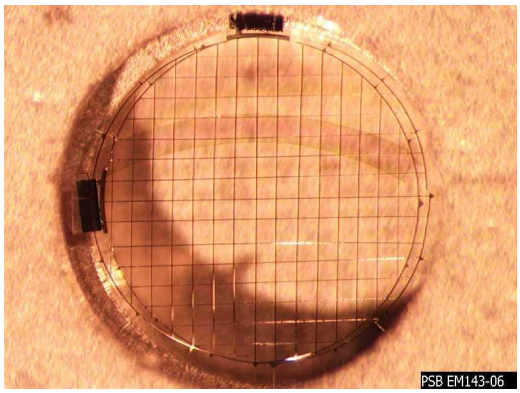


Figure 2.4: This polarization sensitive bolometer pair, also referred to as a PSB pair, is of a similar type as that used on Boomerang 2K2 and will be used on some channels in the Planck Surveyor. The PSB pair is mounted with absorbing grids perpendicular to each other and only 60 $\mu$m separation. The NTD-Ge chips can be seen as black rectangles on the left side of the image for the horizontally oriented grid and the top of the image for the vertically oriented one. The author of this thesis fabricated the proof-of-science PSBs shown in this photograph.

one polarization. A PSB pair is mounted with absorbing grids perpendicular to each other so that the same pixel on the sky is sensitive to orthogonal polarizations. These bolometers have been shown to have higher sensitivity to one polarization than the previous Boomerang flight, which detected all polarizations. In addition, the total system cross-polarization was only 5% [39].

The traditional spiderweb bolometer and its polarization sensitive counterpart, the PSB, typically sit at the back of a feedhorn structure. The feedhorn collects the radiation and focuses it on the absorbing area of the detector, increasing the optical efficiency. The feedhorn also houses filters that define the band of interest. A typical feedhorn structure is shown in Figure 2.5, and its drawbacks are discussed in Section 2.3.2.

### 2.3.1 Thermistor technologies

The monolithic bolometers allow for various types of thermistors to be either integrated or attached to the absorber. There are several thermistor technologies in use today: doped semiconductors, including neutron transmutation doped Ge (NTD-Ge) and ion-implanted Si, and superconducting transition edge sensors (TES).

A sensitive bolometer uses a thermometer material with a strongly temperature dependant resistivity. Currently the most common thermistor in use for sub-mm bolometers is a

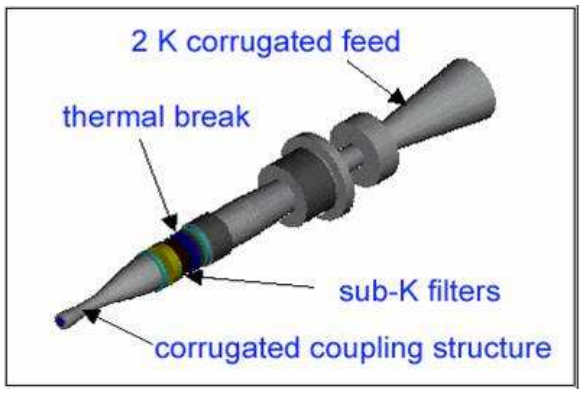


Figure 2.5: A single feedhorn structure for one frequency band. The feedhorn is made of electroformed copper, and a detector sits at the back end of the optical structure. In between the feedhorn and detector are various filters needed to define the frequency band. This structure typically weighs 100g, and is cooled to 2–4K.

neutron-transmutation-doped Ge crystal (NTD-Ge) [26, 83], used by Archeops, Boomerang, and the Planck Surveyor to name a few. NTD-Ge is doped by thermal neutron irradiation of a Ge crystal, thereby converting some Ge atoms into As or Ga dopants [38]. NTD-Ge has a resistance that is a strong function of temperature, can be optimized for a given operating temperature, and the neutron irradiation yields highly reproducible doping levels. Although NTD-Ge has been used in many ground breaking CMB experiments, it has several significant drawbacks. First, the thermistors are relatively bulky: 25 $\mu$m $\times$ 300 $\mu$m $\times$ 100 $\mu$m for Boomerang 2K2 compared to the 1 $\mu$m substrate thickness. This not only creates engineering difficulties in tight spaces, but also means it has a high heat capacity and thus a relatively large time constant. Second, NTD-Ge thermistors have to be bonded to the substrate wafer by hand using indium bumps. This makes reproduction reliability difficult in large arrays, and results in a high cost of woman-hours needed to assemble the thermistors. Third, the thermistor needs to be in good thermal contact with the absorber, which often means being in the optical path and thus being susceptible to cosmic ray hits.

An alternate thermistor to NTD-Ge is ion-implanted Si. The advantage of this technology is that the thermistor is integrated into the absorber by implanting the dopants directly into the support structure. Ion-implanted Si tends to show 1/f noise at low frequencies and has limited resolution for X-ray astronomy [60]. For submillimeter astronomy, SHARC II uses ion-implanted Si on 'pop-up bolometers' [16, 80]. They have minimized 1/f noise inherent in other ion-implanted detectors by increasing the volume of the doped region. The

drawback of this technology is that the final dopant concentration is difficult to predict. Typically a series of wafers are doped by increasing amounts to obtain a range of dopant concentration values, then an optimal wafer for a given application is chosen. This is time consuming and not practical for very large format arrays.

The resistive transition of a superconductor has one of the strongest known dependencies of resistivity on temperature. A superconductor with a critical temperature $T_c$ in the operating range of a system is therefore an ideal choice for a thermistor, and are dubbed transition edge sensors (TES). TES detectors can be an order of magnitude faster than semiconducting thermistors. In addition, they are mass produced directly on the device wafer using standard lithographic techniques, eliminating the need to bond thermistors by hand, as is necessary with NTD-Ge chips. TES detectors can have a very small active area, reducing the total heat capacity of the detector. The small area of the TES also has the advantage of thermalizing quickly. The work in this thesis centers around TES detectors. Their advantages, disadvantages, and characteristics will be discussed in the remaining chapters.

### 2.3.2 Drawbacks of current technology

The spiderweb bolometer and PSB described above work very well, but unfortunately they have several drawbacks that make them unrealistic candidates for large format arrays. Compared to the array formats and spectroscopic capabilities available in other regions of the electromagnetic spectrum, current CMB bolometers and their overall systems are primitive.

The current spiderweb bolometers generally have a semiconductor thermistor in the form of NTD-Ge chips that have to be placed and bonded by hand. It takes considerable time and woman-power to bond one NTD-Ge chip by hand, let alone the thousands needed for a large format array. In addition, the chip is usually directly in the optical path, so it is susceptible to cosmic rays. Currently this relatively massive component on the bolometer contains a large piece of the heat capacity budget when designing a bolometer. For the bolometers in the Planck Surveyor, the NTD-Ge and its components are 35–45% of the total heat capacity of the device.

The scientific requirements needed in the mm to sub-mm wavelength regime demand large format arrays that contain $\gg$1000 elements. The readout electronics of the doped

semiconductor chips do not lend themselves to large arrays. Multiplexing is not possible, and the number of amplifiers and the number of cables quickly become overwhelming. In addition, Si JFET amplifiers are used to read out the doped semiconducting thermistors. These amplifiers dissipate a lot of power, increasing the cooling requirements. Typically JFETs dissipate $\sim \mu$W at 120 K. Large format arrays require many JFETs, complicating the systems requirements.

Another obstacle to building the large format arrays is the large size of the absorbing area. Often, much of the area is devoted to the delicate thermal offset architecture, reducing photon throughput. 'Pop-up' bolometers developed at NASA Goddard Space Flight Center (GSFC) minimize the in-plane size of these legs, but they still require a large absorber area that couples directly to the radiation [16, 80]. The large absorbing area is susceptible to stray radiation as well as cosmic rays.

Aside from the drawbacks in the detector technology itself, one of the main problems with the current systems technology is the need for massive optics, including feedhorns and optical filter stacks. For the Planck Surveyor, a typical feedhorn is approximately 100 g (depending on the wavelength), and there are 36 feedhorn structures on the High Frequency Instrument. The more massive the detection system is, the harder it is to cool down cryogenically, and the more expensive it is to fly for a space-borne mission. The filters in particular are a dielectric with high heat capacity and therefore difficult to cool down.

The same feedhorns that are difficult to cool also limit the pixel density that can be achieved. Even though the Planck Surveyor's focal plane is as densely packed as possible, each feedhorn has a physical aperture that is many times the area of the effective optical aperture. Roughly 90% of photons are lost due to this size discrepancy. 90% of the remaining 10% of photons are lost in the band-defining filter stacks. In the end, only $\sim 1\%$ of the total energy of interest that is incident on the focal plane ever reaches a detector.

The state of the art in CMB bolometer technology in use today has led to great advances in our ability to measure the CMB temperature anisotropies, and the polarization of the CMB is starting to be measured. However, this technology is not good enough to make detailed polarization maps that are required in order to find the characteristic polarization signal imparted by gravitational waves.

# Chapter 3

# Antenna-Coupled Detector Architecture

## 3.1 SAMBA architecture

SAMBA (Superconducting Antenna-coupled Multi-frequency Bolometric Array) has been developed at Caltech and the Jet Propulsion Laboratory (JPL) as a next generation detector architecture to address the issues facing future CMB missions. SAMBA represents a great departure from the bolometer technology in use today. It will be an ideal multi-color camera system for sub-mm wave cosmology because it increases the number of detectors in the focal plane by an order of magnitude and simultaneously decreases by an order of magnitude the mass, volume and cooling requirements of the focal plane.

SAMBA consists of a focal plane populated with multi-slot antennas, whose signals are sampled by taps placed along each slot. These signals are sent outside the active area of the antenna array and are coherently added. They are then sent to a bank of microstrip filters to define multiple bandpass regimes. The microstrip transmission line is terminated and it dissipates the electromagnetic power in a normal metal resistor, which acts as an 'absorber.' A transition edge sensor (TES) measures the temperature change of the absorber, which is related to the power of the radiation incident on the antenna.

There are several advantages to the SAMBA design. The microstrip architecture, including both the antennas and the transmission lines, offers up many of these advantages. Microstrip-coupled slot antennas couple to one polarization, and are thus a natural choice for CMB polarimetry [11]. Slot antennas can be densely packed and arranged in the focal plane to measure several polarizations simultaneously. The antennas provide natural beam directivity, controlling the detector field of view at the focal plane [24]. SAMBA eliminates

the need for the massive feedhorns currently used on CMB bolometer-based observational instruments, such as Planck and Boomerang. The SAMBA architecture allows for a high density of pixels in the focal plane with minimal sub-Kelvin mass.

Another advantage is that microstrip filters can be inserted between the antennas and the bolometer to define the frequency bands [24]. This filtering replaces conventional optical filter stacks that are massive and cumbersome in current millimeter wave experiments such as Boomerang and Planck. Microstrip-coupled slot antennas can be engineered as broadband receivers. By using both microstrip antennas and microstrip filters there is a potential to define several frequency bands from the very same pixel, a feature not available with current technology.

The terminating normal metal resistor replaces traditional absorbers whose areas that need to have a large active area in order to couple efficiently to the radiation. Our resistor can be as small as lithographic techniques permit. Such a small resistor does not couple easily to stray radiation. In addition, a small absorber means reduced heat capacity and a hence a faster detector.

Yet another advantage of the microstrip transmission line, is that can be quite long while having only small losses. Vayonakis et al. report 1% loss per wavelength in the dielectric at temperatures below 1.5K, and specifically measure this loss at 150 GHz [79]. For a densely packed focal plane of microstrip antennas, this small loss allows the TES bolometers to be placed out of the optically exposed focal plane, maximizing the focal plane area for antennas.

Replacing the thermistor with TES films offer several advantages to the design. First, the electrothermal feedback of a voltage-biased TES increases the speed of the detector, the details of which are discussed in Chapter 4. Also, the feedback suppresses Johnson noise at low frequencies. TES bolometers are read out using SQUID amplifiers which offer a significant improvement in noise performance. SQUIDs dissipate several nW of power at temperatures below 4K, while JFET amplifiers dissipate $\sim \mu$W at 120K. The use of SQUID amplifiers greatly reduces the cooling requirements.

## 3.2 Single element device

As a precursor to a full monolithic high-density antenna array, we are developing a single band antenna-coupled bolometric detector. The single element device presented in this thesis consists of a dual slot antenna [84] coupled to a TES (Figure 3.1). This device was designed to test two elements in the SAMBA design. First, it is a test structure for the TES itself, studying the properties of the superconducting film while it is in operation, both when it is illuminated with radiation and when it is dark. Second, this device was designed to test the unique coupling structure between the microstrip antennas and the TES thermistor.

In operation, the electric field from the slot antennas propagates along planar microstrip lines. The microstrip consists of a niobium superconducting lead separated from a niobium ground plane by 2000Å of SiO dielectric. Both niobium layers are 2000Å thick. The electric fields from each antenna in the microstrip lines are passively and coherently added and terminated at a thin film Au resistor. The resistor, which is designed to be used as the microstrip termination or an 'absorber,' can also be used as a heater to simulate optical power. This resistor is located on a thermally isolated silicon nitride island. A close-up photo of this island is shown in Figure 3.2. On the same island, an Al/Ti/Au TES film responds to power dissipated in the resistor, and the signal is read out with a low impedance superconducting quantum interference device (SQUID) current amplifier.

The TES film is a trilayer of aluminum, titanium, and gold. Typically TES films consist of a bilayer of a normal metal and superconductor. The $T_c$ of these films can be adjusted by changing the relative thickness of the layers, utilizing the so-called 'proximity effect' [55]. The normal metal is chosen to be a high conductivity material so the heat diffuses rapidly through the film. Our trilayer has superconducting layers of aluminum and titanium, and a normal layer of gold. The titanium acts as a diffusion barrier between the aluminum and the gold. These materials are easy to deposit with few impurities in a standard e-beam evaporation system. JPL has focused their TES efforts on this trilayer, so it was the natural choice for the work in this thesis.

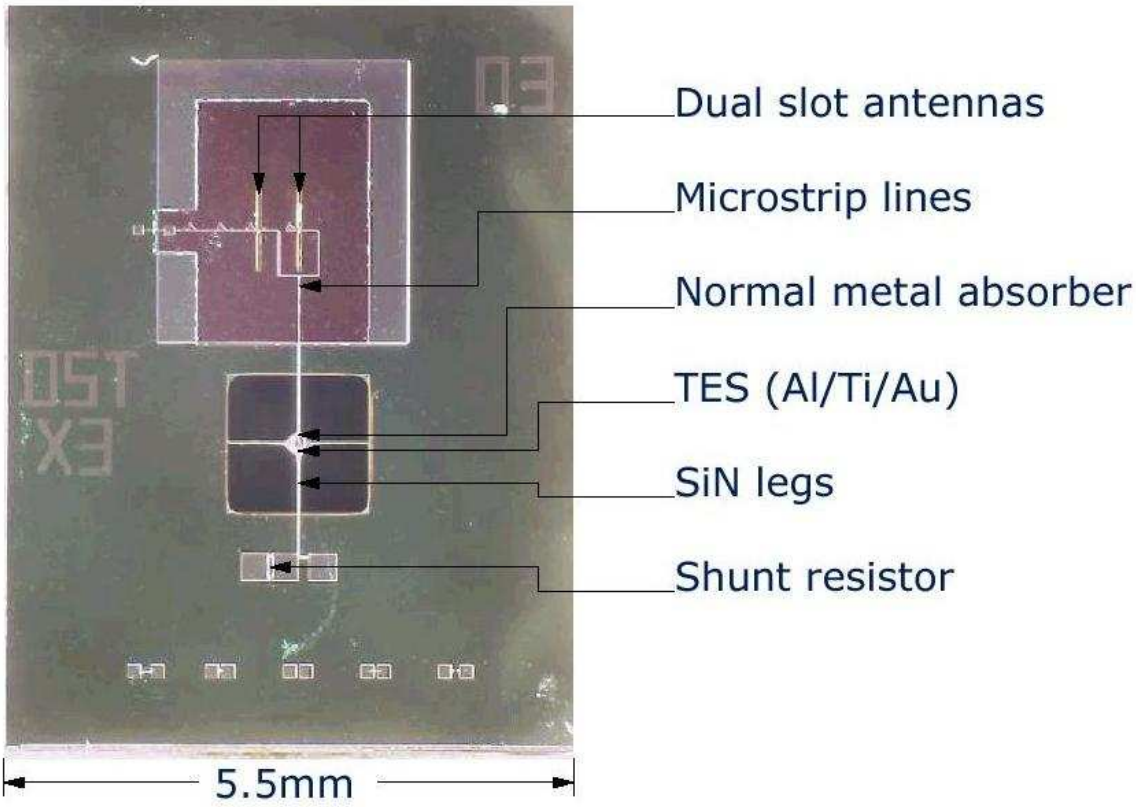


Figure 3.1: A fully fabricated single element device studied in this thesis. A zoom-in of the TES island is shown in Figure 3.2.

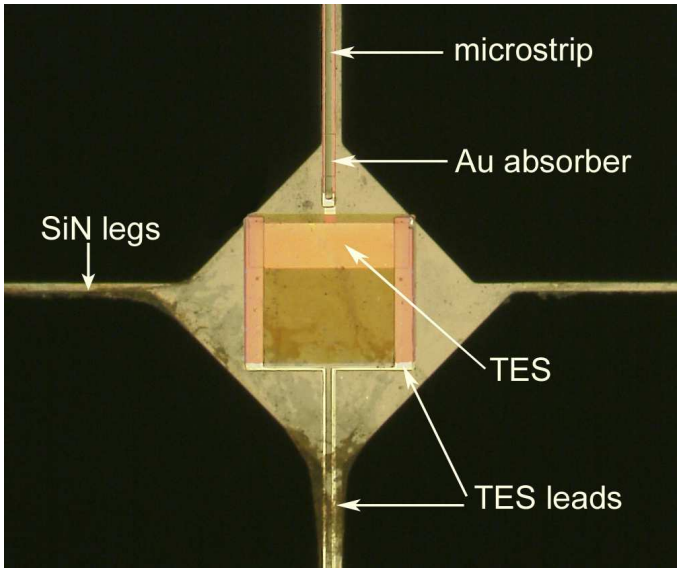


Figure 3.2: Photo of the TES island. For scale, the TES itself is 100 $\mu$m long by 33.3 $\mu$m wide.

## 3.3 Device fabrication

Our device consists of a thermally isolated superconducting sensor coupled to a dual-slot superconducting microstrip antenna. This concept has several complex fabrication issues. Since this device is a test structure, we wanted to make the design as robust as possible. We need to balance having the appropriate thermal isolation structure with having most devices survive the processing involved. We also need to balance our needs for the TES materials with maintaining its integrity through some of the harsh processes in fabrication.

Thermal isolation of the TES structure is provided by a thin support membrane made of 1$\mu$m thick silicon nitride. This is the same isolation mechanism used in the spiderweb bolometers. We want to make this thermal isolation structure very stable under the 'etch and release' while providing enough thermal isolation for the speed and noise performance of the device. We chose an island to support the TES with a four-leg support structure. The bare support legs are 7$\mu$m wide. The legs supporting the microstrip transmission line and the TES readout lines are each 16$\mu$m wide, and can be seen in Figure 3.2. This width was necessary to adequately and reliably support the thick transmission line structure.

To produce this structure, we start with a four-inch diameter silicon wafer and grow 200Å of silicon dioxide via wet air oxidation (WetOx) simultaneously on both sides of the wafer. A 1$\mu$m thick layer of silicon nitride is deposited using low pressure chemical vapor deposition (LPCVD), also on both sides of the wafer. After the metallization layers are applied, the legs/island structure on the top-side of the wafer is patterned and removed with a reactive ion etch (RIE). We stop the etch on the silicon dioxide layer using a UV interference pattern sensor during the etch. The backside window is patterned and etched in the same way, however the silicon dioxide on the backside only is removed in a buffered oxide etch (BOE). The device wafer is then wax-mounted to a six-inch backing wafer placed backside-up into a deep reactive ion etch, using $SF_4$ and $O_2$ plasma etchants. This process removes the silicon in the window down to the silicon dioxide and on the 'streets' that separate individual devices. The silicon dioxide layer provides enough etch selectivity to be a stop barrier for the plasma etch. The wafer is again placed into BOE to remove the exposed topside silicon dioxide in the window. The device wafer, which is still mounted to the backing wafer, is placed device side down into trichloroethylene to remove the wax. The individual devices are released and gently cleaned with acetone and isopropyl alcohol. The

relatively large width of our legs provides enough stability to remain intact while dipping gently in these solutions.

Transferring the signal in the microstrip transmission line to a thermal signal for the TES presented a challenge. A normal metal resistor is needed to short the transmission line and be in good thermal contact with the TES. The impedance at this resistor must be matched to the transmission line to minimize reflection. We chose to place the resistor on the bottom of the other layers to avoid steps in the thin gold film. The gold film is an order of magnitude thinner than an individual layer in the microstrip; 180Å thick for the gold versus 2000Å thick for each layer of the microstrip transmission line. However, terminating the top lead layer to the bottom ground plane through this resistor requires at least one layer in the microstrip to step over a layer that is of equal thickness3. This termination structure is shown in an optical photo in Figure 3.2, and in an SEM micrograph in Figure 3.3. A schematic of the cross section of the termination is shown in Fig. 3.4.

The length of the resistor, and hence its total impedance, is defined on the ground plane. This makes a reproducible resistance by eliminating alignment error that would cause varying resistances. The SiO layer covers the gold film and partially covers the second ground plane pad. The top niobium layer makes contact to the resistor by touching this second pad. The difficulty of this overlapping design is that the niobium and SiO layers are of approximately the same thickness (2000Å) which may cause breaks at the overlap edges. An arrow in Figure 3.3 shows the location of the potential breaks. We reduced this problem by using a multi-layer resist technique that creates a gently sloping edge profile. However, this difficult step structure produced the highest rate of failure in the devices. We lost 1/3 of our devices due to breaks in this region.

Another processing challenge involves maintaining the TES integrity throughout the various processing steps. The Al/Ti/Au trilayer is vulnerable to photoresist developer (which will etch the aluminum) and high temperatures could potentially cause interdiffusion between the layers. We deposited the TES and TES leads very early in the processing so that we could check that the transition temperature ($T_c$) of the superconducting film was in an acceptable range. We aimed for a $T_c$ of around 400mK. This means that the TES trilayer is exposed to various processes such as developer (a mild KOH mixture), RIE etching, and high temperatures of up to 120°C throughout the duration of the processing. To protect the TES we applied a thin 25Å layer of Ti on top of the Au layer, then applied a patch of the

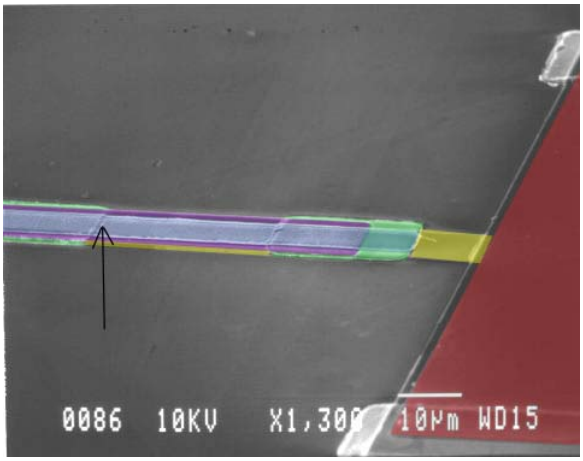


Figure 3.3: A false color SEM micrograph of the termination of the microstrip on the TES island. The microstrip line propagates the signal from the antenna (off picture to the left) to this termination region. A cross-section schematic of this region is shown in Figure 3.4 with the same color scheme. The region in red is the TES. The yellow region is the Au film that defines the terminating resistor then extends to the TES, initially designed for good thermal contact. The microstrip itself consists of the Nb ground plane in green, the SiO dielectric in purple and the Nb lead on top in blue. The arrow indicates the step where failures are most likely to occur as described in the text. Note that this micrograph was taken before the silicon nitride structure was defined.

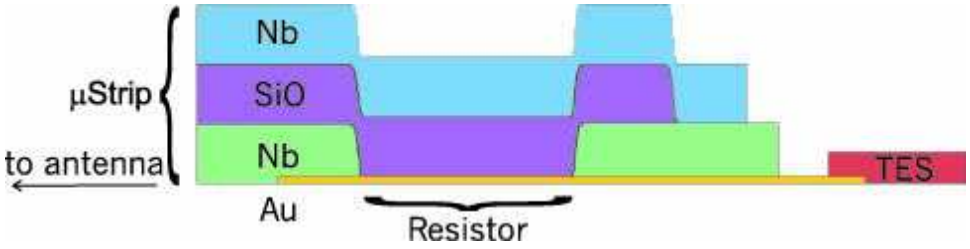


Figure 3.4: A diagram of the cross section through the termination of the microstrip on the TES island, not to scale. An SEM micrograph of this region is shown in Figure 3.3 with the same color scheme. The Au film is 180 Å thick, each Nb film is 2000 Å thick, the SiO dielectric is 2000 Å thick, and the TES itself is 840 Å thick.

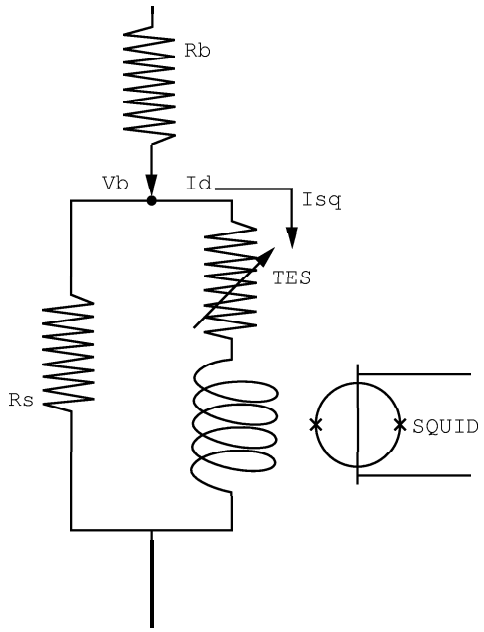


Figure 3.5: The TES electrical circuit. The current $I_d$ is reduced with a current limiting resistor $R_b$. A bias of $V_b$ is applied to the TES and a shunt resistor, $R_s$, in parallel with the TES. The TES is voltage biased when $R_s$ is small compared to the resistance of the TES. An inductor is included in the circuit to couple to the SQUID amplifier.

same 2000Å SiO layer to cover and protect the TES. We avoided using high temperatures in the processing (such as annealing) as much as possible. The transition temperature of our TES drops from that measured just after deposition compared to the that measured after the full fabrication and release. In the case of a 1-square device, the transition temperature dropped from $T_{c0} = 416$ mK to a final $T_c = 368$ mK. This could be due to some mild interdiffusion of the TES layers. However, it is reproducible and is within the operating range of between 350 and 450 mK for a $^3$He cooled testbed.

## 3.4 Electronics

We voltage bias our TES, as shown in Figure 3.5 [37]. We apply a voltage, $V_{appl}$, across the circuit. A fully charged battery will introduce the least amount of noise, especially important in low background-noise measurements such as measuring the noise in the device. However, for other applications, we use a commercially available Data Acquisition Card (DAC). This has the advantage of scanning through a range of voltages at a given speed.

A current limiting resistor, $R_b$, limits the bias voltage, $V_b$, applied to the TES and the

parallel shunt resistor, $R_s$. In this model the TES is a resistor $R(I,T)$, whose resistance is a function of both its temperature, $T$, and the electric current $I_d$ through it. An inductor, $L$ is included as the input coil of a dc SQUID current amplifier, which is kept at a temperature of 4 K. When the shunt resistor, $R_s$ is small compared to the TES resistance, the TES is voltage biased. In the next Chapter, we develop a mathematical description of the thermal and electrical behavior of this circuit.

## 3.5 Experimental setup

The detectors described in this thesis were tested in a $^4$He cryostat equipped with a $^3$He refrigerator, all from Infrared Laboratories [36]. An individual detector is mounted on a sample holder that is in good thermal contact to the $^3$He stage. The temperature of the $^3$He stage and the sample mount were monitored with a commercially available cryogenic Ge thermometer. Figure 3.6 shows a photograph of the dewar in operation. We use a Lake Shore Cryotronics 340 Temperature Controller [45] for monitoring the temperatures of the $^4$He stage and charcoal pump during cooldown and operation of the system. During measurements, we use a 500dc SQUID Controller from Quantum Design [66], the same company that produced the SQUID amplifiers in our system. To measure the Ge thermometers, the TES resistance, and to control the base temperature of our system, we use a Linear Research LR-700 AC Resistance Bridge [53]. When measuring noise, we use the Stanford Research Systems FFT spectrum analyzer [75].

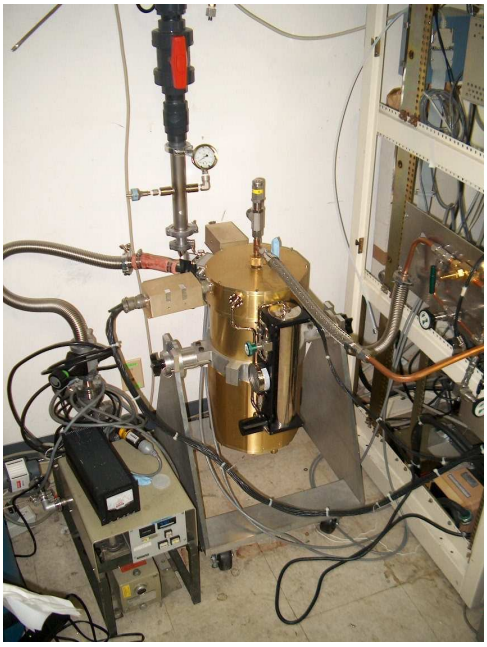

Figure 3.6: Cryogenic dewar used for dark measurements. The dewar, from Infrared Laboratories, is a $^4$He cryostat equipped with a $^3$He refrigerator. The holding tank for the $^3$He gas is located on the outside of the dewar and is visible in this picture as the shiny silver cylinder. A turbo pump is seen to the left of the dewar and is used to evacuate the dewar's vacuum insulation shield. To the right of the dewar is an instrument rack used to take measurements, the bottom of which is visible. Attached to the outside of this rack and seen at the far right of the picture is the valve setup for pumping on LHe to reduce its temperature. This system is located in the Microdevices Laboratory at JPL.

Figure 3.7: Filling the dewar with liquid helium.

# Chapter 4

# Millimeter-Wave Bolometers

A bolometer is a thermal radiation detector whose output is an electrical signal. Bolometers are very broad band detectors and are used from X-ray through millimeter-wave regimes [29, 10, 65]. Bolometers are the most sensitive direct detectors between 200 $\mu$m and 5 mm, a wavelength range that includes most of the CMB. The work in this thesis is concerned with bolometers in this range for sub-mm and mm-wave cosmology. In this chapter we will first give an overview of basic bolometer theory, then extend the theory to superconducting bolometers as it applies to this thesis. We will also discuss the main sources of noise in bolometers, and finally overview the problems with excess noise in superconducting bolometers.

## 4.1 Basic bolometer theory

A simple model of a bolometer is shown in Figure 4.1. It consists of an absorbing element of heat capacity $C$, which is connected to a thermal bath by a weak thermal link, $G$. A power $P$ is absorbed in $C$, and the detector temperature $T$ rises above the bath temperature, $T_0$. The heat then dissipates through the weak thermal link on a timescale of $\tau_{therm} = C/G$, and the absorbing element equilibrates back to its quiescent temperature assuming no additional incident power.

It should be noted that the single 'absorbing element' in this simple model is in practice a compound object including the absorber, the thermistor and the readout leads to the thermistor. The simple bolometer model describes the behavior well, but in certain cases the elements need to be accounted for separately. See Section 4.4 for a review of this case.

The bolometer measures the power of the incident radiation by measuring changes in temperature using an electrical resistance thermometer. The total power absorbed in the

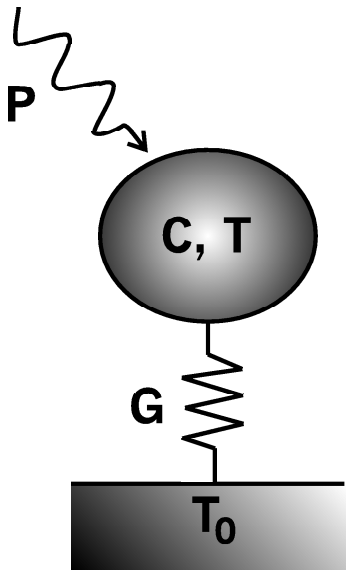


Figure 4.1: A schematic of a simple bolometer. The bolometer consists of an absorbing element of heat capacity $C$ which is weakly coupled to a thermal bath at temperature $T_0$ through $G$. When a power $P$ is absorbed in $C$, the temperature of the absorbing element increases, and equilibrates in a characteristic time scale of $\tau_{therm} = C/G$. This temperature rise is related to the power deposited in the absorber, which makes the bolometer a thermal radiation detector.

bolometer is a sum of the bias power and the incident optical power:

$$P = P_b + P_{opt} \tag{4.1}$$

One of the most important parameters in designing and characterizing a bolometer is the thermal conductance, $G$. This weak thermal link partially determines how fast the detector equilibrates to the bath temperature, and sets the phonon noise level as described in Section 4.3. The dynamic thermal conductance $G$ is given by

$$G = \frac{\mathrm{d}P}{\mathrm{d}T} \tag{4.2}$$

With no other input power than the Joule power, $P_b$, needed to bias the detector, the equilibrium temperature of the detector $T$ is determined by integrating equation (4.2) between the bath temperature $T_0$ and the detector temperature:

$$P_b(T) = \int_{T_0}^{T} G(T')dT' \tag{4.3}$$

We can now define the average thermal conductance $\overline{G}$:

$$P(T) = \overline{G} \cdot (T - T_0) \tag{4.4}$$

The thermal time constant of the detector, $\tau_{therm}$, is determined by how well the absorbing element can retain the heat divided by how easily the heat can flow to the heat bath.

$$\tau_{therm} = \frac{C}{\overline{G}} \tag{4.5}$$

The bias power, $P_b$, due to Joule heating in a resistive film held at a resistance $R$ with a bias $V_b$ is

$$P_b = \frac{V_b^2}{R} \tag{4.6}$$

We can now construct the power balance equation for an operating bolometer as described above. With no incident optical power, the electrical power dissipated is balanced by the thermal power lost through conduction to the bath and the power lost due to a temperature change in the bolometer. C is the heat capacity and does not change with time, so

$$\frac{V_b^2}{R} = \overline{G} \cdot (T - T_0) + C\frac{\mathrm{d}}{\mathrm{d}t}T \tag{4.7}$$

where $V_b$ is the bias voltage applied to the bolometer and $R$ is its resistance. Here we assume that the internal time constants (that is, the thermal equilibration times in the absorbing element) are fast compared to the thermal time constant. This holds for the detectors described in this thesis (Chapter 3) since the size of the absorbing element and the TES are very small. Also, we assume that the temperature gradients in the device are negligible.

The basic function of a detector is to convert a radiant input power to an output signal. The responsivity of a bolometer is the change in output signal per unit of absorbed signal power. The current responsivity is defined by

$$S_i \equiv \frac{\delta I}{\delta P} \tag{4.8}$$

## 4.2 Superconducting bolometer

This thesis describes measurements of a superconducting bolometer, also known as a transition edge sensor (TES). The superconducting film is voltage biased on its resistive transition. This strong resistance versus temperature dependance in the transition is used as a very sensitive thermometer. An input optical power causes changes in the bias current, $I$, which can be measured.

The TES device uses the Joule heating as a negative feedback to hold the temperature constant. When the device is voltage biased and the bath temperature $T_0$ is well below the transition temperature $T_c$, the superconducting film will self-regulate its temperature in the transition. This phenomenon is known as negative electrothermal feedback (ETF) [37]. The device is operating in equilibrium when the Joule heating exactly balances the heat loss to the bath. Functionally, ETF works when an incident optical power, $P_{opt}$, causes the temperature of the film to rise, which in turn causes an increase in the resistance. With this rise in resistance, the electrical power, $V_b^2/R$, decreases which compensates for the increase in incident power, keeping the device biased at the same point in the transition. The TES is a null detector; the output readout is the feedback current needed to hold the temperature constant.

The heat loss to the substrate from the superconducting film behaves like $K(T^n - T_0^n)$, where $K$ is related to the thermal conductivity and depends on material properties and geometry of the device; $n$ is a number whose value depends on the dominant thermal impedance between the substrate and the electrons in the superconducting film [37]. The thermal conductance in equation (4.2) is then

$$G = nKT^{n-1} \tag{4.9}$$

For thicker films, the thermal conductance behaves like $T^3$ ($n = 4$) because thermal boundary (Kapitza) resistance tends to dominate [42]. For thinner films depending on the temperature range, electron-phonon decoupling dominates and $n$ is 5 [81].

Now we have the tools to apply perturbations of a time varying signal of power $\delta P e^{i\omega t}$ to our TES [68]. This varying signal causes a temperature rise, $\delta T e^{i\omega t}$ which in turn causes a decrease in the bias power as described above. We modify the dark power flow equation (4.7) for this scenario. The power in the detector is a balance between the total power

dissipated in the bolometer and the power flowing to the bath:

$$P + \delta P \mathrm{e}^{i\omega t} + \frac{V_b^2}{R} - \frac{V_b^2}{R^2}\frac{\mathrm{d}R}{\mathrm{d}T}\delta T \mathrm{e}^{i\omega t} = \overline{G}\cdot(T - T_0) + \overline{G}\delta T \mathrm{e}^{i\omega t} + i\omega C \delta T \mathrm{e}^{i\omega t} \tag{4.10}$$

We define $\alpha$, a dimensionless parameter that measures the steepness of the resistive superconducting transition:

$$\alpha \equiv \frac{T}{R}\frac{\mathrm{d}R}{\mathrm{d}T} \tag{4.11}$$

We can separate equation (4.10) into a time-independent term:

$$P + \frac{V_b^2}{R} = \overline{G}\cdot(T - T_0) \tag{4.12}$$

and into a time-dependant term using our definition of $\alpha$ in equation (4.11):

$$\delta P \mathrm{e}^{i\omega t} = \left(\frac{P_b}{T}\alpha + \overline{G} + i\omega C\right)\delta T \mathrm{e}^{i\omega t} \tag{4.13}$$

As in the simple bolometer case where $P(T) = \overline{G}\cdot(T - T_0)$, we see that equation (4.13) can be rewritten as

$$\delta P = G_{eff}\delta T \tag{4.14}$$

where we have substituted an effective thermal conductivity, $G_{eff}$ for the term in parentheses. Analogous to electronic circuits with negative feedback [31], we can define a loop gain as the ratio of the change in bias power to the change in total power:

$$\mathscr{L}(\omega) = -\frac{\delta P_b}{\delta P_{tot}} \tag{4.15}$$

The change in bias power can be derived from its definition in equation (4.6):

$$\delta P_b = -\frac{V_b^2}{R^2}\frac{\delta R}{\delta T}\delta T \tag{4.16}$$

$$= -\frac{P_b \alpha}{T}\delta T \tag{4.17}$$

We now combine this result with equation (4.13), which added together give us the total change in power, and substitute them into equation (4.15). We find that the frequency-

dependent loop gain is

$$\mathscr{L}(\omega) = \frac{P_b \alpha}{GT(1 + i\omega\tau_{therm})} \tag{4.18}$$

where $\tau_{therm}$ is defined as $C/G$ in equation (4.5). The DC loop gain is then

$$\mathscr{L} = \frac{P_b \alpha}{GT} \tag{4.19}$$

The loop gain is a measure of the strength of the electrothermal feedback. Note that the gain rolls off at $\omega > 1/\tau_{therm} = G/C$

The electrothermal feedback shortens the time constant of a TES. This can be seen by looking at the responsivity for a TES. From the definition of current responsivity in equation (4.8) applied to the balance of power equation (4.13):

$$S_i = -\frac{1}{V_b} \frac{\mathscr{L}}{1 + \mathscr{L}} \frac{1}{1 + i\omega\tau} \tag{4.20}$$

$\tau$ is the effective time constant, or the thermal time constant reduced by a factor of $1 + \mathscr{L}$ due to electrothermal feedback:

$$\tau = \frac{\tau_{therm}}{1 + \mathscr{L}} \tag{4.21}$$

Likewise, the responsivity of the bolometer rolls off at a higher characteristic frequency, $\omega = 1/\tau$, than the loop gain. At frequencies $\omega \ll 1/\tau$ and large loop gain, the responsivity for a superconducting bolometer is just

$$S_i(0) = -\frac{1}{V_b} \tag{4.22}$$

Note that the responsivity of the voltage biased bolometer is independent of the bath temperature, which means that the bolometer is not sensitive to fluctuations in the cold stage temperature.

## 4.3 Bolometer noise theory

There are several noise sources in bolometers, all of which affect their performance [57, 58]. Ultimately we would like a detector which is 'background limited,' that is, when the dominant noise source is the random arrival rate and absorption of photons. This noise

floor sets the intrinsic sensitivity of a bolometer.

The effect of noise on the detector performance is quantified by the noise equivalent power, NEP. We define the NEP as the internal power change that produces a signal equal to the total rms noise. In more practical terms, the NEP is the minimum optical power a detector can accurately detect, or the signal power that yields a signal to noise ratio of unity. The NEP is calculated as the ratio between the output current noise, $I_n(\omega)$ and the current responsivity of the device.

$$\mathrm{NEP}^2(\omega) = \frac{I_n^2(\omega)}{S_i^2(\omega)} \tag{4.23}$$

The NEP is typically measured in $\mathrm{W}/\sqrt{\mathrm{Hz}}$.

The total NEP of our detector system is the sum in quadrature of all the NEP components since the fluctuations we are considering are uncorrelated sources. The main fundamental sources of the NEP in our system are Johnson noise, phonon noise, amplifier noise, and photon noise from both the signal being detected and from system background photons due to the finite temperature of the cryostat.

$$\mathrm{NEP}^2 = \mathrm{NEP}_{Jn}^2 + \mathrm{NEP}_{ph}^2 + \mathrm{NEP}_{amp}^2 + \mathrm{NEP}_{photon}^2 \tag{4.24}$$

Any resistor has Johnson noise which is due to the thermal fluctuations of the electrons. In a resistor, the Johnson noise can be derived by considering a noiseless resistor in series with an impedance matched noise source. The power dissipated in the resistor is equal to the thermal fluctuations:

$$I^2 \cdot 2R = k_B T \Delta f \tag{4.25}$$

where $I$ is the current applied to a resistance $R$ at temperature $T$ in Kelvin, and $k_B$ is Boltzmann's constant and $\Delta f$ is the bandwidth in Hz. The current noise corresponding to these thermal fluctuations is then

$$I_n = \sqrt{\frac{4k_B T \Delta f}{R}} \tag{4.26}$$

The Johnson noise in a TES can be derived in much the same way by applying a noiseless resistor and a noise voltage generator in series with the TES. The Johnson noise in a TES

of resistance $R$ at a temperature $T$ and of responsivity $S$ as expressed as a contribution to the NEP per unit root-bandwidth is

$$\mathrm{NEP}^2_{Jn} = \frac{4k_BT}{R|S|^2}\left(\frac{\tau}{\tau_{therm}}\right)^2\left(\frac{1+i\omega^2\tau^2}{1+i\omega^2\tau^2_{therm}}\right) \tag{4.27}$$

Electrothermal feedback suppresses the Johnson noise for frequencies well below $1/\tau$. Mather first described this process in detail in reference [57] for a general bolometer. It has been expanded for the case of strong electrothermal feedback in a TES by Irwin [37] and Lee [48].

Phonon noise is thermal fluctuation noise caused by the random propagation of phonons between the detector and the heat sink through the thermal link. The phonon noise varies with frequency just as the signal, so the NEP is frequency independent.

$$\mathrm{NEP}^2_{ph} = \gamma 4k_BT^2\overline{G} \tag{4.28}$$

where $\gamma$ is a factor of order unity for the dielectric supports in the case of our detectors [37]. This factor represents the adjustment to the thermal fluctuation noise for the gradient in temperature along the thermal link [57].

We use a low noise SQUID amplifier to read out the TES signal. We can generically model the NEP contribution with the experimentally measured amplifier noise, $I_n$:

$$\mathrm{NEP}^2_{amp} = \frac{I^2_{n,SQUID}}{|S_i|^2} \tag{4.29}$$

The current noise from a typical SQUID amplifier can range between 1–20pA/$\sqrt{Hz}$ depending on the specifics of the amplifier.

When the detector is illuminated with incident radiation, there is shot noise due to the random arrival rates of the photons. This noise is inherently irreducible. The photon NEP is approximately the square root of the photon flux multiplied by the energy per photon:

$$\mathrm{NEP}^2_{photon} \approx \sqrt{2P_{opt}hc/\lambda} \tag{4.30}$$

Typically the required threshold noise level of a detector is set by the wavelength detected, $\lambda$. However, different observing conditions can introduce other non-intrinsic noise, such

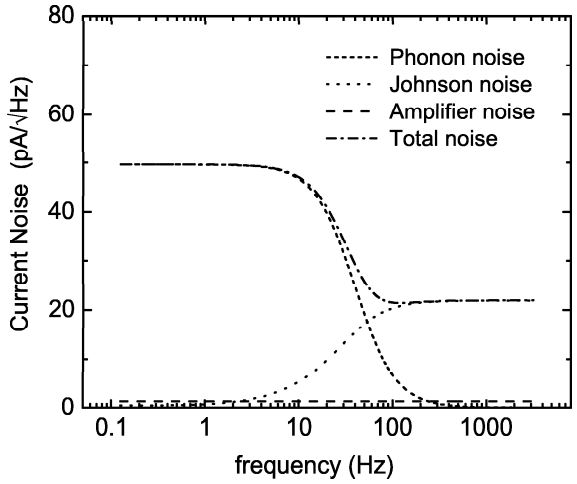


Figure 4.2: An example of current noise in a TES. This spectrum is a plot of the components in equation (4.31) versus frequency with no optical input. The Johnson noise is represented by the dotted line and rolls off at frequencies below $1/\tau$, given by equation (4.21). The phonon noise is represented by the short-dashed line and has the same frequency dependance as the responsivity of a TES, given in equation (4.20). The amplifier noise is low and represented by the long-dashed line. The total noise is represented by the dash-dot line and is the sum in quadrature of these three components.

as atmospheric fluctuations when observing on the ground. The photon shot noise term dominates at low incident optical power and at high frequencies. A more detailed discussion of photon noise can be found in reference [68].

For a direct comparison with measurements, it is useful to write expression (4.24) in terms of a current noise referred to the SQUID amplifier input.

$$I_n^2 = \gamma 4 k_B T^2 G |S_i| + \frac{4kT}{R}\left(\frac{\tau}{\tau_0}\right)^2\left(\frac{1+i\omega^2\tau^2}{1+i\omega^2\tau_0^2}\right) + I_{n,SQUID}^2 + I_{n,optical}^2 + I_{n,excess}^2 \quad (4.31)$$

We have also included an excess noise term that encompasses any noise contributions from other sources. An example of current noise plotted against frequency is shown in Figure 4.2, where only the first three components in equation (4.31) are plotted.

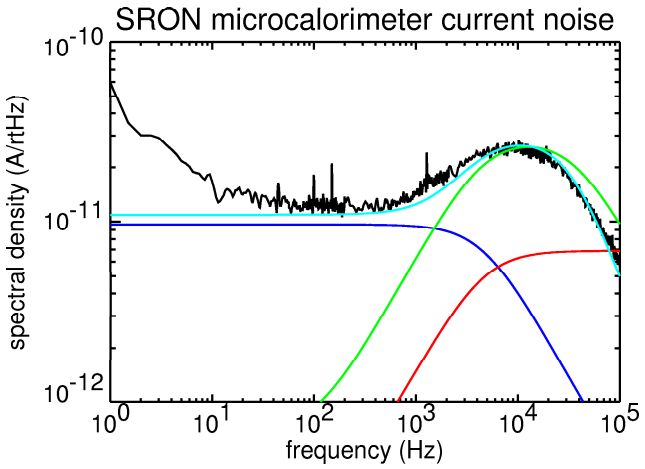


Figure 4.3: An example of excess current noise in a TES. This spectrum is of a Ti/Au TES with Cu absorber, described in reference [14] at the Space Research Organization Netherlands (SRON). The excess noise is modelled as an extended heat capacity coupled with a finite thermal conductance due to to the TES as described in the text, and plotted as the green line. Courtesy P. de Korte and SRON.

## 4.4 Excess noise problems

Historically, TES detectors have been plagued with excess noise problems. Over a wide variety of superconducting films, groups find noise behavior above those outlined in Section 4.3. Typically this excess current noise in TES films appears as a broad peak at high frequencies (500–10,000 Hz), an example of which can be seen in Figure 4.3. Although there has been much discussion at conferences and in personal communications about the cause of this excess noise, very little has been published. Groups working on TES detectors mostly engineer devices for a particular application, and hence look for low noise devices rather than attempt to explain anomalous behaviors.

This section is not meant to be an exhaustive review of all sources of excess noise, as that is beyond the scope of this thesis. Rather, it is meant to be a review of the literature to date to provide the reader with a background on the subject.

The detector groups at Berkeley [23] and at the Space Research Organization of the Netherlands (SRON) [14, 30] first attempted to model and explain the excess noise in their TES devices. Although they use different terminology and have different TES materials (Ti/Al for Berkeley and Ti/Au for SRON), their approach is similar. Both use an extended heat capacity model that incorporates each element of a TES detector. This is an extension

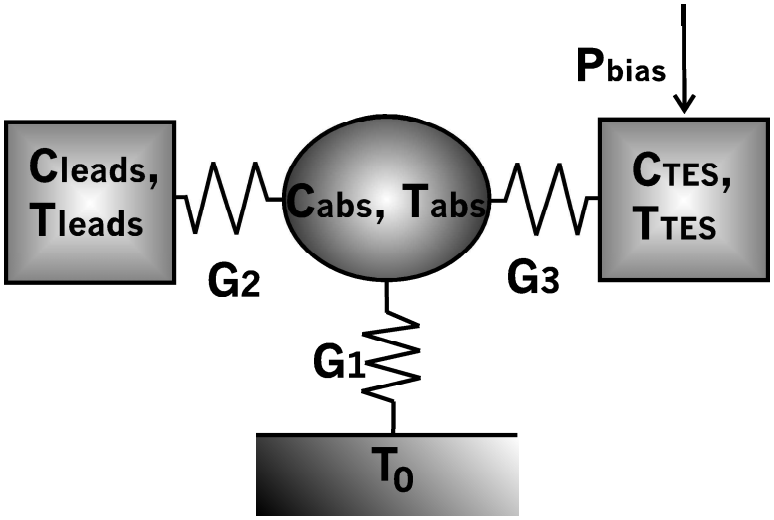


Figure 4.4: A schematic of the extended heat capacity model used in references [23] and [30] to explain an excess noise peak at high frequencies. Instead of lumping together the various components of a bolometer (see Figure 4.1), the extended heat capacity model separates them out into discreet heat capacities connected by their own thermal conductances.

of the simple model as described in Section 4.1 and used in the canonical Mather papers [57, 58]. The extended heat capacity model breaks the single heat capacity detector into an absorber heat capacity $C_{abs}$, a TES heat capacity $C_{TES}$, and in the case of the Berkeley group, a leads heat capacity $C_{leads}$ (see Figure 4.4). Elements can be lumped together only if they have dimensions shorter than $l = \sqrt{\kappa/2\pi fc}$, the characteristic length that a heat pulse propagates in a time $\tau = l^2 c/\kappa$, where $c$ is the specific heat and $\kappa$ is the thermal conductivity. This approach can be generalized to an arbitrary number of thermal masses, applying the small signal analysis to all. The power balance equation in (4.7) becomes a matrix equation and can be solved for the current spectral density. The Berkeley group fabricated devices with different heat capacities and found in general that the higher the heat capacity, the lower frequency the peak of the excess noise and the greater the relative amplitude of the peak. It should be noted that their heat capacities are dominated by the leads, which are a Ti/Al/Ti/Al quadrilayer, and they suggest minimizing the heat capacity in all elements. The SRON group uses the term 'thermal fluctuation noise' or TFN for short, for these noise sources and attributes them to a finite internal thermal conductance of the TES [30]. The TES TFN is proportional to the bias current $I$ and $\alpha$, the steepness of the transition. The major drawback of this model is that it is not rigorous, because both

$G$ and $C$, the thermal conductance between the individual elements and their associated heat capacities are not accurately known [23].

Edge effects parallel to the direction of the current appear to be important in understanding anomalous behavior in a TES. This effect was first noted by the electromagnetic technology group at the National Institutes of Standards and Technology in Boulder (NIST), detailed in reference [29]. The physics of how the edges induce excess noise and degrade superconducting transition profiles is not understood. NIST posits that the quality of the TES film is degraded at the edges due to fabrication errors that cause reduced proximity coupling of the films (the proximity effect is discussed in Chapter 3), either by chemical degradation or through poor physical contact. They solve the problem by adding strips of thick normal metal on the edges to create a consistent boundary condition. This increases $\alpha$, the steepness of the transition, and reduces the excess noise.

Groups from University of Jyväskylä, Helsinki University of Technology and SRON have altered the geometry of the TES to eliminate the edges parallel to the current [54]. Dubbed a CorTES, it is an annulus with one lead attached to the center and the other lead surrounding the outer edge. This causes the current to flow in the radial direction, eliminating the edges in rectangular TES geometries. However the Ti/Au devices studied still show excess noise, especially at low bias voltages. This excess noise cannot be explained by the extended heat capacity model described above. They instead explain this excess noise as 'fluctuation superconductivity noise' (FSN) arising from resistance fluctuations in the film due to thermal fluctuations of the phase boundary [54]. They note that these fluctuations should be present in all TES devices, but may not be observable depending on how the phase boundaries present themselves.

Work is being done by other groups to investigate and control the boundary conditions of the TES to understand the phenomenon in more detail. Both NIST and the detector group at NASA Goddard Space Flight Center (GSFC) have mentioned in private communications that they are developing TES films of varying geometries, looking for a connection to the edge effects. M. Lindeman (GSFC) has been applying a complex impedance technique in an attempt to measure the heat capacity of the TES through the phase transition. This information can lead to a better understanding of the mechanics involved in the transition and the sources of the noise. This technique will be discussed in detail in Chapter 6.

A more phenomenological approach is taken by GSFC in explaining their excess noise in

Mo/Au TES devices [52]. They are able to fit the excess high frequency peak by including a voltage noise source, akin to Johnson noise. Their excess noise is dependent only on the resistance of the TES and independent of bias voltage and temperature. They do note however, that their smallest device, i.e., the one with the lowest heat capacity, has the least amount of excess noise. This is consistent with the results from the extended heat capacity model.

Another source of noise possibly inherent to the superconducting film itself is flux-flow noise of vortices [41]. Although to date there is no literature dealing specifically with this phenomenon in TES devices, the concept often dominates conversations at conferences and meetings. It is mentioned by the Finnish group in reference [54] and attributed to edge effects. In the presence of a magnetic field perpendicular to the film, vortices form. If a current is applied across the film, the vortices will move and dissipate power. There should be a type of shot noise associated with the movement of the vortices. In 1965 van Ooijen and van Gurp found such a spectrum, but it only behaved like the theoretical expectation at the highest currents and fields [78]. At lower fields, the moving entities carried more than a single flux quantum. This has been attributed to pinning, where bundles of vortices move to overcome a pinning barrier. We can conclude that flux motion is generally correct, but a real film has a complex defect structure that complicates the picture.

The state of the field in understanding the anomalous excess noise present in most TES detectors is very immature. There are general strategies to try to avoid excess noise. Reducing the heat capacity of the components is one of the easiest and most accepted ways of avoiding excess noise. In the same vein, keeping the detector clean and free from residue that tends to have a high heat capacity will assure that you are only looking at the heat capacity of the TES system. Geometry and edge effects appear to be important, however more work needs to be done to fully understand their contributions.

# Chapter 5

# Experimental Results

## 5.1 Introduction to results

In this chapter we describe experimental results from four single element devices. The four devices, dubbed 'alpha,' 'beta,' 'gamma,' and 'delta,' all originated from the same processing wafer. The layers were deposited at the same time, so the properties of the layers, such as thickness and electrical resistance, are uniform across the wafer to better than 10%. The only difference between the devices is the geometry of the TES film. Devices alpha and gamma have TES film dimensions 100 $\mu$m by 10 $\mu$m, and have a cold normal state resistance of 5 $\Omega$. Device beta has TES film dimensions 100 $\mu$m by 33.3 $\mu$m, and a cold normal state resistance of 1.5 $\Omega$. Device delta has TES film dimensions 100 $\mu$m by 100 $\mu$m, and a cold normal state resistance of 0.5 $\Omega$. These parameters are summarized in Table 5.1. Perhaps the biggest difference between the individual devices is the post-processing evolution. In the final step, the release of the devices, each one has a different local environment. For example, scum and particles can deposit themselves on the devices during the release in the solvent used to removing wax and photoresist. In addition, the mounting and testing of the devices is not done in a clean environment, so particles can accumulate on the devices. The results for these four devices will be presented as a group, with similarities and differences highlighted.

Table 5.1: Summary of the four devices studied in this thesis.

| | alpha | beta | gamma | delta |
|---|---|---|---|---|
| $R_{normal}$ | 5$\Omega$ | 1.5$\Omega$ | 5$\Omega$ | 0.5$\Omega$ |
| length | 100$\mu$m | 100$\mu$m | 100$\mu$m | 100$\mu$m |
| width | 10$\mu$m | 33.3$\mu$m | 10$\mu$m | 100$\mu$m |

The intention of this chapter is not only to outline the specific results of the four devices, but also to serve as a handbook for the scientist who is first embarking on testing transition edge superconducting bolometers. The results are presented in the order in which they were acquired, and the procedures are outlined. First, one does 'basic measurements' which include taking load curves at different base temperatures, and measuring the device time constant under different conditions. Next, tests can be done using a separate heater on the TES island, if there is one. The more difficult measurements are usually those done in a low-noise environment. This includes taking noise spectra and can include complex impedance measurements, the latter of which is described in Chapter 6. The noise spectra are generally the least understood aspect of TES devices, and the interpretation can be tricky due to the many possible sources of excess noise.

## 5.2 Basic measurements

The 'basic measurements' are ones that do not require a low-noise testing environment. These include measuring the superconducting transition, measuring load curves, measuring the time constant of the device and probing the TES with an on-island heater.

### 5.2.1 Superconducting transition

The easiest way to obtain a resistance versus temperature curve for TES devices is a four-point resistance measurement of the film in a cryostat with varying base temperatures. The four-point measurement must be done on a TES device that is properly heat sunk. The power used to probe the resistance warms up the device enough to change the characteristics of the R vs. T curve if it is thermally isolated. For thermally isolated TES films, the low thermal conductance of the silicon nitride support legs prevents the heat from being dissipated out quickly, and the heating might put the device in a different part of the transition. To avoid these problems, one row of devices is diced off the wafer before the thermal isolation architecture is processed. Since the TES film and the electrical leads are the first layers to be deposited, we can discover problems with the TES film, such as an improper transition temperature. This way one can start on a new wafer and not waste weeks of processing due to a poor TES film.

The resistance and temperature relation for an unreleased Al/Ti/Au TES film is shown

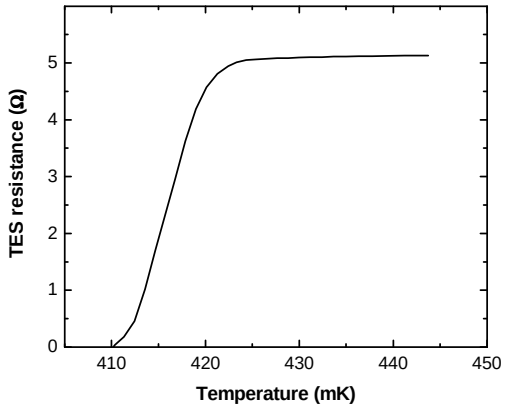


Figure 5.1: Resistance vs. temperature of an Al/Ti/Au film. This curve was taken as a 4 point measurement of a 10-square TES film that was on a solid substrate, i.e., not on a thermally isolated island.

in Figure 5.1. The transition temperature of the film is 417 mK. Its width is approximately 10 mK. The steepness of the transition can be characterized by $\alpha = T/R\ dR/dT$, which is approximately 100 in the center of the transition. The 'bottom' of the transition is where the resistance is very small, or equivalently at a low bias voltage while in operation. The 'top' of the transition refers to points where the TES is close to normal. The bottom of the transition is generally much steeper than the top.

### 5.2.2 Load curve

Measuring the input voltage versus the output current for devices is key in understanding some general TES properties. Perhaps of most importance while in the lab testing a new device, the load curve can be used to determine if the device has a superconducting transition in the thermodynamic range of the cryostat.

The load curve is easiest to understand in terms of an output current from the SQUID vs. an input device current. Figure 5.2 shows an example of a typical TES load curve taken at a bath temperature well below the transition temperature of the TES. There are three distinct regions in the load curve. At the lowest applied currents, the device is superconducting. Since all the input current is being detected by the SQUID, the slope of this line is unity. At some finite current the device will begin to transition, and its resistance

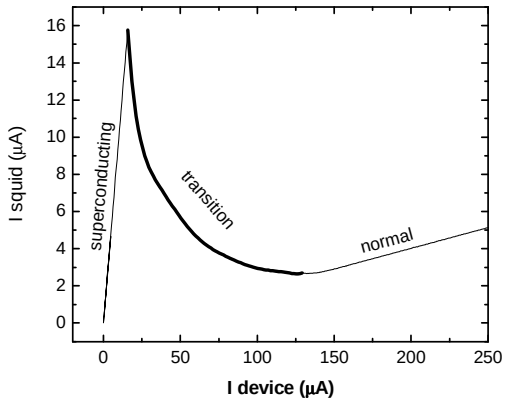


Figure 5.2: Example load curve of a TES. The curve has three distinct regions: At the lowest bias, the device is superconducting and the current applied is the same as the current through the SQUID. At the highest bias, there is sufficient power to drive the device normal. In between, the device is in the superconducting resistive transition.

increases. The slope in the load curve becomes negative through this transition, and its shape is governed by the specific transition properties of the device. When there is sufficient bias to drive the TES normal, the load curve becomes a straight line with constant slope, exactly as expected for a resistor. The slope of this line is set by the shunt resistor and the TES normal-state resistance acting in series.

One can obtain a set of load curves at a series of bath temperatures, as shown in Figure 5.3. As the bath temperature approaches the TES transition temperature, less current is needed to drive the device through its superconducting transition. Note that at warmer bath temperatures the load curve begins to become more and more distorted in the transitions. Similar behavior has been noted for all four devices, however there is little correlation of the current where this behavior appears. It is possible that this is in part due to the difficulties of measuring a device so close to its superconducting transition. Another explanation could be a region in the superconducting film that is proximitized due to the gold layer that provides thermal contact to the absorber. This would cause a region with a different critical temperature than the majority of the TES film, and would tend to disfigure the single-transition film load curve.

One of the key parameters that characterizes a bolometer is $G$, the thermal conductance to the heat bath. From Chapter 4, $G = dP/dT$. We therefore need to measure the power

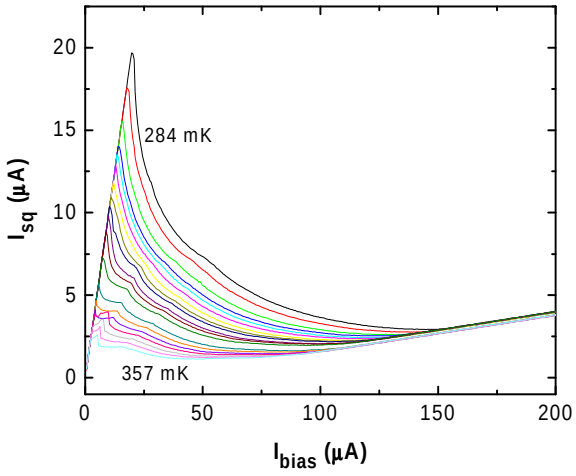


Figure 5.3: Set of load curves of a TES at different bath temperatures. The load curve with the coldest bath temperature is the top black curve at 284 mK, while the warmest is the curve on the bottom at 357 mK. The warmer the bath temperature, the smaller the bias needed to push the superconducting film into the transition. The curves are superimposed in the normal regime, yielding a normal state resistance of 0.5 Ω for this particular device.

in the TES with respect to the temperature. In the superconducting transition, the TES device power should remain constant due to the electrothermal feedback from the voltage bias. One can calculate the power dissipated in the TES using

$$P_{TES} = \frac{V_{bias}^2}{R_{TES}} \tag{5.1}$$

The quiescent bias power of the TES through the transition is shown in Figure 5.4 by applying equation (5.1) to a load curve. One can calculate this constant power in the transition for a given range of bath temperatures. The largest error in this measurement is due to the SQUID amplifier losing lock at the bottom of the transition. The SQUID will often lose count of the number of flux quanta here. When analyzing the data, we need to insert an integral number of flux quanta at the peak in the bias curve to compensate for this loss of lock. When adding these flux quanta, we look for alignment in the high bias regions, as is the case in Figure 5.3. The flat region in the power versus bias curve can in practice have a slight slope. The error from these experimental effects is estimated to be approximately 5% for our data. Figure 5.5 shows the relationship between power and temperature for our device. We can fit this data to equation (4.9) in Chapter 4. We

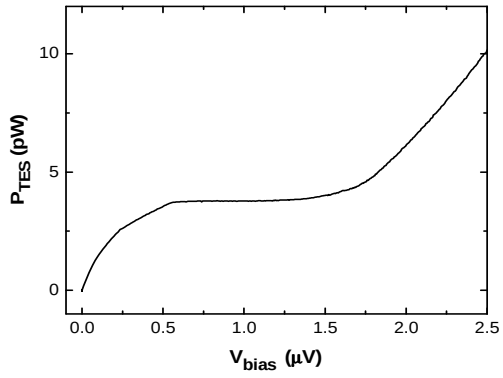


Figure 5.4: Quiescent bias power of TES through transition. When the device is voltage biased in the superconducting transition, the electrothermal feedback keeps the power in the TES constant.

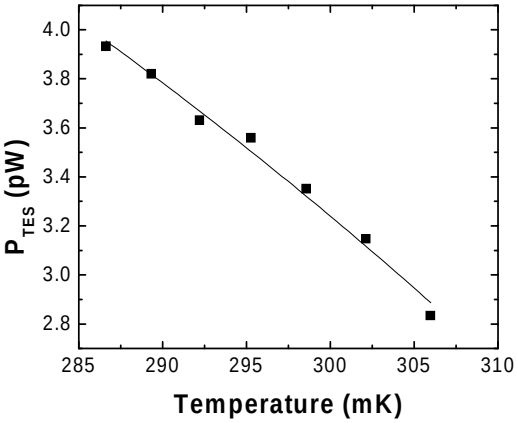


Figure 5.5: Power versus temperature in the TES. These points are taken at a range of temperatures at the constant power of the TES in the superconducting transition, as in Figure 5.4. The curve is the relation $P = k\left(T^n - T_0^n\right)$ as described in Chapter 4. The thermal conductance, $G$ is then $\frac{dP}{dT} = nkT^{n-1}$. Our four devices showed $G = 55$ pW/K to within 6%

discover that all four devices have $G = 55$ pW/K to within 6%. We expect this value to be 46 pW/K, based on the geometry of the silicon nitride legs and the empirical measurements of past silicon nitride films. The small difference of 16% between measured and expected $G$ can be attributed to size variations in the legs due to lithographical errors and over-etching of the silicon nitride.

### 5.2.3 Time constant

To measure the effective time constant of the device, the device must be pulsed with an input power and the response examined. The effective time constant is the thermal time constant, $\tau_{therm} = C/G$, reduced by electrothermal feedback in the voltage biased TES. We chose a measurement method that would be electrically independent of the TES bias circuit. To achieve this, we used a red LED coupled to the TES via an optical fiber to heat the TES island directly. Care was taken to prevent stray LED radiation by coating the LED in opaque paint. The LED pulsing technique has the advantages of being electrically disconnected from the device and of being a relatively quick and easy measurement to make. Although the LED does not emit light in the bandwidth of our antenna, it does simulate optical power by dissipating power directly on the TES island. The LED was driven with a pulse generator and the TES response was measured on an oscilloscope. The fastest time constant measured was 437$\mu$s in device alpha biased at 3$\mu$V, approximately 40% up the transition as shown in Figure 5.6. Note that the time constant of the LED itself is several $\mu$s, much shorter than the time constants measured. The error on the time constant measurement is due to the scatter of data and the quality of the fit. It is typically 2% for most curves. Occasionally, however, the experimental error can be up to 10% particularly for noisy data. Since we do not know the coupling efficiency of the LED to the island, we are not able to measure how much power is deposited directly into our TES with this technique.

A set of time constants through the superconducting transition yields information which is important when modelling the noise behavior. One example of the time constant through the superconducting transition is given in Figure 5.7 for device delta. The time constant of the device is shortest where the electrothermal feedback is the strongest, i.e., where $\alpha$ is largest. Likewise, at the top and bottom of the transition the device has the longest time constants because the electrothermal feedback is the weakest. For our four devices, those

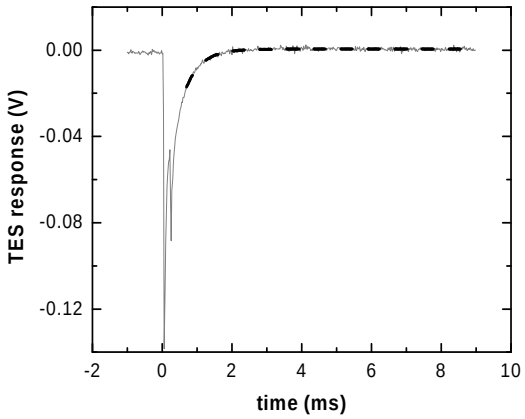


Figure 5.6: TES response (gray) to an LED pulse. The response of the device is fit by an exponential decay $e^{-t/\tau}$, as shown by the bold dashed line. This curve has the smallest time constant measured: 437$\mu$s biased at 3$\mu$V in device alpha.

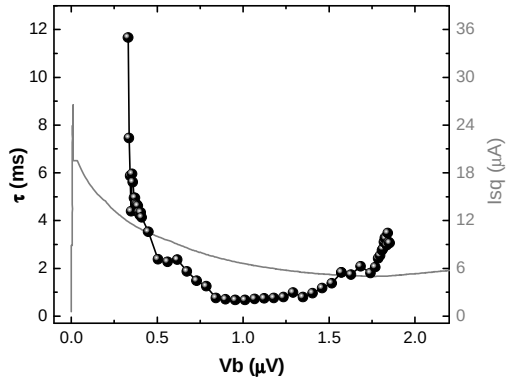


Figure 5.7: Time constants through the superconducting transition are shown with the solid dark circles. The approximate bias curve corresponding to the time constants is given by the gray line, and the y axis is labelled on the right in $\mu$A. Note that at the top and bottom of the transition the device has the longest time constants because the electrothermal feedback is the smallest.

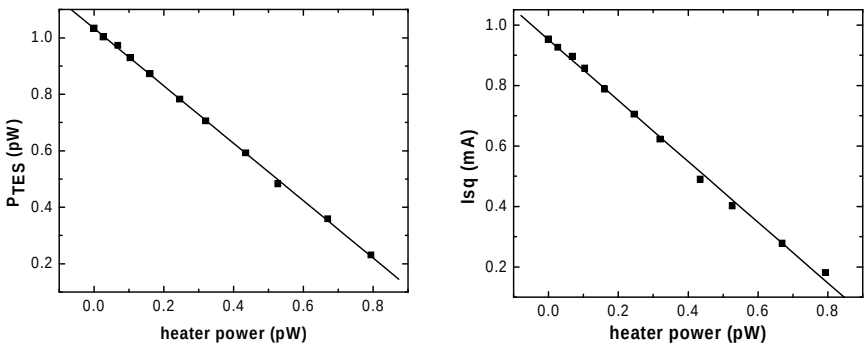


Figure 5.8: Results of the on-island heater applying power to TES island. Although these curves are equivalent, they demonstrate two important behaviors of our devices. In (a) we show that when the loop gain gets very large the slope of $P_{TES}$ vs. $P_{heater}$ should approach -1. We find this linear behavior to within 2%. In (b), with the same limit of a large loop gain, the dc current responsivity ($S_i = dI/dP$) should be well represented by $-1/V_{bias}$. Figure (b) was taken at a bias voltage of 1 $\mu$V, and the slope of the current versus heater power line is -1$\mu$V$^{-1}$ to within 1%, just as we expect.

with the smallest heat capacity had the fastest overall time constants, as expected.

### 5.2.4 Heater

The Au terminating resistor was used as a heater to apply a known power to the TES to study its current responsivity and linearity. Applying a bias across the resistor on the thermally isolated island deposits heat into the TES, simulating optical power in a controlled manner. While applying bias to the heater, we measure load curves of the TES, which yield current responsivity and the transient power deposited in the TES. The loop gain of the TES is given by $\mathscr{L} = -dP_b/dP_{tot}$, where $P_{tot}$ is the total power dissipated in the device, i.e., bias power plus heater power. As the loop gain gets very large, the negative of the slope of bias power vs. heater power approaches unity. Our device shows this linear behavior to better than 2% as seen in Figure 5.8a. We also measure the current response of the TES for a given bias voltage at different applied heater powers. The current responsivity is given by: $S_i = dI/dP$. Again, we take the limit as the loop gain becomes large and while taking a DC measurement the current responsivity becomes: $Si = -1/V_{bias}$. For a bias of 1$\mu$V we expect a DC current responsivity of -1$\mu$V$^{-1}$, which is shown in Figure 5.8b to be matched to better than 1%.

In the future, we will be able to measure and compare the time constants using the

on-island heater and LED technique described above.

## 5.3 Noise

The characteristics of the noise spectrum is critical in characterizing a TES detector. The level of the noise sets the sensitivity of the detector. For our application of CMB detection, the signal is very low power, so the sources of noise must be understood in order to achieve optimal performance.

Our four devices showed different phenomenological noise behavior. In this section, I hope to take the reader through the process of understanding their noise behavior. First we will look at the noise spectra compared with the basic theory of phonon noise, Johnson noise and SQUID noise as outlined in Section 4.3. Next we will look at the general behavior of the excess noise. Finally we will attempt to use the extended heat capacity model to fit the excess noise with varying success.

Current noise spectra from all four devices were taken over a range of frequencies and through the superconducting transition. The major challenge in taking noise spectra is reducing the amount of outside interference. These sources are potentially many, and often finding them is a challenge. Unnecessary instruments should be switched off, especially those electrically connected to the experimental setup. Even those that are not directly connected can create spurious noise sources. For low frequency spectra, movement in the room can cause extra noise. We particularly noticed this when colleagues would move across the floor in a chair with wheels or while closing the door to the room or even when tapping a LHe dewar in the vicinity of the cryostat. Unfortunately, most of this low frequency pickup was unavoidable as the room housing the experimental setup was crowded with several other projects.

Steps were taken to minimize pickup and spurious noise sources. Noise spectra are best taken at night or on the weekends when there is minimal activity in the room and building. All wires leading into the dewar are RF-filtered. The device bias is provided with a battery to reduce 60 Hz pickup, and fully charged to reduce low frequency noise. The best prevention against spurious noise sources, however, is to place a shield around the device. Since our TES superconducting film is especially susceptible to magnetic interference, a niobium shield at the same temperature as the device surrounds the device with small

holes for wire feed-through ports. This superconducting barrier is quite good at shielding magnetic fields. However, there is evidence that it is imperfect since pinning sites tend to freeze into the material. Despite our best efforts, we frequently found different pickup sources. For example, when testing device beta, we found a strong 1 Hz signal. We think this is due to a resistance bridge on a neighboring experiment. In device delta we found high frequency power at 402 Hz and corresponding harmonics. The source of this pickup was never found. For future experiments, other magnetic shielding such as a mu-metal barrier or conetic alloy should be installed in addition to the niobium shield already in place.

### 5.3.1 Data compared with basic theory

First, we compare the noise from our devices against the known sources of noise. We take several noise traces with different frequency spans. This is to ensure the best resolution and coverage at low frequencies as well as at high frequencies. The spectra are then pieced together to cover a larger frequency range. We also take spectra at bias points through the entire transition to understand the behavior with respect to the bias.

The first device we tested, device alpha, turned out to have noise behavior close to the known sources of noise. We found that the best behavior was at the lowest bias voltages, so we concentrated on this regime. Figure 5.9 shows four selected current noise plots from this device, along with the expected noise from the phonon noise, Johnson noise and SQUID noise. All spectra were taken at a base temperature of 282 mK. The noise from the device at all biases matched the basic theory at frequencies below 100 Hz. In this range, the NEP of the device is $1.55\pm0.05\times10^{-17}$ W/$\sqrt{Hz}$. Above this frequency, we see some excess noise. At a bias voltage of 0.301 $\mu$V, or 1% up the transition, the noise at frequencies greater than several hundred Hz is only 50% above the expected value. However, at higher bias voltages, this excess noise increased and the characteristic bend in the spectrum disappears completely. There is also a small noticeable peak at 4500 Hz in all spectra taken. The source of this broad peak is unknown.

Device beta, a 3-square device, has both similar and dissimilar noise characteristics compared to device alpha. Four selected noise traces are shown in Figure 5.10. Again, at frequencies below 100 Hz the noise in device beta agrees extremely well to the basic theory, similar to device alpha. In this range, the NEP of the device is $2.0\pm0.3\times10^{-17}$ W/$\sqrt{Hz}$. At frequencies above 100 Hz, however, the noise behavior is very different to device alpha.

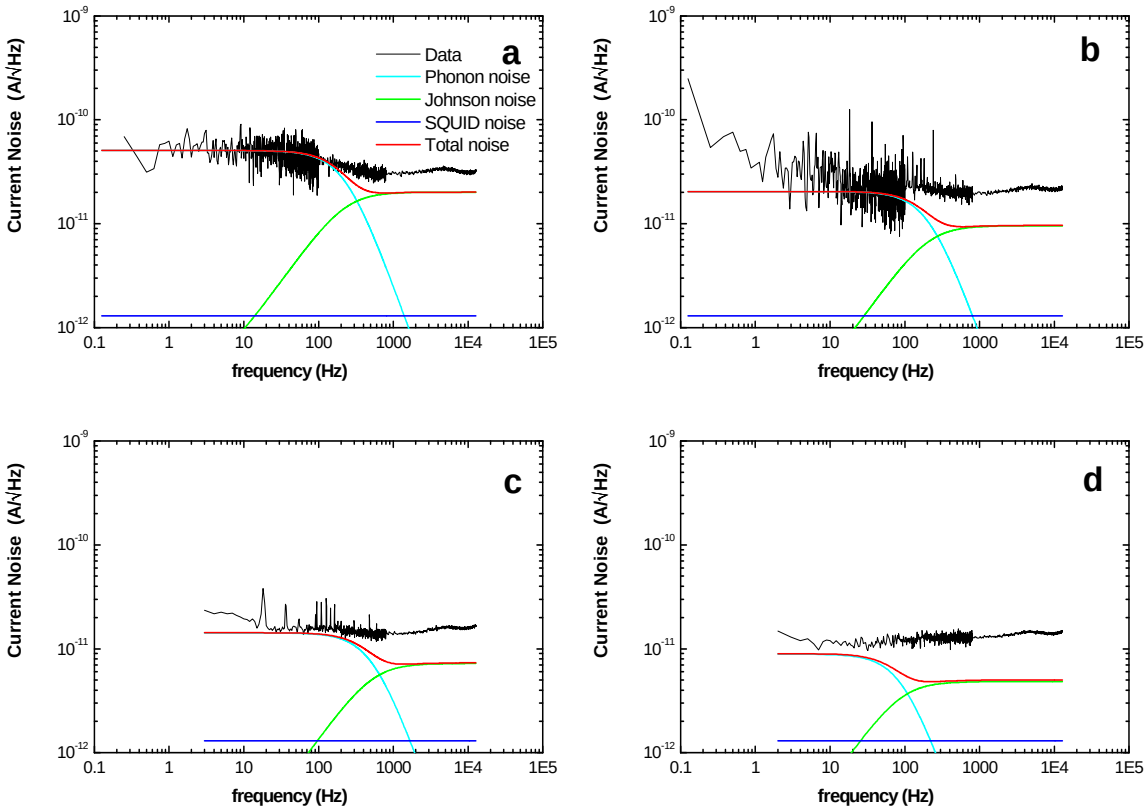


Figure 5.9: Noise from device alpha, a 10-square device with normal state cold resistance of 5 Ω. The separate plots show a) 1% up the transition, b) 3% up the transition, c) 12% up the transition, and d) 25% up the transition. The colored lines show contributions to the expected noise. The turquoise line is phonon noise, the green line is Johnson noise, the blue line is SQUID noise and the red line is the sum in quadrature of all three contributions.

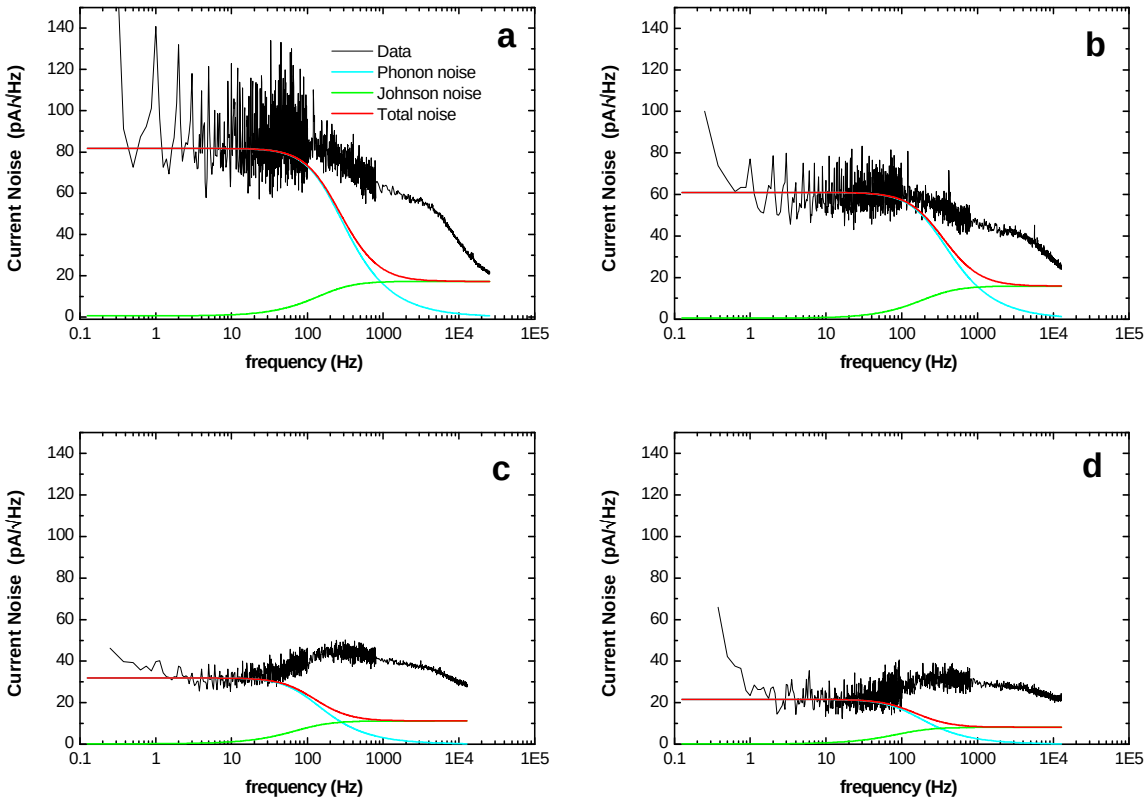


Figure 5.10: Noise from device beta, a 3-square device with a normal state cold resistance of 1.5 Ω. The separate plots show a) 3.5% up the transition, b) 4.4% up the transition, c) 7% up the transition, and d) 10% up the transition. The color scheme is the same as in Figure 5.9, however the SQUID noise is not plotted.

Specifically, there is a large broad bump at high frequencies, most prominent in panels c and d. The excess noise is generally greater in device beta than in device alpha for a given percent through the transition.

Device gamma displayed unusual noise behavior. Noise spectra were taken on several different days. The spectra were inconsistent from one day to the next. They showed different amounts of excess noise and displayed different general shapes in the total noise. The other devices had consistent and similar noise behavior on different days. During the tests of device gamma, there was unusually high activity in the laboratory, both with other experiments and with the facility. We have thus decided to disregard the noise data from device gamma.

Device delta had perhaps the most remarkable noise performance. As seen in Figure 5.11, at the lowest bias voltages, the noise fits the basic theory extremely well. In this

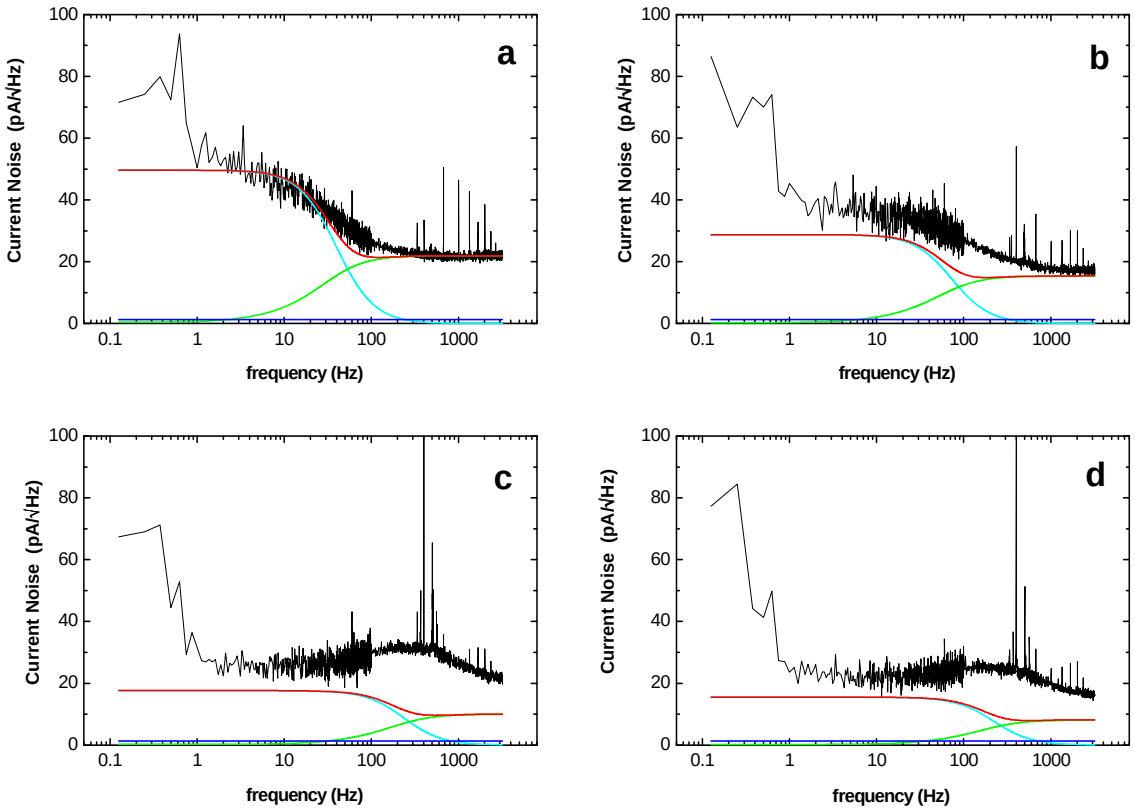


Figure 5.11: Noise from device delta, a 1-square device with a normal state cold resistance of 0.5 Ω. The separate plots show a) 2% up the transition, b) 18% up the transition, c) 43% up the transition, and d) 51% up the transition. The color scheme is the same as in Figure 5.9.

range, the NEP of the device is $2.27\pm0.17\times10^{-17}$ W/$\sqrt{Hz}$. At higher biases, the noise develops an excess noise bump, very similar in appearance to device beta. There is also more low frequency noise at higher bias voltages, causing the data to lie slightly above the basic theory. The apparent very low frequency excess noise below one Hz is most probably due to activity in the laboratory, as described in the introduction to this section, as this data was not taken at night. Note also the 402 Hz pickup. The source of this was never determined.

In analyzing this data, the biggest shortcoming in the analysis is the lack of data at high bias voltages. There were many difficulties in obtaining noise spectra at high bias voltages. In general, in the limited experimental time available we decided to focus on the regime where the noise fit the basic theory and where it began to deviate from it. This happened at the lowest bias voltages. The cryostat had a 6–8 hour hold time, with channels available

for two devices. It would be almost impossible to take a full data set from both devices in this short time. A 'full' data set consists of load curves at different bath temperatures, time constant measurements through the transition, and large frequency range noise spectra through the transition.

When taking noise spectra, we used a load curve taken with the DAC to determine at which bias voltages to take the noise spectra. At high biases, the load curve has a broad minimum. One obstacle to taking spectra in this regime was the difficulty in determining if the device was normal or if it was high in the transition.

The greatest difficulty in obtaining data at high bias points has to do with maintaining the bath temperature. At the top of the transition, the bath temperature would slowly rise. The TES was acting in effect as a resistive heater inside the dewar. Usually the temperature would stabilize after approximately 20 minutes, except at the largest biases. Capturing the noise spectra is a lengthy process, especially for the low frequency scans. The longer the bath temperature was warmed up, the shorter the hold time of the dewar. Taking a careful noise spectra of the device while it is normal can take up to 15 minutes, yet it shortens the hold time of the dewar by roughly 30 minutes. To get the most data out of the short hold time, we usually started at the low biases. More often than not, the dewar would run out of cryogens while taking noise spectra.

It is clear that in the future, we should focus on the entirety of the transition, not just at the lowest biases. To aid in this, it would be advantageous to have a refrigerator with more cooling power. A longer hold time in the cryostat would allow for time to stabilize the bath temperature at the high biases. In addition, extra care must be taken to ensure that data is taken through the entirety of the transition.

### 5.3.2 Extrapolating general noise behavior

In order to get a handle on the general behavior of the excess noise, we need to quantify the excess noise in such a way that we can compare the trends between devices. We also need to quantify the excess noise independent of any excess noise model. The excess noise is given by the quadrature difference between the data and the theory:

$$I^2_{n,excess} = I^2_{n,data} - I^2_{n,theory} \tag{5.2}$$

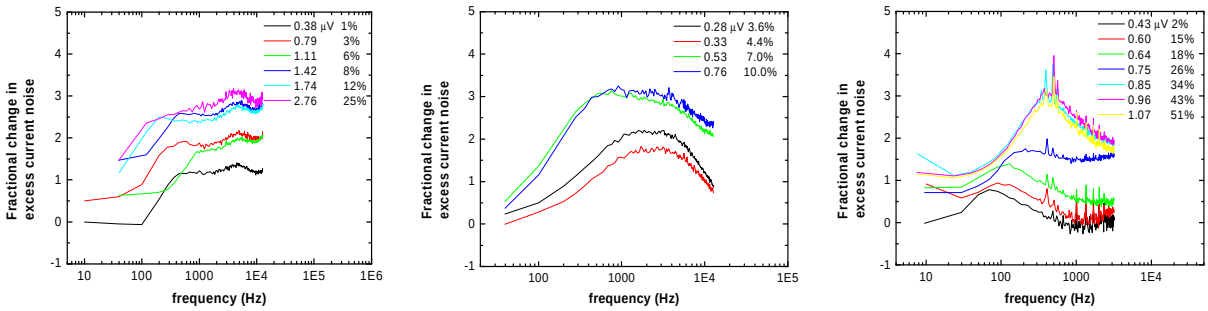


(a) alpha (b) beta (c) delta

Figure 5.12: Fractional excess noise from devices alpha, beta and delta. When the excess noise is equal to the basic theory, the fractional change in the noise is 1, as in equation (5.3). In the legend, each curve is denoted by its bias voltage and the corresponding percent through the transition. For all three devices, the general trend is that the fractional change in excess noise increases with increasing bias voltage.

Therefore, a suitable measure of the excess noise is the fractional change in excess current noise:

$$F_I = \frac{\sqrt{I_{n,data}^2 - I_{n,theory}^2}}{I_{n,theory}} \tag{5.3}$$

When the excess noise is equal to the value predicted by theory, the fractional change will yield a value of one; when it is twice as much the fractional change will yield a value of two, and so on. This is clearly more intuitive than a simple ratio between data and theory. For example, if the excess noise is equal to the value predicted by theory, a simple ratio will yield a value of $\sqrt{2}$. Figure 5.12 shows the fractional change in excess current noise for devices alpha, beta and delta. For clarity, the data has been smoothed by taking frequency bins and plotting the average of the data in the bin. The plot for device alpha uses bins of 100 Hz, the plot for device beta uses bins of 40 Hz, while the plot for device delta uses 25 Hz. The bin size was chosen for clarity without degrading the quality of the data.

All devices show a general trend that the noise increases with bias voltage. However, the details of the shape of the excess noise are quite different. The magnitude of the increase does not scale with bias voltage between devices. Each device shows a peak in the fractional change in the excess noise, but in each device this peak has a different shape and occurs at different frequency.

### 5.3.3 Models for excess noise

Upon inspection, device beta had a considerable amount of residue wrapped around the TES island. Some of this residue on another device can be seen in Figure 3.2 on the TES leads and on the silicon nitride leg on the left of the image. This residue was a pervasive problem as a result of our processing, however most devices only had the residue on the silicon nitride leg. If the residue is in contact with the TES, it will be weakly coupled thermally to the TES itself. This residue has a high heat capacity and can potentially add excess noise to our device. We believe that this is the source of excess noise in device beta, and explains why the noise in this device at the low bias voltages is different from that in devices alpha or delta.

We attempted to fit the noise from the three devices, alpha, beta, and delta to the thermal fluctuation model as given in references [14, 23], meeting with varying degrees of success. Device beta was the only device which had noise that could be mostly modelled by this description, as seen in Figure 5.13. In reference [14], the SRON group was able to model their excess fluctuation noise with only two elements, the TES and the absorber, and a constant thermal link between them. In our fit, we had to vary the strength of this thermal link to get a good fit. This value of the thermal conductance, which we call $G_{excess}$, varied between 1.0 $\mu$W/K for the lowest bias and 35.0 $\mu$W/K for the highest bias, with $G_{excess}$ increasing with increasing bias.

The noise in device alpha could not be fit to the same model. However, device delta could with some exceptions be fit to the thermal fluctuation noise model. This can be seen in Figure 5.14. Again, $G_{excess}$ varied between biases: 0.2 $\mu$W/K for the two lowest biases and 20 $\mu$W/K for the higher biases. To obtain a reasonable fit, however, we had to change the measured time constant of the device. At the lowest bias voltages the time constant stayed the same for the best fit. For the highest bias voltages, the best fit was achieved with a time constant of 2.8 ms, about a factor of 3 longer than that measured with the LED technique, as described in Section 5.2.3. Although this model may not reflect a physical representation of the behavior of the device, the fit does suggest an avenue for a model of the excess noise in this particular device.

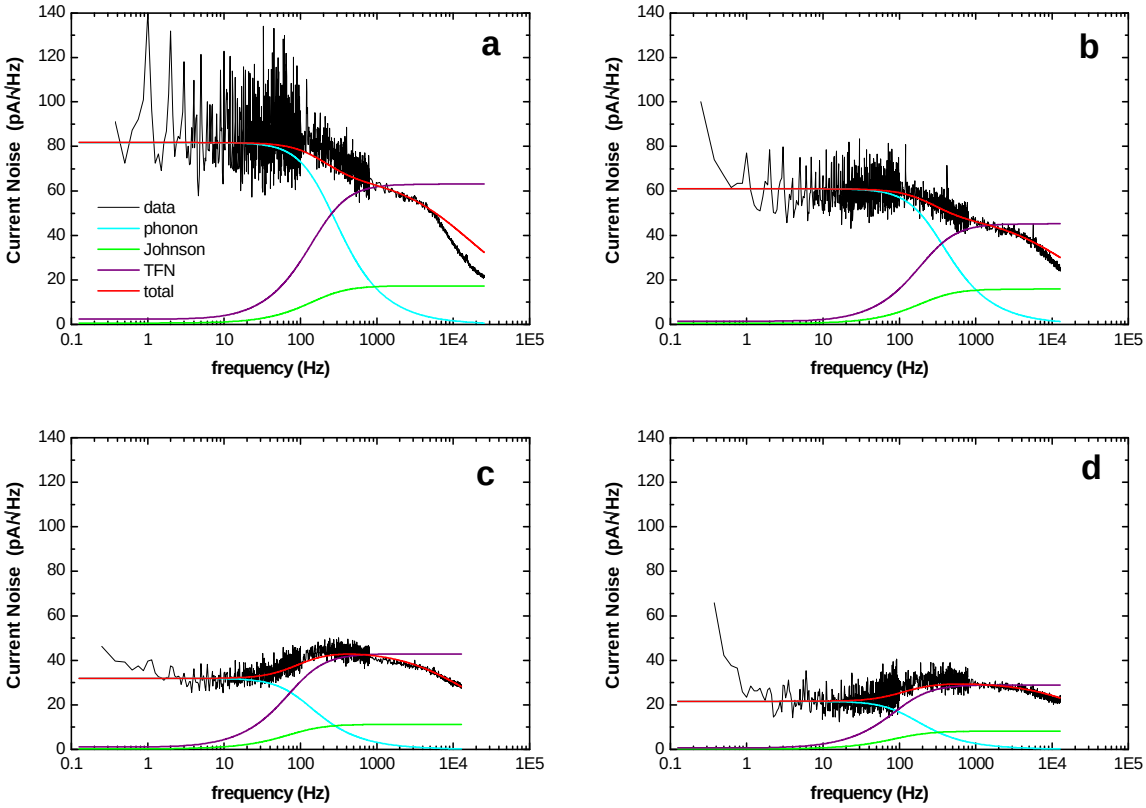


Figure 5.13: Noise from device beta, including the fit to the thermal fluctuation noise model. The separate plots show a) 3.5% up the transition, b) 4.4% up the transition, c) 7% up the transition, and d) 10% up the transition. The color scheme is the same as in Figure 5.9, however the SQUID noise is not plotted, and the thermal fluctuation noise is plotted in purple. The total noise is less than the thermal fluctuation noise at high frequencies due to the rolloff introduced by the inductor in the circuit.

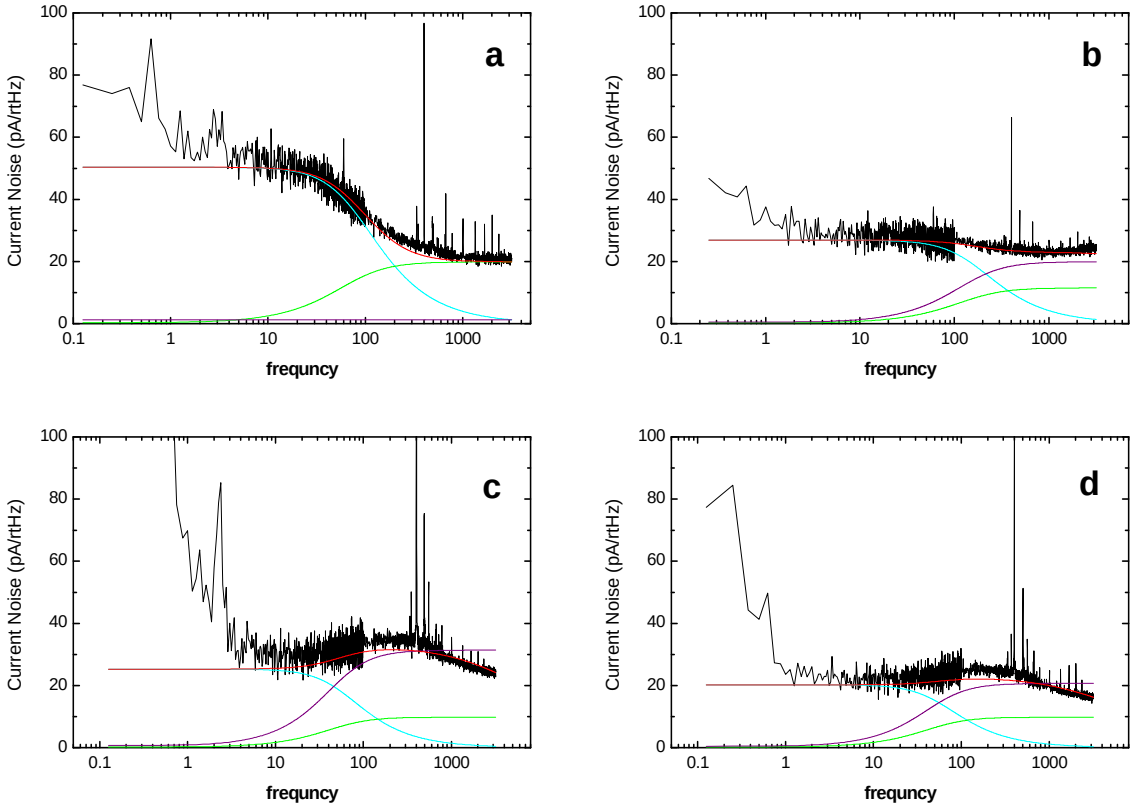


Figure 5.14: Noise from device delta, including the fit to thermal fluctuation noise model. a) 2% up the transition b) 18% up the transition c) 43% up the transition d) 51% up the transition. The color scheme is the same as in Figure 5.9, and the thermal fluctuation noise is plotted in purple.

# Chapter 6

# Complex Impedance Analysis

## 6.1 Introduction to complex impedance analysis

Many groups are working on developing superconducting bolometers for widely varying applications. In several cases TES detectors have proven to give better performance than current technology for a given application. For example, in solid state X-ray emission studies TES detectors yield a great bandwidth improvement over traditional scintillators [29]. TES detectors have the promise of being very sensitive, fast and potentially easy to implement in large arrays. Unfortunately they are not without their own problems. As discussed in Chapter 4, transition edge sensors are almost universally plagued with excess noise at high frequencies. Groups using different TES materials in different geometries see similar excess noise behavior. A greater understanding of a bolometer operating in its superconducting transition will shed more light on the design and successful implementation of this class of detectors.

We need more clues as to the nature of the superconducting state of an operating TES, and one such clue can be provided by heat capacity measurements through the transition around $T_c$. Near $T_c$, a superconductor has a higher heat capacity than in its normal resistive state just above the transition due to an energy gap in the electronic state. There is a discontinuity in the electronic contribution to the heat capacity in the phase transition at the critical temperature, $T_c$ [69]. However, in experiments we measure the total heat capacity, that is the electronic contribution and other contributors, such as a lattice contribution. The shape of the heat capacity transition through the superconducting resistive transition might give us clues to the microscopic behavior of the device in the superconduting/normal mixed state.

In the landmark 1982 paper, J. C. Mather discussed non-equilibrium noise theory for a

general bolometer [57]. In this paper he suggests using complex impedance as a method of measuring the heat capacity of the detector. In this way, complex impedance analysis can provide a powerful tool to aid in our understanding of the physics of TES detectors while in the superconducting resistive transition.

For TES detectors, the only published work on measuring the complex impedance is by M. Lindeman at NASA Goddard Space Flight Center (GSFC) [51]. He studied X-ray calorimeters that consisted of a Mo/Au TES. The X-ray TES detectors at GSFC consistently showed excess noise [52], so they chose to study some of the underlying physics of the noise. They speculate that if the TES film transitions from the superconducting state to the normal state smoothly, the heat capacity profile would also transition smoothly. However, if the TES transitions in some 'chunky' manner, that is with isolated islands of normal state and superconducting state, then the heat capacity profile might have discrete steps. They find that the heat capacity in their Mo/Au films transition in the latter fashion, lending support to the 'chunky' transition hypothesis. One key difference between the TES films studied at GSFC and those discussed in this thesis is that the GSFC films have relatively low impedance, around 10 m$\Omega$ when normal.

Since the work at GSFC was only performed on one device of relatively low impedance, there is considerable work to be done in understanding more about the heat capacity of a TES while biased in the transition. In this chapter we will develop a mathematical expression for the complex impedance of a TES. We will then explain how complex impedance measurements are obtained experimentally. Experimental data on the complex impedance of the TES devices in this thesis are described. Finally we discuss how future measurements can be performed to provide more accurate measurements of the heat capacity.

## 6.2 Deriving the complex impedance of a voltage-biased TES

To derive an expression for the impedance of a TES, we start by setting up the power balance equation, as in equation (4.7) for the TES with no optical power. The electrical power dissipated is balanced by the thermal power lost through conduction to the bath and the power lost due to a temperature change in the TES. C is the heat capacity and does

not change with time, so

$$\frac{V_b^2}{R_{TES}} = G\left(T_{TES} - T_{bath}\right) + C\frac{\mathrm{d}}{\mathrm{d}t}T_{TES} \tag{6.1}$$

We want to apply a perturbation to the system and look at the system's response. Ultimately we are looking for the impedance, which is $Z_{TES} = \frac{\mathrm{d}V}{\mathrm{d}I}$. We apply perturbations in a linear approximation of the form:

$$\begin{aligned} V_b &= V_{b0} + \delta V_b \mathrm{e}^{\mathrm{i}\omega \mathrm{t}} \\ R &= R_0 + \delta R \mathrm{e}^{\mathrm{i}\omega \mathrm{t}} \\ T_{TES} &= T_{TES0} + \delta T_{TES} \mathrm{e}^{\mathrm{i}\omega \mathrm{t}} \end{aligned} \tag{6.2}$$

We insert the perturbations of equation (6.2) into equation (6.1), and expand the denominator on the left hand side in a Taylor series. Keeping only the first-order terms:

$$\begin{aligned} \frac{V_{b0}^2}{R_0} &- \frac{V_{b0}^2}{R_0}\frac{\delta R}{R_0}\mathrm{e}^{\mathrm{i}\omega \mathrm{t}} + \frac{2V_{b0}}{R_0}\delta V_b \mathrm{e}^{\mathrm{i}\omega \mathrm{t}} \\ &= G\left(T_{TES0} + \delta T_{TES}\mathrm{e}^{\mathrm{i}\omega \mathrm{t}} - T_{bath}\right) + i\omega C \delta T_{TES}\mathrm{e}^{\mathrm{i}\omega \mathrm{t}} \end{aligned} \tag{6.3}$$

The zero-order term is $\frac{V_{b0}^2}{R_0} = G\left(T_{TES0} - T_{bath}\right)$. We subtract this from equation (6.3) because we only want to look at the perturbations. We can divide through by $\mathrm{e}^{\mathrm{i}\omega \mathrm{t}}$ to obtain:

$$\frac{2V_{b0}}{R_0}\delta V_b - \frac{V_{b0}^2}{R_0^2}\delta R = G\delta T_{TES} + i\omega C \delta T_{TES} \tag{6.4}$$

This equation describes the perturbations of the TES around equilibrium, where $R_0$ is the equilibrium resistance of the TES; $V_{b0}$ is the voltage of the TES; $T_{TES}$ is the temperature of the TES at the given bias point. We will remove the subscripts for ease of notation:

$$\frac{2V}{R}\delta V - \frac{V^2}{R^2}\delta R = G\delta T + i\omega C \delta T \tag{6.5}$$

Since the complex impedance is given by $Z = \frac{\mathrm{d}V}{\mathrm{d}I}$, we eliminate all the $\delta T_{TES}$ and $\delta R$ terms, by writing them in terms of $\delta I$ and $\delta V$. We can achieve this by using the relations:

$$\delta R = \frac{\partial R}{\partial T}\delta T + \frac{\partial R}{\partial I}\delta I \tag{6.6}$$

and,

$$\begin{aligned} I &= \frac{V}{R} \\ \Rightarrow \delta I &= \frac{\delta V}{R} - \frac{V}{R^2}\delta R \end{aligned} \tag{6.7}$$

Combining (6.6) and (6.7) and solving for $\delta T$:

$$\frac{\partial R}{\partial T}\delta T = \left(\frac{\delta V}{R} - \delta I\right)\frac{R^2}{V} - \frac{\partial R}{\partial I}\delta I \tag{6.8}$$

We substitute equation (6.8) and equation (6.6) into equation (6.5), and use the definitions:

$$\begin{aligned} \alpha &= \frac{T}{R}\frac{\partial R}{\partial T} \\ \beta &= \frac{I}{R}\frac{\partial R}{\partial I} \end{aligned} \tag{6.9}$$

We find,

$$Z_{TES}(\omega) = R\left[(1+\beta) + \frac{(2+\beta)}{2}\frac{I^2R}{CT}\alpha\tau\left(-1 + \frac{1+i\omega\tau}{-1+i\omega\tau}\right)\right] \tag{6.10}$$

where,

$$\tau = \left[\frac{I^2R\alpha}{CT} - \frac{G}{C}\right]^{-1} \tag{6.11}$$

We can express the complex impedance in equation (6.10) in terms of the loop gain, $\mathscr{L}$, analogous to electronic feedback circuits defined in equation (4.19):

$$\mathscr{L} = \frac{\alpha P}{GT} \tag{6.12}$$

Using $\tau_{therm} = C/G$, the complex impedance is

$$Z_{TES} = R\left[(1+\beta) + \frac{(2+\beta)\,\mathscr{L}}{-\mathscr{L} + 1 + i\omega\tau_{therm}}\right] \tag{6.13}$$

## 6.3 Plotting and fitting complex impedance

In practice, the TES does not stand alone but is part of a circuit as shown in Figure 3.5. In Section 6.2, we derived the expression of the complex impedance of the TES alone, as

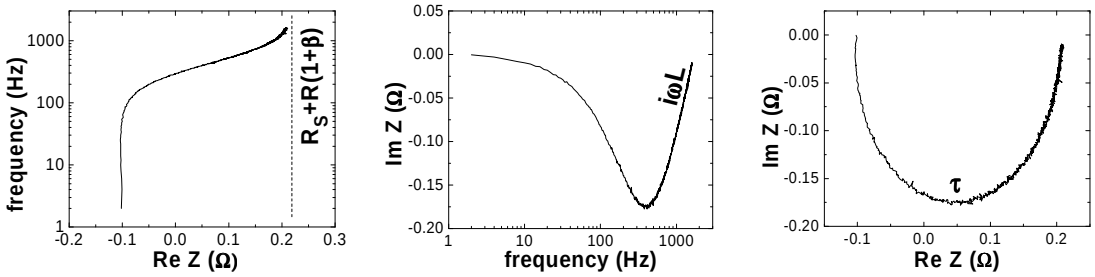


(a) (b) (c)

Figure 6.1: Example of complex impedance curves in the (a) real, (b) imaginary, and (c) complex planes.

given by equation (6.10). The total impedance must include the shunt resistor, $R_S$, and the SQUID-coupling inductor, $L$

$$Z_{TOT} = R_S + i\omega L + Z_{TES} \tag{6.14}$$

To measure the complex impedance, we apply a small chirp signal to the DC bias and look at the differential spectrum output. We feed the chirp signal alone, and the response from the circuit into two channels of a spectrum analyzer. We look at the signal of $\frac{<FFT_{chirp}>}{<FFT_{response}>}$, and obtain the total impedance of the system from:

$$Z_{TOT} = V_{appl}\frac{R_S}{R_b}\cdot\frac{< FFT_{chirp} >}{< FFT_{response} >} \tag{6.15}$$

Figure (6.1) shows representative, yet real, data for the complex impedance expression in equation (6.15). The real part of the complex impedance is plotted in Figure (6.1.a). Note that at high frequencies, the curve approaches $R_s + R(1+\beta)$. The imaginary part of the complex impedance is plotted in Figure (6.1.b). At high frequencies the curve approaches $i\omega L$. Figure Figure (6.1.c) shows the combination of (a) and (b), the real and imaginary parts, in the complex plane. This is a semicircle, with the value of the minimum yielding $\tau$ from the frequency at this point; $\tau = 1/2\pi f$.

The main difficulty with interpreting this measurement is breaking the degeneracy between $\alpha$ and $C$. In equation (6.10), $\alpha$ and $C$ are perfectly degenerate appearing only in a ratio $\alpha/C$. The expression for the time constant in equation (6.11) breaks this degeneracy,

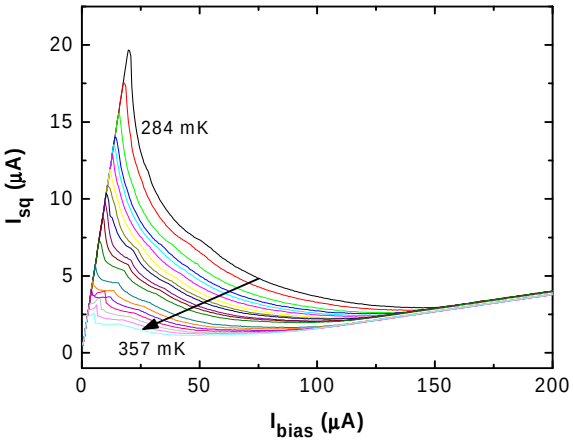


Figure 6.2: Set of bias curves at different temperatures. The coldest temperature plotted is 311 mK, while the warmest temperature plotted is 368 mK. In order to stay in the same point in the transition as the bath temperature warms up, the bias current decreases as shown by the arrow.

provided that the first term, $I^2R\alpha/CT$, is not too large. In a typical measurement scenario, we are at the base temperature of the dewar, which causes the current for a given point in the transition, $I_0$, to be large, and the first term dominates. To stay at a given point in the transition but reduce the current needed to be at that point, we need to increase the bath temperature of the system. Figure (6.2) shows a set of bias curves at different bath temperatures, and an arrow illustrates how $I_0$ decreases with increasing bath temperature for a given point on the transition. Note also that the bias curves tend to develop unusual features as the bath temperature gets closer to the transition temperature. These features are repeatable between different load curves, and also between different cool-downs of the same device. The cause of these features is not yet understood.

In an attempt to break the degeneracy, we warmed up the bath to 353.6 mK, just 16.4 mK below the superconducting transition of the device. We took a set of twelve complex impedance curves through the transition, and curves when the device was superconducting and when it was normal, as shown in Figure (6.3). We would like to fit each curve to equation (6.10) to extract the heat capacity. The next section discusses the issue of this fit in terms of the degeneracy between $C$ and $\alpha$.

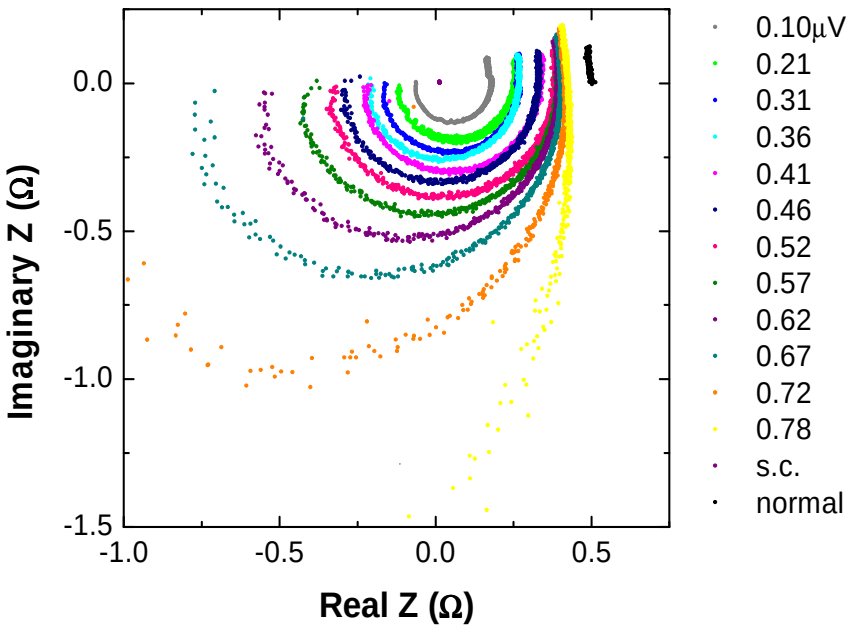


Figure 6.3: Set of complex impedance curves taken at a bath temperature 16.4 mK below the superconducting transition of device delta. The black straight line on the right represents the impedance when the device is normal at a resistance of 0.5 Ω, while the small purple line at a real impedance of zero is taken when the device is superconducting.

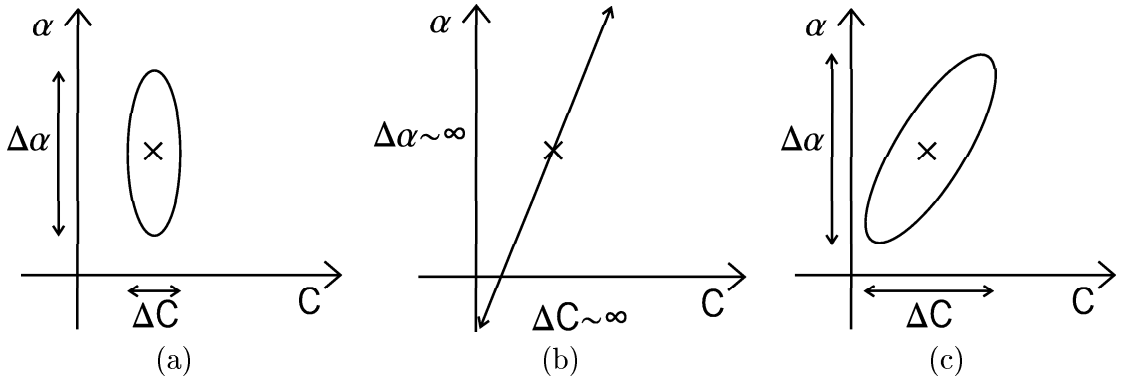


Figure 6.4: $\chi^2$ surface for the pair of variables $\alpha$ and $C$ where they are (a) non-degenerate, (b) perfectly degenerate, and (c) partially degenerate. The 'x' denotes the minimum $\chi^2$, and a contour is drawn in containing all points within $\Delta\chi^2$ of the minimum. The errors in $\alpha$ and $C$ are approximately the extent of this ellipse in either direction. In (a), $\alpha$ and $C$ are perfectly non-degenerate: the ellipse is squared off, and $\Delta\alpha$ and $\Delta C$ are at a minimum. In (b), $\alpha$ and $C$ are perfectly degenerate: the ellipse is tilted and stretched out to form a line. $\Delta\alpha$ and $\Delta C$ are infinite. In the mixed case (c), $\alpha$ and $C$ are partially degenerate: the ellipse is tilted and elongated.

## 6.4 Degeneracy

In order to break the degeneracy, we need to reduce the current in the transition. If we increase the bath temperature, we decrease the current needed to be at a particular point on the transition. This helps to break the degeneracy between $\alpha$ and $C$. We would like to be able to quantitatively calculate how well the degeneracy will be broken for a given device and bath temperature. We would also like to calculate how low $I_0$ must be to break the degeneracy sufficiently.

In order to understand how to break the degeneracy, we need to understand the $\chi^2$ landscape of these two parameters. Calculating $\chi^2$ allows us to test the statistical independence of two or more variables, in our case $\alpha$ and $C$.

$$\chi^2 = \sum_{i=1}^{N} \frac{(f_i - d_i)^2}{\sigma_i^2} \tag{6.16}$$

where $f_i$ is the fitting function, equation (6.10), and $d_i$ is the data value.

Figure (6.4) is meant to illustrate our method of minimizing the degeneracy between these parameters. The three panels a, b, and c, show the $\chi^2$ surface for the pair of variables $\alpha$ and $C$ where they are non-degenerate, perfectly degenerate, and partially degenerate respectively. The 'x' denotes the minimum $\chi^2$, and a contour is drawn containing all points

within $\Delta\chi^2$ of this minimum. If $\Delta\chi^2$ is chosen appropriately, then the errors in $\alpha$ and $C$ correspond to the extent of this ellipse in each direction. In Figure (6.4.a), $\alpha$ and $C$ are perfectly non-degenerate: the ellipse is squared off, and $\Delta\alpha$ and $\Delta C$ are at a minimum. In Figure (6.4.b), $\alpha$ and $C$ are perfectly degenerate: the ellipse is tilted and stretched out forming a line, and the errors are then infinite. In the mixed case, Figure (6.4.c), $\alpha$ and $C$ are partially degenerate: the ellipse is tilted and elongated.

If $C$ changes by $\Delta C$ and $\alpha$ changes by $\Delta\alpha$, then $\chi^2$ changes by $\Delta\chi^2$, where

$$\Delta\chi^2 = \sum_{i=1}^{N} \left[ \frac{\left(f_i + \frac{\partial f_i}{\partial C}\Delta C + \frac{\partial f_i}{\partial \alpha}\Delta\alpha - d_i\right)^2}{\sigma^2} - \frac{(f_i - d_i)^2}{\sigma^2} \right] \tag{6.17}$$

This is the extent of our elliptical contour. Assume that the error $\sigma$ is the same for each data point, so we can move the $\sigma^2$ terms outside the sum. Expanding this expression and regrouping terms:

$$\begin{aligned} \Delta\chi^2\sigma^2 \quad &= \quad \sum_{i=1}^{N} \left[ (f_i - d_i) \frac{\partial f_i}{\partial C}\Delta C + (f_i - d_i) \frac{\partial f_i}{\partial \alpha}\Delta\alpha \right. \\ &+ \quad \left. \left(\frac{\partial f_i}{\partial C}\right)^2 \Delta C^2 + \left(\frac{\partial f_i}{\partial \alpha}\right)^2 \Delta\alpha^2 + 2\left(\frac{\partial f_i}{\partial C}\frac{\partial f_i}{\partial \alpha}\right)\Delta C\Delta\alpha \right] \end{aligned} \tag{6.18}$$

The first two terms in the sum average to 0 since $(f_i - d_i)$ is random about 0, assuming our model provides a good fit to the data.

We can substitute into equation (6.18):

$$\begin{aligned} a &= \sum_{i=1}^{N} \left(\frac{\partial f_i}{\partial C}\right)^2 \\ b &= \sum_{i=1}^{N} \left(\frac{\partial f_i}{\partial \alpha}\right)^2 \\ c &= \sum_{i=1}^{N} \left(\frac{\partial f_i}{\partial C}\frac{\partial f_i}{\partial \alpha}\right) \end{aligned} \tag{6.19}$$

giving

$$\Delta\chi^2\sigma^2 = a\Delta C^2 + b\Delta\alpha^2 + 2c\Delta C\Delta\alpha \tag{6.20}$$

Now we can solve for $\Delta\alpha$ and $\Delta C$ in terms of $a$, $b$, $c$, and $\Delta\chi^2\sigma^2$:

$$\Delta\alpha = -\frac{c}{b}\Delta C \pm \left(\frac{c^2}{b^2}\Delta C^2 - \frac{a}{b}\Delta C^2 + \frac{\Delta\chi^2\sigma^2}{b}\right)^{\frac{1}{2}} \tag{6.21}$$

We want to find the extrema of the ellipse, or where $\Delta\alpha$ is single-valued. This only happens when

$$\frac{c^2}{b^2}\Delta C^2 - \frac{a}{b}\Delta C^2 + \frac{\Delta\chi^2\sigma^2}{b} = 0 \tag{6.22}$$

$$\Delta C^2 = \frac{b\Delta\chi^2\sigma^2}{ab - c^2} \tag{6.23}$$

We can follow the same procedure to obtain

$$\Delta\alpha^2 = \frac{a\Delta\chi^2\sigma^2}{ab - c^2} \tag{6.24}$$

The ellipse is 'squared' when $\Delta C$ and $\Delta\alpha$ are minimized, or when $c^2 \ll ab$.

We can easily calculate $c$, $a$, $b$, and $\chi^2$ from our complex impedance $Z_{TES}$ in equation (6.10). Consider the case similar to our experimental data, where the warmed bath temperature is $T = 353.6$ mK, and at a bias point of 50% up the transition, or $R = 0.25\ \Omega$ and $I_0 = 15.5\ \mu$A. In this case, $c^2/ab = 0.9996$, which means that $C$ and $\alpha$ are almost perfectly degenerate. We calculated the ratio for this detector scenario through the entire transition, and found the ratio to be very close to unity. Unfortunately, for our device it is not possible to sufficiently break the degeneracy between $C$ and $\alpha$ to get a good measure of the heat capacity in the transition.

To break the degeneracy, we need to lower $I^2R\alpha/CT$ so that it is approximately equal to $G/C$. The most obvious way to achieve this is to reduce $I^2R$ in the device. This might explain why GSFC was able to easily measure the complex impedance in their TES device, while we cannot. Their device had a normal state impedance of 0.02 $\Omega$, while our impedance was 0.5 $\Omega$. The choices for the impedances of our devices in this thesis were somewhat arbitrary.

We have demonstrated that measuring the complex impedance of the device is straightforward. However, interpreting the results in the framework presented is both subtle and complex. We can take the results of our measurements, and look at their shortcomings to suggest specific experiments for the future. The bath temperature could be better controlled

in order to bring the bath temperature very close to the transition temperature. Our warm bath temperature was still 16.4 mK from the transition temperature of the device. Other experiments at Caltech/JPL have shown temperature regulation down to fluctuations of 0.1 mK. We can also produce devices with much lower normal state impedance. It would also be very useful to develop a model from empirical data and using the framework presented in this section. This model could predict the ability to break the degeneracy in the parameters for a wide variety of devices. In order for this model to work, we need more empirical data to show how both the impedance and bath temperature change the shape of the load curve.

# Chapter 7

# Conclusion

The SAMBA architecture has been devised as a next-generation solution to future CMB missions. SAMBA is designed to be a large format array of antenna-coupled bolometers. The antennas are polarization sensitive, and have a large bandwidth. This will enable the construction of an array that has many pixels filling the entire focal plane, each with several wavelength channels with use of microstrip filters. The SAMBA design addresses the need for more sensitivity and throughput in future CMB experiments.

As a precursor to the complete SAMBA architecture, we have designed, developed and studied a single-element device, which is presented in this thesis. This device consisted of a dual-slot microstrip-coupled antenna coupled to an Al/Ti/Au TES on a thermally isolated island. Several obstacles in processing these devices were overcome, resulting in a small pool of test detectors. These obstacles included designing a new lithography process for the many-layered device, maintaining the integrity of the TES through processing, and designing a reliable microstrip termination structure for the normal metal resistor.

We tested four detectors under minimized optical loading conditions, commonly referred to as 'dark testing.' We found that the transition temperature of the TES decreased slightly after processing the entire device. A measure of the steepness of the transition, $\alpha$, was found to be $\sim$100 in the middle of the transition. This is lower than has been measured in other TES films. This might be due to poor edge definition of the TES. We patterned the TES in a liftoff process, which leads to jagged edges. In the future it would be good to use an etch-back technique to obtain sharply defined edges of the TES. We measured load curves and found the thermal conductance of the detector, $G$, to be 55 pW/K to within 6% for all four devices. We measured the effective time constant of the devices by using an LED to apply a pulse of radiation directly to the TES island. We find that the time constants are smallest in the middle of the transition where the electrothermal feedback is the strongest. The

fastest time constant measured was 437 $\mu$s. Finally, we used the normal metal microstrip termination resistor as an on-island heater. We found that the current responsivity of our device is linear to 2%.

The most remarkable feature of our TES devices is their very small excess noise. Noise so close to the theoretical limit has almost never been seen in TES detectors. We attribute this to the reduced heat capacity of the TES film and absorber in our devices. However, the increased excess noise at high bias voltages is not fully understood. More work must be done to understand this excess noise if the device is to be operated in this regime.

In an effort to expand our understanding of the physics in the superconducting transition, we made the first measurements of the complex impedance in an Al/Ti/Au device. This is only the second published work on this topic. Unfortunately, we were not able to extract the heat capacity of the device through the transition, because the heat capacity and $\alpha$ are degenerate for our detectors. However, we do believe that these measurements can be successful on lower impedance devices if we design an efficient temperature control system.

We have developed TES detectors with low noise. We believe they can be engineered to have even lower noise, by decreasing G and C. We can also take care to make sure each device is clean from residue and particles. These detectors are prime candidates for future CMB missions.

Finally, the work in this thesis suggests many promising avenues for future research. Future experiments could be devised to aid in the understanding of the topic. In the case of TES detectors, the physics of the superconducting film in its transition while biased on a thermally isolated island is perhaps more complicated than we initially expected. TES development is usually conducted with the goal of developing a working instrument. Rarely is there time or money to study just the TES film itself. With the widespread difficulties in these films, it seems clear that more fundamental work must be undertaken before TES detectors can be reliably engineered for implementation in the variety of applications proposed. It seems that some of the phase-space of the parameters of the detectors must be explored. For example, one could make 'bare' TES films on a thermally isolated island with no absorber. The size of the films could also be varied, providing information which could shed light on the extended heat capacity model for larger TES films. It could also shed light on some of the characteristics of the superconducting transition, especially if complex

impedance measurements are successful. As another example, one could design detectors with the same small TES geometry, but using the different TES materials in use by various groups. In the literature it is difficult to compare TES films based on the materials properties alone because their geometries, resistances and lead materials are different. Producing a homogeneous set of detectors would resolve this problem.

Clearly more work is needed before TES detectors are a mature technology, capable of being implemented in the same way as detectors in other wavelength regimes. However, TES technology has much promise as a solution to detector needs in the astronomical and solid state communities.

# Appendix A

# Photoessay

For most experimental scientists working in the CMB field, the details of the processes involved in fabricating a detector are mystifying. Often, the devices are made by a group of skilled technicians in a cleanroom then handed over to the observers who integrate them into instruments. As a scientist who stands on both sides of the line, I would like to show pictorially the major steps in the fabrication process of a typical bolometer, and hopefully shed some light on the workings of the cleanroom.


Figure A.1: When entering the cleanroom, an airshower greets you to blow off particles.

Figure A.2: Although you might be working in the class 1000 area, it is mandatory to satisfy class 10 gowning requirements since all areas are interconnected. Most of the gear we don is not to protect us from the chemicals we will use, but to protect our devices from us! Particulates can ruin a delicate device and make it difficult to work with.

Figure A.3: The next few figures will show an example of a process layer. Here is an electron-beam evaporator, which can deposit various materials with relatively low impurity rates. In an etch-back process, the layer (such as gold) will first be evaporated at the appropriate thickness onto a silicon wafer.

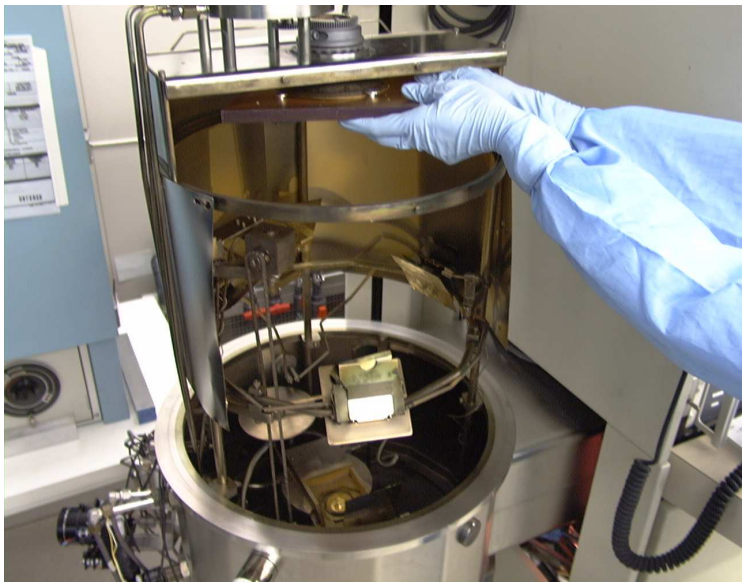

Figure A.4: This is the inside of the same e-beam evaporator. I am holding the plate on which the wafer is mounted, inverted facing down. At the bottom of the picture, the gold crucible can be seen.

Figure A.5: Other materials, such as niobium, can be deposited in this sputtering system.

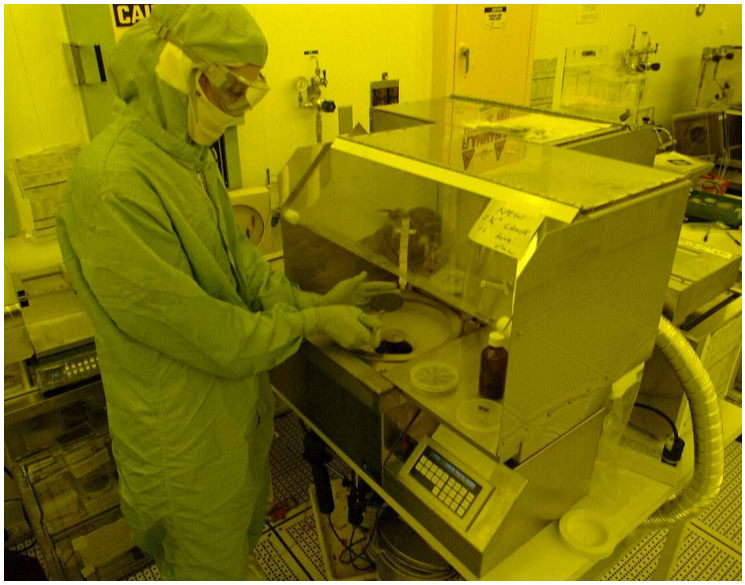

Figure A.6: After the metallization layer is deposited, a layer of photo resist is spun evenly on the surface. No, my camera wasn't broken. Photoresist is a liquid polymer solution that reacts when exposed to UV radiation. When using resist, we have to work in a 'UV-tight' environment, causing the room to look yellow. For a 'positive' resist process, the exposed polymers break under UV radiation. This reaction is used to create the desired pattern on the wafer.

Figure A.7: A mask is used to create the desired pattern. The mask and wafer are placed in an aligner system. Once the proper placement is achieved, the wafer is exposed with the proper wavelength radiation for a set amount of time.

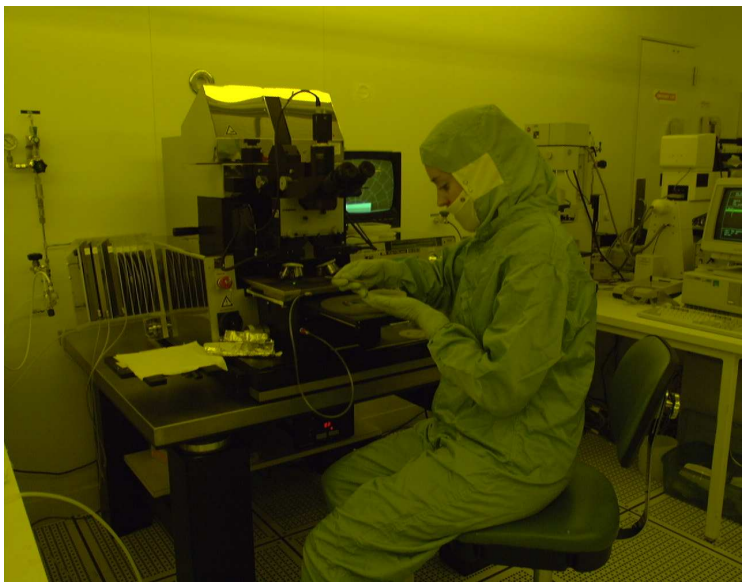

Figure A.8: The wafer is unloaded from the aligner and...

Figure A.9: ...the wafer is placed in a developer for a precise amount of time. In our 'positive' resist example, the developer washes away the broken polymer areas, leaving the pattern behind.

Figure A.10: The wafer has to be carefully dried before continuing the process. After this, the materials in the exposed areas are removed either in a wet etch or in a plasma etch, leaving behind a pattern under the photoresist. Finally the photoresist is removed in a solvent.

Figure A.11: For detectors with neutron transmutation doped germanium thermistors, the chips must be placed and bonded by hand. It can be a very time-consuming and tedious process.

Figure A.12: The whole device must be protected before etching out the 'window' of silicon that defines the open area under the silicon nitride membrane. Here I am melting wax on the top side of the device.


Figure A.13: Safety first! This is the personal protective equipment donned when handling acids. Besides the goggles, a faceshield, apron, and acid resistant gloves complete the ensemble.


Figure A.14: The silicon window is etched from the backside either in a dry plasma etch process, or as shown here with hydrofluoric acid and nitric acid. After this step, the wax is dissolved in solvents and the delicate device is removed from the liquid, taking care not to break the membrane.

# Appendix B

# Process Sheets

As requested by my thesis committee, these are the actual process sheets I developed and used in fabricating the devices described in this thesis. The fabrication was performed exclusively at the Microdevices Laboratory at NASA's Jet Propulsion Laboratory in Pasadena, California. These recipes are not meant to be 'rules' in recreating similar devices, but rather guidelines for a starting point in developing a similar recipe. In general recipes vary from cleanroom to cleanroom, and even machine to machine within a laboratory.

1. **Ti/Au/Ti normal metal boundaries/load resistor**
   Thin normal metal layer will be placed on first to go underneath TES structure. Top layer of Ti is to prevent diffusion of Au of this layer into the Al layer of TES.

*Preparation:*

| |
|---|
| • Clean wafer by rinsing in ACE followed by IPA for 1 m each, blow dry. |
| • Dehydrate wafer by placing on 115°C hot plate for 2 m, Cool wafer on plate for ∼1 m. |
| • Perform $O_2$ dry etch for 1 m using 100W, 50 sccm at 100 mT to clean wafer. |
| • Place **HMDS** on front side of wafer let sit for 30 sec |
| • Spread at 750 rpm for 3 sec and spin at 400 rpm for 40 seconds. |
| • Place **AZ 5214E** on front side of wafer |
| • Spread at 750 rpm for 3 sec and spin **AZ 5214E** at 4000 rpm for 40 seconds. |
| • Let PR settle 5 min |
| • Softbake at **95°C for 95 sec** |

*Patterning:*

| **Machine** | **MJB3** | **MA6** |
|---|---|---|
| **Mode** | **High precision (vac chamber)** | **Hard vac** |
| **Exposure** | **20sec at 10mW/cm$^2$, I=320nm** | **5 sec at 25mW/cm$^2$** |
| **Develop** | **4:1(DI:AZ400k) for 25-35sec** | **4:1(DI:AZ400k) for 25-35sec** |

| |
|---|
| • Inspect pattern under microscope. Proceed if all lines are well defined. |
| • **CD 2$\mu$m** onto M10 TES boundary, **8$\mu$m** on ALL load resistor |
| • Otherwise, strip photoresist and repeat step. |
| • Plasma ash in O2 at .5Torr, 100W, 2min |
| • Dip in diluted HF (10:1), or BOE for 5 sec then rinse in DI and blow dry. |

*Metallization:*

| |
|---|
| • Evaporate using the Sloan or TSC e-beam evaporator at a base pressure of $\leq 5 \times 10^{-7}$ Torr |
| **25Å of Ti at 1Å/ sec** |
| **120Å of Au at 2Å/ sec** |
| **50Å of Ti at 1Å/ sec** |
| • Dip wafer in room temp ACETONE and heat to 50°C (water bath) for **30-60min**. |
| • Perform DI flow rinse to remove microstrip and residual metals. |
| • Observe under microscope to ensure all lines have metal |
| • If metal was removed, strip metal and repeat evaporation |
| • **CD 2$\mu$m** onto M10 TES boundary, **8$\mu$m** on ALL load resistor |

**2. TES patterning by liftoff**

Al/Ti/Au TES, where Ti is diffusion barrier between Al and Au.
Top Ti structure is sticking layer for dielectric, which will be placed on top.

*Preparation:*

| |
|---|
| • Clean wafer by rinsing in ACE followed by IPA for 1 m each, blow dry. |
| • Dehydrate wafer by placing on 115°C hot plate for 2 m, Cool wafer on plate for ∼1 m. |
| • Perform $O_2$ dry etch for 1 m using 100W, 50 sccm at 100 mT to clean wafer. |
| • Place **HMDS** on front side of wafer let sit for 30 sec |
| • Spread at 750 rpm for 3 sec and spin at 400 rpm for 40 seconds. |
| • Place **AZ 5214E** on front side of wafer |
| • Spread at 750 rpm for 3 sec and spin **AZ 5214E** at 4000 rpm for 40 seconds. |
| • Let PR settle 5 min |
| • Softbake at **95°C for 95 sec** |

*Patterning:*

| **Machine** | **MJB3** | **MA6** |
|---|---|---|
| **Mode** | **High precision (vac chamber)** | **Hard vac** |
| **Exposure** | **20sec at 10mW/cm$^2$, I=320nm** | **5 sec at 25mW/cm$^2$** |
| **Develop** | **4:1(DI:AZ400k) for 25-35sec** | **4:1(DI:AZ400k) for 25-35sec** |

| |
|---|
| • Inspect pattern under microscope. Proceed if all lines are well defined. Otherwise, strip photoresist and repeat step. |
| • **CD 10$\mu$m** on M10 or X10 type. |
| • Plasma ash in O2 at .5Torr, 100W, 2min |
| • Dip in diluted HF (10:1), or BOE for 5 sec then rinse in DI and blow dry. |

*Metallization:*

| |
|---|
| • Evaporate using the Edwards e-beam evaporator at a base pressure of $\leq 5 \times 10^{-8}$ Torr |
| **280Å of Al at 2Å/ sec** |
| **280Å of Ti at 2Å/ sec** |
| **280Å of Au at 2Å/ sec** |
| **50Å of Ti at 1Å/ sec** |
| • Dip wafer in room temp ACETONE and heat to 50°C (water bath) for **30-60min**. |
| • Slight agitation may be needed to have film lift off completely. |
| • Perform IPA dip/flow rinse to remove ACE and residual metals. |
| • Observe under microscope to ensure all lines have metal. |
| • **CD 10$\mu$m** on M10 or X10 type. |
| • If NOT well patterned, strip metal and repeat evaporation. |

**3. Nb Ground plane by liftoff**

A good undercut is needed for this layer due to the fact that Nb is sputtered onto the wafer, and a liftoff process is used.

We use a bi-layer process of PMMA (as it's removed with chlorobenzene) and PR.

Care must also be taken to not expose the underlying TES layer to 400K developer, as the Al will be stripped.

*Preparation:*

| |
|---|
| • Clean wafer by rinsing in ACE followed by IPA for 1 m each, blow dry. |
| • Dehydrate wafer by placing on 115°C hot plate for 2 m, Cool wafer on plate for ∼1 m. |
| • Place **HMDS** on front side of wafer let sit for 30 sec using small spinner |
| • Spread at 750 rpm for 3 sec and spin at 400 rpm for 40 seconds. |
| • Place **6% 495K PMMA** on front side of wafer using small spinner. |
| • Spread at 750 rpm for 3 sec and spin **6% 495K PMMA** at 4000 rpm for 40 seconds. |
| • Softbake at **95°C for 65 sec** followed by **105°C for 5 min.** |
| • Spread **AZ5214E** at 750 rpm for 3 sec and spin at 4000 rpm for 40 sec. |
| • let PR settle 5 min. |
| • Softbake at **95°C for 95 sec** |

*Patterning:* REGULAR 5124E DEVELOPMENT

| **Machine** | **MJB3** | **MA6** |
|---|---|---|
| **Mode** | **High precision (vac chamber)** | **Hard vac** |
| **Exposure** | **20sec at 10mW/cm$^2$, I=320nm** | **5 sec at 25mW/cm$^2$** |
| **Develop** | **4:1(DI:AZ400k) for 25-34sec** | **4:1(DI:AZ400k) for 25-35sec** |

| |
|---|
| • $O_2$ RIE for descumming PMMA/PR interface layer. |
| Time: 6% PMMA **3.0 min** |
| Power: 33% |
| Gas: O2 40 sccm (40%) |
| Pressure: 70mT turn-on followed by 10mT run pressure. |
| • Deep UV flood PMMA **8 min** at 25 mW/cm$^2$ |
| • Develop PMMA in Chlorobenzene at 30°C for **30-40 sec** |
| • Toluene rinse. Dry quickly. If you leave the toluene on too long, the PR tends to bubble. |
| • Check if undercut is enough. If not place in chlorobenzene for 15-20 sec more and repeat process as necessary. |
| • O2 RIE for final descumming of PMMA residue **0.5 min** |
| • **CD 3$\mu$m** on ALL leads from TES; 6$\mu$m gap in antenna. |

*Metallization:* To be performed by H. LeDuc in his sputtering system

| |
|---|
| • Slight Ar sputter to clean surface. |
| • Sputter: Nb 2000Å (aproximately 6 min) using Nb sputterer at a base pressure of $\leq 5 \times 10^{-9}$ Torr |
| • Dip wafer in room temp ACETONE and heat to 50°C (water bath) for **30-60min**. |
| • Carefully use squirt bottle to remove residual metal, and swab while wet as necessary. |
| • Perform IPA dip/flow rinse to remove ACE and residual metals. |
| • Observe under microscope to ensure all lines have metal. |
| • **CD 3$\mu$m** on ALL leads from TES; 6$\mu$m gap in antenna. |
| • If NOT well patterned, strip metal and repeat evaporation. |

**4. Ti/SiO dielectric patterning**

Dielectric for middle of microstrip and act as a passivation layer to protect TES and resistors.

*Preparation:*

| |
|---|
| • Clean wafer by rinsing in ACE followed by IPA for 1 m each, blow dry. |
| • Dehydrate wafer by placing on 115°C hot plate for 2 m, Cool wafer on plate for ∼1 m. |
| • Place **HMDS** on front side of wafer let sit for 30 sec using small spinner |
| • Spread at 750 rpm for 3 sec and spin at 400 rpm for 40 seconds. |
| • Place **6% 495K PMMA** on front side of wafer using small spinner. |
| • Spread at 750 rpm for 3 sec and spin **6% 495K PMMA** at 4000 rpm for 40 seconds. |
| • Softbake at **95°C for 65 sec** followed by **105°C for 5 min.** |
| • Spread **AZ5214E** at 750 rpm for 3 sec and spin at 4000 rpm for 40 sec. |
| • let PR settle 5 min. |
| • Softbake at **95°C for 95 sec** |

*Patterning:* REGULAR 5124E DEVELOPMENT

| **Machine** | **MJB3** | **MA6** |
|---|---|---|
| **Mode** | **High precision (vac chamber)** | **Hard vac** |
| **Exposure** | **20sec at 10mW/cm$^2$, I=320nm** | **5 sec at 25mW/cm$^2$** |
| **Develop** | **4:1(DI:AZ400k) for 25-34sec** | **4:1(DI:AZ400k) for 25-35sec** |

| |
|---|
| • $O_2$ RIE for descumming PMMA/PR interface layer. |
| Time: 6% PMMA **3.0 min** |
| Power: 33% |
| Gas: O2 40 sccm (40%) |
| Pressure: 70mT turn-on followed by 10mT run pressure. |
| • Deep UV flood PMMA **8 min** at 25 mW/cm$^2$ |
| • Develop PMMA in Chlorobenzene at 30°C for **30-40 sec** |
| • Toluene rinse. Dry quickly. If you leave the toluene on too long, the PR tends to bubble. |
| • Check if undercut is enough. If not place in chlorobenzene for 15-20 sec more and repeat process as necessary. |
| • O2 RIE for final descumming of PMMA residue **0.5 min** |
| • **CD 10$\mu$m** on ALL lead legs. |

*Metallization:*

| |
|---|
| • Evaporate **50 Å of Ti at 1 Å /sec** in Sloan e-beam evaporator. |
| • Load into SiO thermal evaporation chamber and evaporate **2000Å of SiO at 5-10Å/s** |
| • Dip wafer in room temp ACETONE and heat to 50°C (water bath) for **30-60min**. |
| • Perform IPA dip/flow rinse to remove ACE and residual material. |
| • Observe under microscope to ensure all lines have metal. |
| • If NOT well patterned, strip metal and repeat evaporation. |
| • **CD 10$\mu$m** on ALL leads from TES. |

## 5. Nb Leads by liftoff

*Preparation:*

| |
|---|
| • Clean wafer by rinsing in ACE followed by IPA for 1 m each, blow dry. |
| • Dehydrate wafer by placing on 115°C hot plate for 2 m, Cool wafer on plate for ∼1 m. |
| • Place **HMDS** on front side of wafer let sit for 30 sec using small spinner |
| • Spread at 750 rpm for 3 sec and spin at 400 rpm for 40 seconds. |
| • Place **6% 495K PMMA** on front side of wafer using small spinner. |
| • Spread at 750 rpm for 3 sec and spin **6% 495K PMMA** at 4000 rpm for 40 seconds. |
| • Softbake at **95°C for 65 sec** followed by **105°C for 5 min.** |
| • Spread **AZ5214E** at 750 rpm for 3 sec and spin at 4000 rpm for 40 sec. |
| • let PR settle 5 min. |
| • Softbake at **95°C for 95 sec** |

*Patterning:* REGULAR 5124E DEVELOPMENT

| **Machine** | **MJB3** | **MA6** |
|---|---|---|
| **Mode** | **High precision (vac chamber)** | **Hard vac** |
| **Exposure** | **20sec at 10mW/cm$^2$, I=320nm** | **5 sec at 25mW/cm$^2$** |
| **Develop** | **4:1(DI:AZ400k) for 25-34sec** | **4:1(DI:AZ400k) for 25-35sec** |

| |
|---|
| • $O_2$ RIE for descumming PMMA/PR interface layer. |
| Time: 6% PMMA **3.0 min** |
| Power: 33% |
| Gas: O2 40 sccm (40%) |
| Pressure: 70mT turn-on followed by 10mT run pressure. |
| • Deep UV flood PMMA **8 min** at 25 mW/cm$^2$ |
| • Develop PMMA in Chlorobenzene at 30°C for **30-40 sec** |
| • Toluene rinse. Dry quickly. If you leave the toluene on too long, the PR tends to bubble. |
| • Check if undercut is enough. If not place in chlorobenzene for 15-20 sec more and repeat process as necessary. |
| • O2 RIE for final descumming of PMMA residue **0.5 min** |
| • **CD 3.4$\mu$m** on ALL leads from antenna; 5$\mu$m on ALL wire on lead leg. |

*Metallization:* To be performed by H. LeDuc in his sputtering system

| |
|---|
| • Slight Ar sputter to clean surface. |
| • Sputter: Nb 2000Å (aproximately 6 min) using Nb sputterer at a base pressure of $\leq 5 \times 10^{-9}$ Torr |
| • Dip wafer in room temp ACETONE and heat to 50°C (water bath) for **30-60min**. |
| • Carefully use squirt bottle to remove residual metal, and swab while wet as necessary. |
| • Perform IPA dip/flow rinse to remove ACE and residual metals. |
| • Observe under microscope to ensure all lines have metal. |
| • **CD 3.4$\mu$m** on ALL leads from antenna; 5$\mu$m on ALL wire on lead leg. |
| • If NOT well patterned, strip metal and repeat evaporation. |

"Normal" release process

**6. <u>Front-side SiN etch</u>**

Spread thick resist (AZ 4330) on backside to protect during etch.
Take care not to etch too much of $SiO_2$, as this layer provides etch-stop during deep Si etch.

*Preparation:*

| |
|---|
| • Clean wafer by rinsing in ACE followed by IPA for 1 m each, blow dry. |
| • Dehydrate wafer by placing on 115°C hot plate for 2 m, Cool wafer on plate for ∼1 m. |
| • Place **HMDS** on **back (unpatterned) side** of wafer let sit for 30 sec |
| • Spread **HMDS** on **back (unpatterned) side** at 750 rpm for 3 sec and spin at 400 rpm for 40 seconds. |
| • Spread **AZ4330** on **back (unpatterned) side** at 750 rpm for 3 sec and spin at 4000 rpm for 40 sec. |
| • let PR settle 5 min. |
| • Hardbake wafer at **115°C for 60 sec** |
| • Gently clean PR beads on **front (patterned) side** with a swab dipped in acetone. |
| • Hardbake wafer at **115°C for 60 sec** to dehydrate. |
| • Place **HMDS** on **front (patterned) side** of wafer let sit for 30 sec |
| • Spread **HMDS** on **front (patterned) side** at 750 rpm for 3 sec and spin at 400 rpm for 40 seconds. |
| • Spread **AZ4330** on **front (patterned) side** at 750 rpm for 3 sec and spin at 4000 rpm for 40 sec. |
| • let PR settle 5 min. |
| • Softbake at **95°C for 95 sec** |

*Patterning:*

| **Machine** | **MJB3** | **MA6** |
|---|---|---|
| **Mode** | **High precision (vac chamber)** | **Hard vac** |
| **Exposure** | **20sec at 10mW/cm$^2$, I=320nm** | **5 sec at 25mW/cm$^2$** |
| **Develop** | **4:1(DI:AZ400k) for 25-35sec** | **4:1(DI:AZ400k) for 120-10sec** |

| |
|---|
| • Inspect pattern under microscope. Proceed if all lines are well defined. Otherwise, repeat this step. |
| • **CD 7$\mu$m** on ALL side SiN legs; 16$\mu$m on lead SiN leg. |
| • Hardbake wafer at **115°C for 2 min.** |

*Etching:*

| |
|---|
| • Hardbake wafer at **115°C for 5 min.** |
| • Dry etch using CF4 @ 22 sccm, 100mT, 100W for 44 min, base pressure $\leq 2 \times 10^{-5}$ Torr<br>• ***etch rate is approximately 25 nm/min for Si3N4.***<br>• Can use UV edge finder. |
| • **CD 7$\mu$m** on ALL side SiN legs; 16$\mu$m on lead SiN leg. |

**7. <u>Back-side SiN etch</u>**

Pattern backside window, etch SiN. $SiO_2$ layer needs to be completely removed in prep. for deep Si etch.

*Preparation:*

| |
|---|
| • Clean wafer by rinsing in ACE followed by IPA for 1 m each, blow dry. |
| • Dehydrate wafer by placing on 115°C hot plate for 2 m, Cool wafer on plate for ∼1 m. |
| • Place **HMDS** on **front (patterned) side** of wafer let sit for 30 sec |
| • Spread **HMDS** on **front (patterned) side** at 750 rpm for 3 sec and spin at 400 rpm for 40 seconds. |
| • Spread **AZ4330** on **front (patterned) side** at 750 rpm for 3 sec and spin at 4000 rpm for 40 sec. |
| • let PR settle 5 min. |
| • Hardbake wafer at **115°C for 60 sec** |
| • Gently clean PR beads on **back (unpatterned) side** with a swab dipped in acetone. |
| • Hardbake wafer at **115°C for 60 sec** to dehydrate. |
| • Place **HMDS** on **back (unpatterned) side** of wafer let sit for 30 sec |
| • Spread **HMDS** on **back (unpatterned) side** at 750 rpm for 3 sec and spin at 400 rpm for 40 seconds. |
| • Spread **AZ5740** on **back (unpatterned) side** at 750 rpm for 3 sec and spin at 2000 rpm for 30 sec. |
| • let PR settle 5 min. |
| • Softbake at **110°C for 6 min** |

*Patterning:*

| **Machine** | **MJB3 transmission IR** | **MA6 backside feature** |
|---|---|---|
| **Mode** | | **soft or hard** |
| **Exposure** | | **65 sec at 25mW/cm$^2$** |
| **Develop** | | **3:1(DI:AZ400k) for 5-6 min** |

| |
|---|
| • Hardbake wafer at **130°C for 5 min** |
| • Inspect pattern under microscope. Proceed if all lines are well defined. Otherwise, repeat this step. |

*Etching:*

| |
|---|
| • Dry etch using RIE $CF_4$ @ 40 sccm and $O_2$ @ 8 sccm, 50mT, 100W for 14-15 min, base pressure $\leq 2 \times 10^{-5}$ Torr<br>• ***etch rate is approximately 170 nm/min for $Si_3N_4$, slower for $SiO_2$.***<br>• Can use UV edge finder. |
| • If $SiO_2$ isn't completely removed (surface should appear silvery) do BOE dip for requisite time. Consult color chart for approximate thickness. |

**8. Deep silicon etch with STS**

STS deep etch team will perform etch. Prep for process:

| |
|---|
| • Make sure no PR splatter remains in holes on backside. |
| • Place 6" backing wafer onto hot plate @ 80-90$^circ$C for yellow wax application. |
| • Melt small piece of yellow wax onto backing wafer until it liquifies. Cover inside area where wafer is to be placed. Removed and allow wax to cool. Reheat, liquifying wax, place one edge of detector wafer on liquified wax (backside up), then slowly lower wafer to reduce bubbles. Place weight on wafer, remove from heat and allow to cool. |
| • Cover exposed backing wafer with Kapton tape. |
| • Use program Spider-2 for STS etch, ~2 nm/min. 200 $\mu$m takes about 1 hr 33 min, will stop on $SiO_2$ layer. |
| • Dip whole wafer sandwich into BOE to completely remove $SiO_2$ from behind web. Watch out for bubbles! |

## 9. Final Release

| |
|---|
| • Remove Kapton tape from backing wafer. Scrape off excess yellow wax with blade. |
| • Place wafer sandwich on holder, device side down. |
| • Fill with warm TCE. As yellow wax dissolves, devices will fall to bottom of holder. |
| • Rinse devices carefully in Acetone and IPA, taking care not to snap delicate structures. |

# Bibliography


[1] http://lambda.gsfc.nasa.gov/product/cobe.

[2] http://map.gsfc.nasa.gov/.

[3] http://astro.estec.esa.nl/SA-general/Projects/Planck/.

[4] http://universe.gsfc.nasa.gov/.

[5] http://groups.physics.umn.edu/cosmology/maxipol/.

[6] R. A. Alpher and R. C. Herman. Theory of the origin and relative abundance distribution of the elements. *Rev. Mod. Phys.*, 22(2):152–212, 1950.

[7] A. Benoit et al. First detection of polarization of the submillimetre diffuse galactic dust emission by Archeops. *Applied Optics*, submitted 2003. see also astro-ph/0306222.

[8] J. J. Bock, H. M. DelCastillo, et al. Infrared bolometers with silicon micromesh absorbers. In *Submillimeter and Far-Infrared Space Instrumentation*, pages 119–122. ESTEC, 1996.

[9] J. R. Bond, G. Efstathiou, and M. Tegmark. Forecasting cosmic parameter errors from microwave background anisotropy experiments. *Mon. Not. R. Astron. Soc.*, 291:33–41, 1997.

[10] B. Cabrera, J. M. Martinis, et al. TES spectrophotometers for near IR/Optical/UV. In *American Institute of Physics Conference Series*, pages 565–570, 2002.

[11] G. Chattopadhyay and J. Zmuidzinas. A dual-polarized slot antenna for millimeter waves. *IEEE Trans. Antenn. Propag.*, 46(5):736–737, 1998.

[12] E. S. Cheng, P. R. Saulson, et al. Large-scale anisotropy in the 2.7 K radiation. *Ap. J.*, 232:L139–L143, 1979.

[13] P. de Bernardis et al. A flat universe from high-resolution maps of the cosmic microwave background radiation. *Nature*, 404:955–959, 2000.

[14] P. A. J. de Korte, W. M. Bergmann Tiest, et al. Noise and energy resolution of X-ray microcalorimeters. *IEEE T. Appl. Supercon.*, 11(1):747–750, 2001.

[15] R. H. Dicke, P. Peebles, P. G. Roll, and D. Wilkinson. Cosmic black-body radiation. *Ap. J.*, 142:414–419, 1965.

[16] C. D. Dowell, C. A. Allen, et al. SHARC II: a Caltech Submillimeter Observatory facility camera with 384 pixels. In *Millimeter and Submillimeter Detectors for Astronomy*, page 4855. SPIE, 2003.

[17] P. M. Downey, A. D. Jeffries, et al. Monolithic silicon bolometers. *Applied Optics*, 23(6):910–914, 1984.

[18] R. Durrer, B. Novosyadlyj, et al. Acoustic peaks and dips in the cosmic microwave background power spectrum. *Ap. J.*, 583:33–48, 2003.

[19] D. Fixsen, E. Cheng, et al. The cosmic microwave background spectrum from the full COBE FIRAS data set. *Ap. J.*, 473:576–587, 1996.

[20] A. Friedmann. *Z. Phys.*, 10:377, 1922.

[21] A. Friedmann. *Z. Phys.*, 21:326, 1924.

[22] G. Gamow. The origin of elements and the separation of galaxies. *Phys. Rev.*, 74:505–506, 1948.

[23] J. M. Gildemeister, A. T. Lee, and P. L. Richards. Model for excess noise in voltage-biased superconducting bolometers. *Applied Optics*, 40(34):6229–6235, 2001.

[24] A. Goldin, J. J. Bock, C. L. Hunt, et al. Design of broadband filters and antennas for SAMBA. In *Millimeter and Submillimeter Detectors for Astronomy*, pages 163–171. SPIE, 2003.

[25] A. H. Guth. Inflationary Universe: A possible solution to the horizon and flatness problems. *Phys. Rev. D*, 23:347–356, 1981.

[26] E. E. Haller. Isotopically engineered semiconductors. *Journal of Applied Physics*, 77:2857–2878, 1995.

[27] N. Halverson et al. Degree Angular Scale Interferometer first results: A measurement of the cosmic microwave background power spectrum. *Ap. J.*, 568:38–45, 2002.

[28] W. Herschel. *Philos. Trans. R. Soc.*, 90:284, 1800.

[29] G. C. Hilton, J. M. Martinis, et al. Microfabricated transition-edge x-ray detectors. *IEEE T. Appl. Supercon.*, 11(1):739–742, 2001.

[30] H. F. C. Hoevers, A. C. Bento, et al. Thermal fluctuation noise in a voltage biased superconducting transition edge bolometer. *Appl. Phys. Lett.*, 77(26):4422–4424, 2000.

[31] P. Horowitz and W. Hill. *The Art of Electronics*, pages 175–176, 232–235. Cambridge University Press, Cambridge, United Kingdom, 1996.

[32] W. Hu and S. Dodelson. Cosmic microwave background anisotropies. *Annu. Rev. Astron. Astr.*, 40:171–216, 2002.

[33] W. Hu, N. Sugiyama, and J. Silk. The physics of microwave background anisotropies. *Nature*, 386:37–43, 1997.

[34] W. Hu and M. White. A CMB polarization primer. *New Atronomer*, 2:323, 1997. see also astro-ph/9706147.

[35] E. Hubble and M. L. Humason. The velocity-distance relation among extra-galactic nebulae. *Ap. J.*, 74:43–80, 1931.

[36] Infrared Laboratories. `http://www.irlabs.com/`. Tucson, AZ.

[37] K. D. Irwin. An application of electrothermal feedback for high resolution cryogenic particle detection. *Appl. Phys. Lett.*, 66(15):1998–2000, 1995.

[38] K. M. Itoh, E. E. Haller, W. L. Hansen, J. W. Beeman, J. W. Farmer, A. Rudnev, A. Tikhomirov, and V. I. Ozhogin. Neutron transmutation doping of isotopically engineered Ge. *Appl. Phys. Lett.*, 64:2121–2123, Apr. 1994.

[39] W. C. Jones. personal communication.

[40] G. Jungman, M. Kamionkowski, et al. Cosmological-parameter determination with microwave background maps. *Phys. Rev. D*, 54:1332–1344, 1996.

[41] Y. Kim and M. J. Stephen. Flux flow and irreversible effects. In R. D. Parks, editor, *Superconductivity*, volume 2, pages 1107–1165. Marcel Decker, Inc., New York, 1969.

[42] C. Kittel. *Introduction to Solid State Physics*, pages 137–138. John Wiley & Sons, 7th edition, 1996.

[43] A. Kogut, C. Lineweaver, et al. Dipole anisotropy in the COBE differential microwave radiometers first-year sky maps. *Ap. J.*, 419:1–6, 1993.

[44] J. M. Kovac et al. Detection of polarization in the cosmic microwave background using DASI. *Nature*, 420(6917):772–787, 2002.

[45] Lake Shore Cryotronics, Inc. `http://www.lakeshore.com/`. Westerville, OH.

[46] A. E. Lange, E. Kreysa, et al. Improved fabrication techniques for infrared bolometers. *Int. J. Infrared Milli.*, 4(5):689–706, 1983.

[47] S. P. Langley. The Bolometer. *Nature*, 25:14–16, 1881.

[48] S.-F. Lee, J. M. Gildemeister, et al. Voltage-biased superconducting transition-edge bolometer with strong electrothermal feedback operated at 370 mK. *Appl. Opt.*, 37(16):3391–3397, 1998.

[49] E. M. Leitch et al. Measurement of polarization with the Degree Angular Scale Interferometer. *Nature*, 420(6917):763–771, 2002.

[50] G. Lemaitre. A homogeneous universe of constant mass and increasing radius accounting for the radial velocity of extra-galactic nebulae. *Mon. Not. R. Astr. Soc.*, 91:483–490, 1931.

[51] M. A. Lindeman, S. R. Bandler, et al. Probing the phase transition of Mo/Au TES Microcalorimeters. In *X-Ray and Gamma-Ray Telescopes and Instruments for Astronomy*, volume 4851, pages 957–964. Proceedings of the SPIE, 2003.

[52] M. A. Lindeman, R. P. Brekosky, et al. Performance of Mo/Au TES Microcalorimeters. In *Low Temperature Detectors*, volume 605, pages 203–206. LTD-9, American Institute of Physics, 2002.

[53] Linear Research Inc. `http://www.linearresearch.com/`. San Diego, CA.

[54] A. Luukanen, K. M. Kinnunen, et al. Fluctuation-limited noise in a superconducting transition-edge sensor. *Phys. Rev. Lett.*, 90(23):238306, 2003.

[55] J. M. Martinis, G. C. Hilton, et al. Calculation of $T_c$ in a normal-superconductor bilayer using the microscopic-based Usadel theory. 444:23–27, 2000.

[56] S. Masi et al. The BOOMERANG experiment and the curvature of the Universe. *Prog. Part. Nucl. Phys.*, 48:243–261, 2002.

[57] J. C. Mather. Bolometer noise: nonequilibrium theory. *Appl. Opt.*, 21(6):1125–1129, 1982.

[58] J. C. Mather. Bolometers: ultimate sensitivity, optimization, and amplifier coupling. *Appl. Opt.*, 23(4):584–588, 1984.

[59] P. D. Mauskopf, J. J. Bock, H. del Castillo, W. L. Holzapfel, and A. E. Lange. Composite infrared bolometers with $Si_3N_4$ micromesh absorbers. *Appl. Opt.*, 36:765–771, 1997.

[60] D. McCammon, R. Almy, et al. High-resolution calorimetry: limitations of doped semiconductor thermometers. *Nucl. Instr. Meth Phys. A*, 436(1-2):205–211, 1999.

[61] R. B. Partridge and D. T. Wilkinson. Isotropy and homogeneity of the universe from measurements of the cosmic microwave background. *Phys. Rev. Lett.*, 18(14):557–559, 1967.

[62] P. J. Peebles and D. T. Wilkinson. Comment on the anisotropy of the primeval fireball. *Phys. Rev.*, 174(5):2168, 1968.

[63] P. J. E. Peebles. *Principles of Physical Cosmology.* Princeton University Press, Princeton, New Jersey, 1993.

[64] A. A. Penzias and R. W. Wilson. A measurement of excess antenna temperature at 4080 mc/s. *Ap. J.*, 142:419–421, 1965.

[65] B. J. Peterson. Infrared imaging video bolometer. *Rev. Sci. Instr.*, 71(10):3696–3701, 2000.

[66] Quantum Design. `http://www.qdusa.com/`. San Diego, CA.

[67] M. J. Rees and D. W. Sciama. Large-scale density inhomogeneities in the Universe. *Nature*, 217:511–516, 1967.

[68] P. L. Richards. Bolometers for infrared and millimeter waves. *J. Appl. Phys.*, 76(1):1–24, 1994.

[69] G. Rickayzen. The Theory of Bardeen, Cooper and Schrieffer. In R. D. Parks, editor, *Superconductivity*, volume 1, pages 77–85. Marcel Decker, Inc., New York, 1969.

[70] W. Rindler. Cosmological-parameter determination with microwave background maps. *Mon. Not. R. Astron. Soc.*, 116:662–677, 1956.

[71] J. E. Ruhl, P. A. R. Ade, et al. Improved measurement of the angular power spectrum of temperature anisotropy in the CMB from two new analyses of BOOMERANG observations. *Submitted to Ap. J.*, 2002. see also astro-ph/0212229.

[72] R. K. Sachs and A. M. Wolfe. Perturbations of a cosmological model and angular variations of the microwave background. *Ap. J.*, 147(1):73–90, 1967.

[73] J. Silk. *The Big Bang.* W. H. Freeman and Company, New York, 1989.

[74] G. F. Smoot, M. V. Gorenstein, and R. A. Muller. Detection of anisotropy in the cosmic blackbody radiation. *Phys. Rev. Lett.*, 39(14):898–901, 1977.

[75] Stanford Research Systems. `http://www.srsys.com/`. Sunnyvale, CA.

[76] I. A. Strukov and A. A. Brukhanov. The Relikt-1 experiment – New results. *Mon. Not. R. Astr. Soc.*, 258:37p–40p, 1992.

[77] K. S. Thorne. Primordial element formation, primordial magnetic fields, and the isotropy of the universe. *Ap. J.*, 148:51–68, 1967.

[78] D. J. van Ooijen and G. J. van Gurp. *Phys. Lett.*, 17:230, 1965.

[79] A. Vayonakis, C. Luo, et al. The millimeter-wave properties of superconducting microstrip lines. In *American Institute of Physics Conference Series*, pages 539–542, 2002.

[80] G. M. Voellmer, C. A. Allen, et al. Design and fabrication of two-dimensional semiconducting bolometer arrays for HAWC and SHARC-II. In *Millimeter and Submillimeter Detectors for Astronomy*, volume 4855, pages 63–72. SPIE, 2003.

[81] F. C. Wellstood, C. Urbina, and J. Clarke. Hot-electron effects in metals. *Phys. Rev. B*, 49(9):5942–5955, 1994.

[82] R. W. Wilson. *Nobel Prize Lecture*. 1978.

[83] A. L. Woodcraft, R. V. Sudiwala, et al. High precision characterisation of semiconductor bolometers. *Int. J. Infrared Milli.*, 23(4):575–595, 2002.

[84] J. Zmuidzinas and H. R. LeDuc. Quasi-optical slot antenna sis mixers. *IEEE Transactions on Microwave Theory and Techniques*, 40(9):1797–1804, 1992.